2010 (Heisei 22)

Doctoral Thesis

MODELING AND PARAMETER ESTIMATION OF RHEOLOGICAL OBJECTS FOR SIMULTANEOUS REPRODUCTION OF FORCE AND DEFORMATION

Ritsumeikan University Graduate School of
Science and Engineering
Doctoral Program in Science and Engineering
Department of Robotics

Zhongkui Wang

Acknowledgements

With a deep gratitude, I would like to thank my advisor, Professor Shinichi Hirai, who has contributed a great deal to my doctoral work. He has been a mentor and friend throughout my time at Ritsumeikan University. I greatly appreciate the guidance and support that he has provided. In addition, I would like to thank Professor Sadao Kawamura and Professor Noritaka Yamamoto for their kind reviews of my dissertation and valuable advices. I am grateful to Professor Shigehiro Morikawa, who has given me a lot of help and advices about my experiments. I would also like to thank Professor Ota, who has provided Japanese sweets materials for my experiments and demonstrated the making procedures of traditional Japanese sweets products. Many thanks to Ms. Mari Hatanaka for her always kind help and patient with my poor Japanese.

I am deeply grateful to my family, who have extended their love and encouragement over a great distance. Without their understanding and support through these years, I am unable to make my dreams coming true. I would like to thank my wonderful group of Chinese friends, who have brought a lot of fun to me and made my life more colorful.

Many thanks to several graduated students, especially Dr. Sumadi Jien, Yujiro Yamazaki, Kazuki Namima, and Kazumi Endo, who have always been there for me whenever I need help. Thanks to my body building buddies, Yuki Kataoka and Masayuki Tatsumi. We have had a lot of fun together to make our bodies stronger. I also would like to thank Van Anh Ho for lending me the stage controller many times and kind help for debugging the programs. Grateful to Yoshiyuki Abe for his time to translate my abstract to Japanese.

Sincere thanks to my research group members, Lijuan Wang, Yoshiyuki Abe, Atsuo Mori, Yusuke Taniguchi, and Masatoshi Kinoshita, for their inspiration, support, and kind help.

I am eternally grateful to you all.

Modeling and Parameter Estimation of Rheological Objects for Simultaneous Reproduction of Force and Deformation

Zhongkui Wang
Advisor: Prof. Shinichi Hirai

Abstract

There are many deformable objects in our living life demonstrated rheological behaviors, such as human organs and tissues, potteries, clays, and various food products. Many applications has been involved, including computer aided surgery, robotics, and food automation. Rheological object has both elastic and plastic properties. Due to the presence of residual deformation, it is difficult to model rheological objects, especially to reproduce both rheological force and residual deformation simultaneously.

This thesis aims at modeling and parameter estimation of rheological objects for simultaneous reproductions of both rheological force and deformation. Physically-based models were firstly investigated for describing rheological behaviors and were summarized into two groups: serial and parallel models. Generalized constitutive laws of both groups were formulated. Analytical expressions of rheological forces and residual deformation were derived for parallel models. We found a contradiction between the reproductions of rheological force and deformation. To solve this problem, a dual-moduli viscous element was introduced.

2D and 3D FE dynamic models were developed and then extended to deal with non-uniform layered objects and contact interaction between objects as well. Criterions for detecting the contact moment were established. In addition, to cover large deformation and deformation with rotation motion, FE model with

nonlinear Green strain tensor was developed and simulation results were presented as well.

Methods for estimating the parameters involved in the FE model were proposed based on nonlinear optimization, which aims at minimizing the difference between simulation (or calculation) results and experimental measurements. Basically, two ideas were investigated. One is based on iterative FE simulation and the other is based on the straightforward calculation of rheological forces by taking the advantages of parallel structure of the physical model. We have tested both methods for estimating the parameters of our FE model.

Various compression experiments with commercial available clay and Japanese sweets materials were performed. During the experiments, force data and images of deformed shapes were recorded and used to estimate the physical parameters of both materials. The estimated parameters and the proposed FE models were then used to reproduce these experimental behaviors. Finally, by using our FE model and parameter estimation method, we successfully reproduced both rheological forces and deformation behaviors simultaneously.

Contents

List of Figures

List of Tables

Nomenclature

Roman Symbols

$\mathbf{A}$ the bottom constraint matrix in 2D FE formulation

$\mathbf{A}_{3D}$ the bottom constraint matrix in 3D FE formulation

$\mathbf{B}$ the top constraint matrix in 2D FE formulation

$\mathbf{B}_{3D}$ the top constraint matrix in 3D FE formulation

$\mathbf{C}$ constraint matrix denoted the contact nodes on the object

$\mathbf{D}$ elasticity matrix of an elastic isotropic material

$\mathbf{d}(t)$ displacement function used in 2D FE formulation

$\mathbf{d}^{3D}(t)$ displacement function used in 3D FE formulation

$\mathbf{d}_i^{exp}$ displacement vector of the i-th nodal point during experiment

$\mathbf{d}_i^{sim}$ displacement vector of the i-th nodal point during simulation

$\mathbf{E}(\bullet)$ objective function for optimization problems

$\mathbf{F}^{bott}$ force vector generated on the boundary nodes of the bottom layer object in the formulation of non-uniform layered object

$\mathbf{F}^{top}$ force vector generated on the boundary nodes of the top layer object in the formulation of non-uniform layered object

$\mathbf{F}_1$ force vector generated at the first Maxwell element in the parallel 5-element model of 2D FE formulation

$\mathbf{F}_1^{3D}$ force vector generated at the first Maxwell element in the parallel 5-element model of 3D FE formulation

$\mathbf{F}_2$ force vector generated at the second Maxwell element in the parallel 5-element model of 2D FE formulation

$\mathbf{F}_2^{3D}$ force vector generated at the second Maxwell element in the parallel 5-element model of 3D FE formulation

$\mathbf{F}_3$ force vector generated at the third viscous element in the parallel 5-element model of 2D FE formulation

$\mathbf{F}_3^{3D}$ force vector generated at the third viscous element in the parallel 5-element model of 3D FE formulation

$\mathbf{f}_i^{exp}$ force vector at the i-th sampling time during experiment

$\mathbf{f}_i^{sim}$ force vector at the i-th sampling time during simulation

$\mathbf{F}_{2D}^{ela}$ elastic force vector in 2D FE formulation

$\mathbf{F}_{2D}^{rheo}$ rheological force vector in 2D FE formulation

$\mathbf{F}_{3D}^{ela}$ elastic force vector in 3D FE formulation

$\mathbf{F}_{3D}^{rheo}$ rheological force vector in 3D FE formulation

$\mathbf{J}_\lambda$ normal connection matrices in 2D FE formulation

$\mathbf{J}_\lambda^{3D}$ normal connection matrices in 3D FE formulation

$\mathbf{J}_\mu$ shear connection matrices in 2D FE formulation

$\mathbf{J}_\mu^{3D}$ shear connection matrices in 3D FE formulation

$\mathbf{K}$ stiffness matrix in 2D FE formulations

$\mathbf{K}^{3D}$ stiffness matrix in 3D FE formulations

$\mathbf{M}$ inertia matrix in 2D FE formulation

$\mathbf{M}^{3D}$ inertia matrix in 3D FE formulation

$\mathbf{q}$ displacement vector used in the formulation of the Green strain tensor

$\mathbf{u}^{bott}$ displacement vector of the boundary nodes on the bottom layer in the formulation of non-uniform layered object

$\mathbf{u}^{top}$ displacement vector of the boundary nodes on the top layer in the formulation of non-uniform layered object

$\mathbf{u}_c^{ins}$ displacement vector of contact nodes on the instrument

$\mathbf{u}_c^{obj}$ displacement vector of contact nodes on the object

$\mathbf{u}_N$ displacement vector of all nodal points in 2D FE mesh

$\mathbf{u}_N(\infty)$ residual displacements of all nodal points

$\mathbf{u}_N^{3D}$ displacement vector of all nodal points in 3D FE mesh

$\mathbf{v}_c^{ins}$ velocity vector of contact nodes on the instrument

$\mathbf{v}_c^{obj}$ velocity vector of contact nodes on the object

$\mathbf{v}_N^{Push}$ constant velocity vector during pushing phase

A_i coefficients of the constitutive laws in both serial and parallel models

B_j^{p1} coefficients of the constitutive laws in parallel models of type 1

B_j^{p2} coefficients of the constitutive laws in parallel models of type 2

B_j^{s1} coefficients of the constitutive laws in serial models of type 1

B_j^{s2} coefficients of the constitutive laws in serial models of type 2

c viscous modulus of the viscous element, Pa·s

c_i viscous modulus of the i-th viscous element, Pa·s

c_i^{load} viscous moduli used during operations

c_i^{unload} viscous moduli used after operations

E Young's modulus of the elastic element, Pa

$E(c_i^{unload})$ objective function used in final-shape optimization

E_i Young's modulus of the i-th elastic element, Pa

h thickness of the object in 2D modeling

$N_{i,j,k}$ interpolating shape function with the node order of i, j, and k

N_{ix} partial derivative of $N_{i,j,k}$ relative to x

N_{iy} partial derivative of $N_{i,j,k}$ relative to y

$N_{j,k,i}$ interpolating shape function with the node order of j, k, and i

N_{jx} partial derivative of $N_{j,k,i}$ relative to x

N_{jy} partial derivative of $N_{j,k,i}$ relative to y

$N_{k,i,j}$ interpolating shape function with the node order of k, i, and j

N_{kx} partial derivative of $N_{k,i,j}$ relative to x

N_{ky} partial derivative of $N_{k,i,j}$ relative to y

p constant velocity during pushing phase

s factor of Laplace transform

t time

t_h holding time in experiment and simulation

t_p pushing time in experiment and simulation

U strain energy

w scale factor used in optimization of deformed shapes

Greek Symbols

α scalar parameter used in dual-moduli viscous element, Pa·s

ℓ_1 Lagrange multiplier in 2D FE formulation corresponding to the constraint on the bottom surface

ℓ_1^{3D} Lagrange multiplier in 3D FE formulation corresponding to the constraint on the bottom surface

ℓ_2 Lagrange multiplier in 2D FE formulation corresponding to the constraint on the top surface

ℓ_2^{3D} Lagrange multiplier in 3D FE formulation corresponding to the constraint on the top surface

γ Poisson's ratio

κ switch function used in dual-moduli viscous element

λ the first Lamé's constant in formulation of 2D generalized Hooke's law

λ_1^{ela} the first Lamé constant of the first elastic element in the 5-element model

λ_2^{ela} the first Lamé constant of the second elastic element in the 5-element model

λ_3^{vis} the first Pseudo Lamé constant of the third viscous element in the 5-element model

$\boldsymbol{\alpha}$ predetermined vector associated with the normal strain component along x-axes in the Green strain tensor

$\boldsymbol{\beta}$ predetermined vector associated with the normal strain component along y-axes in the Green strain tensor

$\boldsymbol{\epsilon}$ Cauchy strain tensor

$\boldsymbol{\epsilon}(\infty)$ strain vector at time infinite

$\boldsymbol{\epsilon}^g$ Green strain tensor

ϵ_i	Cauchy strain tensor at the i-th element
ϵ_i^{ela}	strain vector at the i-th elastic element
ϵ_i^{vis}	strain vector at the i-th viscous element
ϵ_{xx}^g	the normal strain component along x-axes in the Green strain tensor
ϵ_{xy}^g	the shear strain component in the Green strain tensor
ϵ_{yy}^g	the normal strain component along y-axes in the Green strain tensor
σ	stress tensor
σ_i	stress tensor at the i-th element
$\mathbf{\Theta}$	a vector consisting of physical parameters to be estimated
ζ	predetermined vector associated with the shear strain component in the Green strain tensor
μ	the second Lamé's constant in formulation of 2D generalized Hooke's law
μ_1^{ela}	the second Lamé constant of the first elastic element in the 5-element model
μ_2^{ela}	the second Lamé constant of the second elastic element in the 5-element model
μ_3^{vis}	the second Pseudo Lamé constant of the third viscous element in the 5-element model
ω	angular frequency used in CSM

Acronyms

1D	one-dimensional
2D	two-dimensional
3D	three-dimensional

Nomenclature

CSM constraint stabilization method

FEM finite element method

GA genetic algorithm

GPU graphics processing unit

MRI magnetic resonance imaging

MSD mass-spring-damper

SPH smoothed particle hydrodynamics

SQP sequential quadratic programming

Chapter 1

Introduction

1.1 Modeling of Deformable Objects

There are many deformable objects in our daily life, such as human organs and tissues, pottery, clay, and various food products. Modeling and simulation of such deformable objects has been studied for over 20 years and many applications have been involved, including computer aided surgery, food automation, and robot manipulation. In our definition, deformable objects were roughly divided into three categories (Fig. 1.1): elastic object, in which the deformation is completely reversible; plastic object, in which the deformation is completely maintained; and rheological object, in which the deformation is partially reversible.

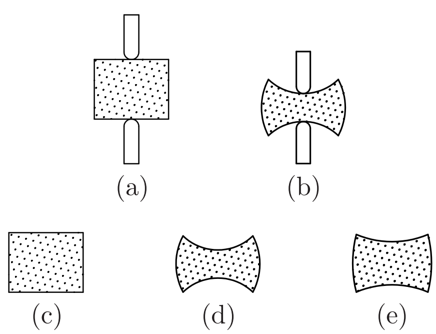

Figure 1.1: Categories of deformable objects. (a) Original shape before pushing. (b) Deformed shape during manipulation. (c), (d), and (e) Deformed shape after releasing. (c) Elastic object. (d) Plastic object. (e) Rheological object.

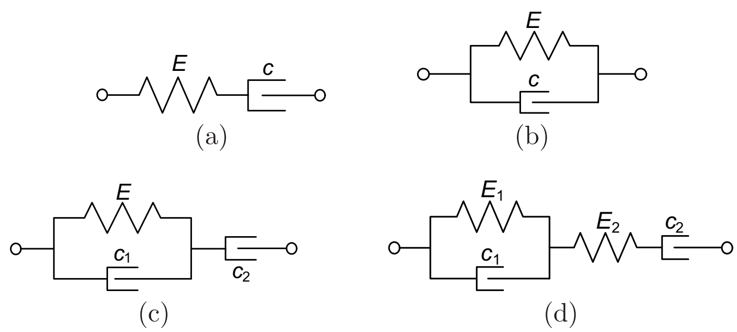

Figure 1.2: Widely used physically-based models: (a) the Maxwell model, (b) the Kelvin-Voigt model, (c) the Lethersich model, and (d) the Burgers model.

Early work on the modeling of deformable objects can date back to Terzopoulos *et al.* (1987) and Terzopoulos & Fleischer (1988). They have shown the advantages of physically-based models over kinematic models for computer animation and have proposed several physically-based models for simulating inelastic deformation. Generally, a physically-based model consists of a finite numbers of elastic and viscous elements connected in a certain configuration. Some famous physically-based models, such as the Maxwell model[1], the Kelvin-Voigt model[2], the Lethersich model[3], and the Burgers model[4] (Fig. 1.2), were often used to describe the behaviors of deformable materials. In conventional material tests, *e.g.*, force relaxation and creep recovery tests, one-dimensional (1D) models were used to describe the behaviors of materials. However, along with the developments of computer, we are able to reconstruct an object with two-dimensional (2D) and three-dimensional (3D) geometry to achieve more realistic simulation behaviors of deformable objects.

The most popular methods for 2D and 3D modeling of deformable objects are the mass-spring-damper (MSD) method [Waters (1987)] and the finite element method (FEM) [Cotin *et al.* (1996)]. The MSD method has been used to simulate cloth animation [Baraff & Witkin (1998)], facial expressions [Kähler *et al.* (2001)], and the deformation of a myoma (pathology) [Lioyd *et al.* (2007)], respectively.

[1]It was introduced by J. C. Maxwell in 1867.
[2]It was firstly introduced by L. Kelvin in 1875 and later by W. Voigt in 1889.
[3]It was firstly introduced by W. Lethersich in 1942.
[4]It was firstly introduced by J. M. Burgers in 1935.

The MSD method has the advantage of conceptual simplicity and relatively low computation costs. However, the formulation of MSD method was not based on continuum mechanics and the simulation accuracy is quite limited. Therefore, a finite element (FE) model has been used as a reference to calibrate MSD model based on genetic algorithm optimization [Bianchi *et al.* (2004)] and analytical expression [Lioyd *et al.* (2007)], respectively.

The FE method has proven to be a powerful tool for simulating complex behaviors of deformable objects. In FE formulation, an object is described by a set of elements (*e.g.*, triangles in 2D case and tetrahedrons in 3D case). The dynamic behaviors of the object are then determined by analyzing the behaviors of individual elements. In recent years, many commercial FE softwares are available and more and more researchers have been using FE method in their applications. The FE method has been widely used in computer-aided surgery to simulate the deformation behaviors of biological organs and tissues, such as porcine liver [Ahn & Kim (2010)], human skin [Bischoff *et al.* (2000)], liver [Nava *et al.* (2008)], and uterus [Kauer *et al.* (2002)]. It currently also was employed to model some surgical operations, such as needle insertion [Hing *et al.* (2007)] and soft tissue cutting [Mendoza & Laugier (2003)]. FE method is based on continuum mechanics and does not suffer from geometry problems. But, it is quite time-consuming. In order to speed up FE simulation, matrix condensation technology [Bro-Nielsen & Cotin (1996)] and fast FEM [Bro-Nielsen (1998)] have been proposed. Current parallel calculation architecture, such as graphics processing unit (GPU), also has been investigated by Taylor *et al.* (2009). In addition, to achieve real-time simulation of soft tissue, other modeling methods were also presented, such as the radial elements method [Balaniuk & Salisbury (2003)] and the point collocation-based method of finite spheres [Lim & De (2007)]. The FEM also has been used in food industry to model food products. For example, FE analysis has been used to model and simulate the indentation of bread crumbs [Liu & Scanlon (2003)]; FE simulation has been used to evaluate the dependence of temperature and water content on process time during meat cooking [Purlis & Salvadori (2005)]; and FE method also has been employed to calculate food quality and safety losses during processing, storage and distribution [Martins (2006)].

To date, the modeling of soft organs and tissues mostly supposed that the organs and tissues are completely recoverable and the deformation behaviors after unloading operations are not considered in most applications. Some organs and tissues, however, may fail to totally recover from the deformation after loading-unloading operations. Hrapko *et al.* (2006) found that porcine brain tissue did not recover completely after a loading-unloading cycle. In vivo experimental results showed that residual deformation may also present in human liver [Nava *et al.* (2008)]. In addition, residual deformation may also exist when biological organs and tissues suffer from some diseases or undergoing a significant external forces. Such residual deformations could be handled by rheological models. On the other hand, modeling and property estimation of food materials were studied so far mainly on the chemical and ingredient composition point of view for improving the cooking ability, product quality, and nutrition. As an "engineering material", however, it was not well developed. Chua *et al.* (2003) stated that the most critical barrier against the application of robotics and automation in food industry is a lack of understanding of the food product properties as an "engineering" material for handling operations. We have therefore turn our attention on the modeling, simulation, and parameter estimation of rheological objects, especially considering the residual deformations which has not been studied intensively.

1.2 Parameter Estimation of Deformable Objects

Before simulating any real objects, some physical parameters of the model have to be available in advance. In conventional material science, material properties were usually estimated by direct calculation or curve fitting based on the measurements of experimental tests, such as compressive, tensile, force relaxation, and creep recovery tests [Shames & Cozzareli (1992)]. However, these calculations and tests were mostly under an assumption of 1D deformation (pure uniaxial or pure shear deformation). Deformable objects, on the other hand, have more complex deformation behaviors and sometimes include several different material properties. Therefore, they have to be simulated as a 2D/3D continuum and

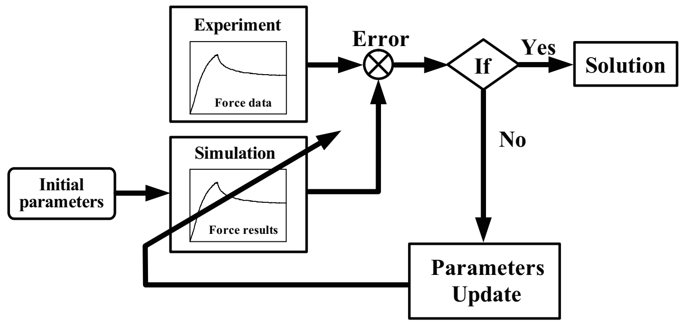

Figure 1.3: Optimization process for parameter estimation.

complex deformation behaviors have to be considered during parameter estimation. It is a quite challenging work to estimate physical parameters for accurately reproducing the behaviors of deformable objects.

So far, the most popular method used in estimating physical parameters of deformable objects is simulation-based optimization, *i.e.*, the simulation is iterated with updated physical parameters until the difference between the simulation and experiment becomes minimal, as shown in Fig. 1.3. Using this method, many work has been done. For example, Kauer *et al.* (2002) characterized human uteri in vivo through an aspiration experiment; Hing *et al.* (2007) investigated the force behaviors during the insertion of a needle into a porcine liver; Samur *et al.* (2007) developed a robotic indenter for minimally invasive measurements and characterized the material properties of pig liver; Ahn & Kim (2010) characterized a porcine liver by indentation experiments with various indentation depths and two different tip shapes; Tada *et al.* (2005) performed a compression test inside a magnetic resonance imaging (MRI) system and estimated the material properties of a layered soft tissue; Augenstein *et al.* (2005) investigated the physical parameters of pig heart based on cyclical inflation experiments and MRI tagged images with simultaneous pressure recordings; and Ikawa & Noborio (2007) calibrated a food dough which was simulated by a hierarchical MSD model. In order to accomplish the optimization problem of the estimation method, many optimization algorithms have been used, such as Levenberg-Marquardt method [Kauer *et al.* (2002)], sequential quadratic programming (SQP) [Augenstein *et al.* (2005)], genetic algorithm (GA) [Ikawa & Noborio (2007)] and extended Kalman filter [Hoshi *et al.* (2007)].

The optimization-based estimation method is quite robust and works well with different models. However, this method is time-consuming since it is based on iterative simulations.

Direct calculation and curve fitting methods have also been used to estimate physical parameters of deformable objects. Farshad *et al.* (1999) have performed a series of compressive and shear tests on pig kidney and estimated its physical parameters by using curve fitting. Sakamoto *et al.* (2007) formulated a "Norimaki-sushi" by a 2-layered Maxwell model and directly calculated its physical parameters by using least squares method based on the measurements of force and displacements. In order to well capture the force response during the grasping of the "Norimaki-sushi", Tsai *et al.* (2008) used a Fung's viscoelastic model to describe the force behaviors of the sushi and employed curve fitting method to determine the physical parameters. Direct calculation or curve fitting method for estimating parameters are efficient since no simulation was involved. However, this method needs the analytical expressions of force or displacement, which are not always available. Therefore, such method is not always applicable. In this dissertation, both simulation-based and calculation-based methods will be discussed and mixed together to achieve better reproductions of both force and deformation simultaneously.

1.3 Modeling and Parameter Estimation of Rheological Objects

Rheological object has both elastic and plastic properties. Generally, it is more difficult to model a rheological object than model an elastic object due to the presence of residual deformation. Early work on the modeling of rheological objects was started by Terzopoulos & Fleischer (1988), who have employed a Burgers model to describe rheological behaviors. However, it is only a conceptual description and no simulation results and information of parameter determination were given. A plenty of work on modeling and parameter estimation of rheological objects has been done by Noborio *et al.* (2003), who have employed a Lethersich model and MSD method to construct a food dough, a typical rheological object [Nogami *et al.* (2004b)]. They investigated three different mesh configurations: the lattice [Yoshida *et al.* (2005)], the truss [Nogami *et al.* (2004a)], and the hierarchical [Ikawa & Noborio (2007)] structures, with decreased MSD elements connected between nodal points to reduce the computation cost. Two optimization methods, modified randomized algorithm [Noborio *et al.* (2003)] and genetic algorithm [Ikawa & Noborio (2007)], were used to estimate the physical parameters. As we mentioned above, the MSD model has an advantage of low computation cost but the simulation accuracy is quite limited and the physical parameters are dependent on mesh configuration and resolution. A two-layered Maxwell model [Sakamoto *et al.* (2007)] and a Fung's viscoelastic model [Tsai *et al.* (2008)] have been used respectively to reproduce the force response of a sushi when grasped by a robot hand. Good approximations of force behaviors were obtained. However, both models are still 1D models. In addition, the ISU exoskeleton technique has been used in modeling clay to simulate an interaction between virtual clay and a human finger [Chai *et al.* (1998)].

Interestingly, most above-mentioned work of rheological objects modeling has focused on either reproduction of deformation alone [Noborio *et al.* (2003), Nogami *et al.* (2004a), Nogami *et al.* (2004b), Yoshida *et al.* (2005), Ikawa & Noborio (2007)] or reproduction of force alone [Sakamoto *et al.* (2007), Tsai *et al.* (2008)]. Reproduction of both force and deformed shapes of a food dough has been studied by Yoshida *et al.* (2007) with a MSD model. Experimental results suggested that shape calibration (parameter estimation by minimizing the difference of deformed shape) could only yield good shape reproduction and force calibration only resulted in good force reproduction. It is impossible to reproduce both force and deformed shape simultaneously by using one set of parameters. However, they did not mention the reason of this impossibility and how to solve it. This will be the main concern of this dissertation.

On the other hand, rheological properties of food materials were frequently studied in food engineering. Many instruments have been developed to measure rheological properties, such as rheometer, farinograph, and dynamic oscillator, as reviewed by Mirsaeedghazi *et al.* (2008). Sivaramakrishnan *et al.* (2004) have used a farinograph and a rheometer to assess the rheological properties of various types of rice dough to determine their suitability for making rice bread.

Wu *et al.* (2010) have investigated the use of extrusion cooking on pastes by estimating the dynamic rheological properties of extruded flaxseed-maize pastes through dynamic oscillation and creep-recovery tests. However, properties tests and behavior models on food materials are usually carried out in 1D condition and mainly focusing on chemical and ingredient composition. Our work has been motivated from an engineering point of view for grasping and manipulating of rheological objects. Therefore, the object or material investigated in this dissertation basically has a 2D or 3D shape and the deformed shapes are always of concern.

1.4 Aim of the Present Work

As discussed above, the modeling of rheological objects has not been well developed and mostly is based on MSD modeling method or with a 1D assumption. An effective approach for estimating physical parameters of rheological objects has also not been well established. To our knowledge, the residual (permanent) deformation after loading-unloading operation has not been taken into consideration during the modeling and parameter estimation of rheological objects so far. The residual deformation might be important in some situations where the desired shape is needed without any damage. The aim of this dissertation is the determination of appropriate models for simulating rheological objects and of their physical parameters in order to reproduce both rheological force and deformation behaviors simultaneously. In other words, we hope that our present work is able to help us to understand rheological behaviors and to choose an appropriate model and parameters for accurately capturing those behaviors, such as force response, deformed shapes, and final recovered shapes. Possible application fields of our present work may include surgical simulation, food engineering, and robot manipulation.

1.5 Dissertation Organization

In Chapter 2, we summarized the physically-based models which can be used to describe rheological behaviors. According to the configuration among elements, we divided the physically-based models into two groups: serial and parallel models. General constitutive laws for both groups were formulated and analytical expressions of force and residual deformation were derived to discuss the ability of physically-based model for capturing both rheological forces and deformation behaviors. A dual-moduli viscous element was then introduced in order to reproduce both rheological forces and deformation simultaneously.

In Chapter 3, 2D and 3D FE dynamic models were formulated based on generalized Hooke's law and linear Cauchy strain tensor. In order to handle large deformation and deformation with rotation motion, the nonlinear Green strain tensor was introduced into our FE formation. Simulation results with linear Cauchy strain and nonlinear Green strain tensors were then performed to compare the differences. Finally, FE model with the proposed dual-moduli viscous element was presented for capturing both rheological forces and deformation behaviors simultaneously.

In Chapter 4, modeling of non-uniform layered objects and contact interaction between two objects were investigated. The layered objects were artificially separated into several uniform objects and modeled by our FE model. The constraints between interaction boundaries were then imposed to connect these uniform objects to construct the non-uniform ones. The contact models were divided into two categories depended on the size of the instruments. A global or local remeshing was needed for the second category but not necessary for the first one. The contact moment was detected by using a definition of signed area. A contact condition was established to start the contact simulation. Surprisingly, the losing contact action can be achieve automatically by using this condition as well. The losing contact moment also can serve as a criterion required in the dual-moduli viscous element to switch parameters.

In Chapter 5, the parameter estimation methods were studied for reproducing both rheological forces and deformation behaviors simultaneously. At first, the influences of physical parameters and mesh resolution on simulation results were investigated. Secondly, a three-step estimation method was presented based on simulation-based optimization with a constraint on the summation of viscous moduli. By taking the advantages of analytical expressions of rheological forces, a calculation-based optimization method was then proposed. Finally, the method for estimating parameters of FE model with dual-moduli viscous elements was presented.

In Chapter 6, experimental results with commercial available clay and Japanese sweets materials were presented. A series of compressive tests on flat-squared objects made of above-mentioned materials were performed with different compressing operations. Measurements of force and deformed shapes were utilized to estimate the physical parameters of both materials. Different parameter estimation methods were employed to estimate the parameters. Validation results of both FE model and estimated parameters were then investigated by comparing the simulation results with experimental measurements.

Chapter 7 concluded this dissertation and suggested possible directions and applications of future work.

Chapter 2

Physically-Based Models

Physically-based models are often employed to describe deformable materials and objects, *e.g.*, an elastic element (Fig. 2.1a) and a viscous element (Fig. 2.1b) represent ideal elastic and viscous material, respectively. Note that the deformation generated in an elastic element is completely recoverable while the deformation generated in a viscous element will be totally maintained after loading-unloading operations. An elastic and a viscous elements connected in series is called a Maxwell element (Fig. 2.1c), which denotes a simplest rheological material. An elastic and a viscous elements connected in parallel is called a Kelvin (or Kelvin-Voigt) element (Fig. 2.1d), which denotes a visco-elastic material. We shall call the above four elements as basic elements (Fig. 2.1). By connecting several basic elements in different configurations, many physically-based models can be obtained for simulating rheological behaviors. We categorized such models into two

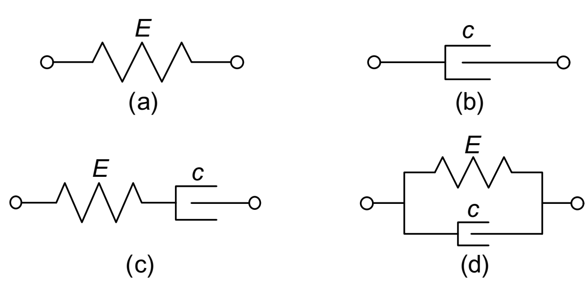

Figure 2.1: The basic elements for describing deformable materials: (a) the elastic; (b) the viscous; (c) the Maxwell; and (d) the Kelvin elements.

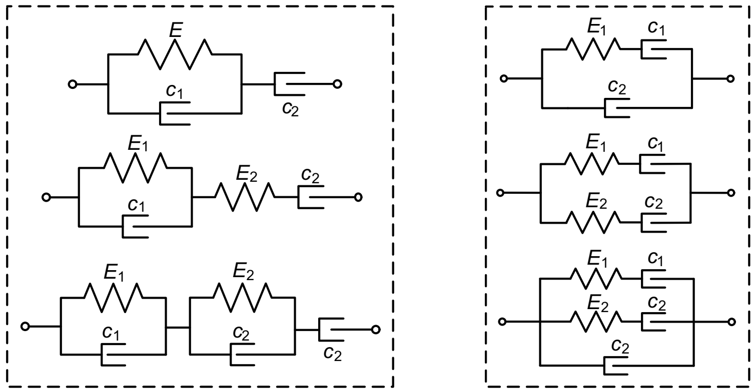

(a) (b)

Figure 2.2: Two groups of rheological physically-based models: (a) serial models, and (b) parallel models.

groups: serial and parallel models, as shown in Fig. 2.2.

2.1 Generalized Serial Model

A serial rheological model consists of numbers of Kelvin elements and a viscous or a Maxwell element connected in series. Note that the deformation generated in an elastic or a Kelvin element is completely recoverable. Therefore, a serial rheological model must include a viscous element connected in series, which causes the residual (permanent) deformation. According to the presence of elastic element, serial models can be further divided into two types, as shown in Fig. 2.3. Let us

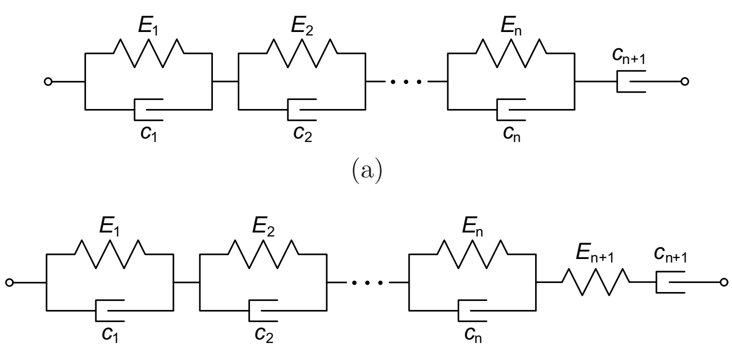

(b)

Figure 2.3: Generalized serial models: (a) type 1, and (b) type 2.

take the serial model of type 1 (Fig. 2.3a) as an example to show the derivation procedure of the constitutive law.

Note that the constitutive law of four basic elements can be formulated as:

$$\begin{aligned} \text{Elastic element}: &\quad \sigma = E\epsilon, \\ \text{Viscous element}: &\quad \sigma = c\dot{\epsilon}, \\ \text{Maxwell element}: &\quad \dot{\sigma} + \frac{E}{c}\sigma = E\dot{\epsilon}, \\ \text{Kelvin element}: &\quad \sigma = E\epsilon + c\dot{\epsilon}, \end{aligned} \tag{2.1}$$

Let ϵ_i and ϵ_{n+1} be the strain at the i-th Kelvin element and the $(n+1)$-th viscous element, respectively, in type 1 serial model. Let E_i and c_i be the Young's modulus and viscous modulus of the i-th elastic and viscous elements, respectively. Due to the serial connections among these basic elements, the total stress at the serial model is equal to the stress at each basic element and the total strain at the serial model is equal to the summation of the strain at each basic element. That is,

$$\begin{aligned} \sigma &= E_i\epsilon_i + c_i\dot{\epsilon}_i, \quad 1 \le i \le n, \\ \sigma &= c_{n+1}\dot{\epsilon}_{n+1}, \\ \epsilon &= \sum_{i=1}^{n+1} \epsilon_i. \end{aligned} \tag{2.2}$$

Taking Laplace transform of the above equations, we have

$$\begin{aligned} \sigma(s) &= E_i\epsilon_i(s) + c_i s\epsilon_i(s), \quad 1 \le i \le n, \\ \sigma(s) &= c_{n+1}s\epsilon_{n+1}(s), \\ \epsilon(s) &= \sum_{i=1}^{n+1} \epsilon_i(s). \end{aligned} \tag{2.3}$$

Eliminating $\epsilon_i(s)$ from the above equations, we then have

$$\epsilon(s) = \Big[\Big(\sum_{i=1}^{n} \frac{1}{s+r_i}\frac{1}{c_i}\Big) + \Big(\frac{1}{s}\frac{1}{c_{n+1}}\Big)\Big]\sigma(s), \tag{2.4}$$

where $r_i = E_i/c_i$. Let us define a polynomial as below:

$$\prod_{i=1}^{n}(s+r_i) = A_n s^n + A_{n-1}s^{n-1} + \cdots + A_1 s + A_0. \tag{2.5}$$

The coefficients of the above polynomial have the forms of:

$$
\begin{aligned}
A_n &= 1, \\
A_{n-1} &= \sum_{i=1}^{n} r_i, \\
A_{n-2} &= \sum_{i=1}^{n} \sum_{\substack{j=1 \\ j \neq i}}^{n} r_i r_j, \\
A_{n-3} &= \sum_{i=1}^{n} \sum_{\substack{j=1 \\ j \neq i}}^{n} \sum_{\substack{k=1 \\ k \neq i \\ k \neq j}}^{n} r_i r_j r_k, \\
&\cdots \\
A_0 &= \prod_{i=1}^{n} r_i.
\end{aligned}
\tag{2.6}
$$

Multiplying Eq. 2.4 by Eq. 2.5, we have

$$
\begin{aligned}
\prod_{i=1}^{n}(s+r_i)\epsilon(s) &= \prod_{i=1}^{n}(s+r_i)\Big[\big(\sum_{i=1}^{n}\frac{1}{s+r_i}\frac{1}{c_i}\big)+\big(\frac{1}{s}\frac{1}{c_{n+1}}\big)\Big]\sigma(s) \\
&= \Big[\sum_{i=1}^{n}\prod_{\substack{j=1 \\ j \neq i}}^{n}\frac{(s+r_j)}{c_i}+\prod_{j=1}^{n}\frac{s+r_j}{s}\frac{1}{c_{n+1}}\Big]\sigma(s).
\end{aligned}
\tag{2.7}
$$

We then find the following equation:

$$
\begin{aligned}
\prod_{\substack{j=1 \\ j \neq i}}^{n}(s+r_j) &= (s+r_1)\cdots(s+r_{i-1})(s+r_{i+1})\cdots(s+r_n) \\
&= s^{n-1}+B_{i,1}s^{n-2}+\cdots+B_{i,n-2}s+B_{i,n-1},
\end{aligned}
\tag{2.8}
$$

where

$$
\begin{aligned}
B_{i,1} &= \sum_{\substack{j=1\\ j\neq i}}^{n} r_j, \\
B_{i,2} &= \sum_{\substack{j=1\\ j\neq i}}^{n} \sum_{\substack{k=1\\ k\neq i\\ k\neq j}}^{n} r_j r_k, \\
B_{i,3} &= \sum_{\substack{j=1\\ j\neq i}}^{n} \sum_{\substack{k=1\\ k\neq i\\ k\neq j}}^{n} \sum_{\substack{l=1\\ l\neq i\\ l\neq j\\ l\neq k}}^{n} r_j r_k r_l, \\
&\cdots \\
B_{i,n-1} &= \prod_{\substack{j=1\\ j\neq i}}^{n} r_j.
\end{aligned}
\tag{2.9}
$$

Substituting Eqs. 2.5 and 2.8 into Eq. 2.7, we have the following Laplace transform equation:

$$
\begin{aligned}
&(A_n s^{n+1} + A_{n-1} s^n + \cdots + A_0 s)\epsilon(s) \\
&\qquad = (B_n^{s1} s^n + B_{n-1}^{s1} s^{n-1} + \cdots + B_1^{s1} s + B_0^{s1})\sigma(s),
\end{aligned}
\tag{2.10}
$$

where

$$
\begin{aligned}
B_n^{s1} &= \sum_{i=1}^{n} \frac{1}{c_i} + \frac{A_n}{c_{n+1}}, \\
B_{n-1}^{s1} &= \sum_{i=1}^{n} \frac{B_{i,1}}{c_i} + \frac{A_{n-1}}{c_{n+1}}, \\
&\cdots \\
B_1^{s1} &= \sum_{i=1}^{n} \frac{B_{i,n-1}}{c_i} + \frac{A_1}{C_{n+1}}, \\
B_0^{s1} &= \frac{A_0}{c_{n+1}}.
\end{aligned}
\tag{2.11}
$$

Applying the inverse Laplace transform to Eq. 2.10 yields the constitutive law of serial model of type 1 as follows:

$$
\sum_{i=1}^{n+1} A_{i-1} \frac{\partial^i \epsilon}{\partial t^i} = \sum_{j=0}^{n} B_j^{s1} \frac{\partial^j \sigma}{\partial t^j}. \tag{2.12}
$$

Note that the highest-order derivative of strain ϵ is one order larger than the highest-order of stress σ. In addition, there is no constant term in the coefficients of strain polynomial (the subscript i starts from 1 in the left side of Eq. 2.12).

Following the same derivation procedure, we can obtain the constitutive law of serial model of type 2 as follows:

$$\sum_{i=1}^{n+1} A_{i-1} \frac{\partial^i \epsilon}{\partial t^i} = \sum_{j=0}^{n+1} B_j^{s2} \frac{\partial^j \sigma}{\partial t^j}, \tag{2.13}$$

where

$$\begin{aligned} B_{n+1}^{s2} &= \frac{1}{E_{n+1}}, \\ B_n^{s2} &= \sum_{i=1}^{n} \frac{1}{c_i} + \frac{A_n}{c_{n+1}} + \frac{A_{n-1}}{E_{n+1}}, \\ B_{n-1}^{s2} &= \sum_{i=1}^{n} \frac{B_{i,1}}{c_i} + \frac{A_{n-1}}{c_{n+1}} + \frac{A_{n-2}}{E_{n+1}}, \\ &\cdots \\ B_0^{s2} &= \frac{A_0}{c_{n+1}}. \end{aligned} \tag{2.14}$$

Equation 2.13 indicates that the highest-order derivative of strain ϵ is equal to the highest-order of stress σ. Note that the left side of Eq. 2.13 has the same form with the left side of Eq. 2.12.

2.2 Generalized Parallel Models

Two kinds of parallel rheological models were shown in Fig. 2.4. Due to the parallel connections among basic elements, the total strain at the parallel model is equal to the strain at each basic element and the total stress at the parallel model is equal to the summation of the stress at each basic element. For parallel model of type 1, we therefore have

$$\begin{aligned} \dot{\sigma}_i + \frac{E_i}{c_i}\sigma_i &= E_i\dot{\epsilon}, \quad 1 \le i \le n, \\ \sigma_{n+1} &= c_{n+1}\dot{\epsilon}, \\ \sigma &= \sum_{i=1}^{n+1} \sigma_i. \end{aligned} \tag{2.15}$$

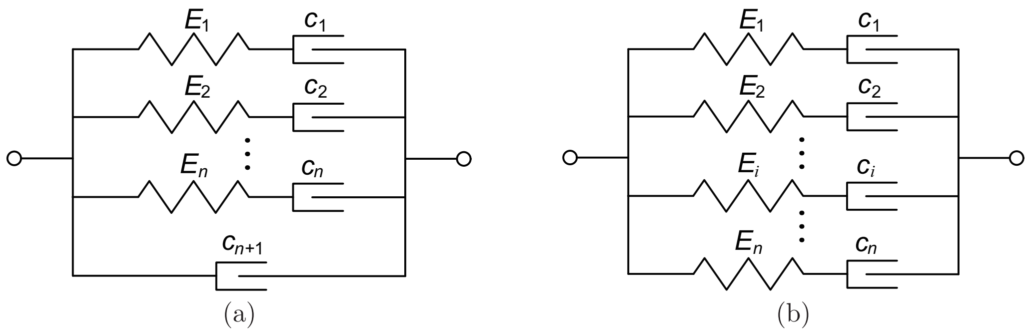

Figure 2.4: Generalized parallel models: (a) type 1; and (b) type 2.

Following the same derivation with serial models, we can end up with the constitutive law of parallel model of type 1 (Fig. 2.4a) as follows:

$$\sum_{i=0}^{n} A_i \frac{\partial^i \sigma}{\partial t^i} = \sum_{j=1}^{n+1} B_j^{p1} \frac{\partial^j \epsilon}{\partial t^j}, \tag{2.16}$$

where

$$\begin{aligned} B_{n+1}^{p1} &= c_{n+1}, \\ B_n^{p1} &= \sum_{i=1}^{n} E_i + A_{n-1} c_{n+1}, \\ B_{n-1}^{p1} &= \sum_{i=1}^{n} B_{i,1} E_i + A_{n-2} c_{n+1}, \\ &\cdots \\ B_1^{p1} &= \sum_{i=1}^{n} B_{i,n-1} E_i + A_0 c_{n+1}. \end{aligned} \tag{2.17}$$

Correspondingly, the constitutive law of parallel model of type 2 (Fig. 2.4b) can be formulated as:

$$\sum_{i=0}^{n} A_i \frac{\partial^i \sigma}{\partial t^i} = \sum_{j=1}^{n} B_j^{p2} \frac{\partial^j \epsilon}{\partial t^j}, \tag{2.18}$$

where

$$
\begin{aligned}
B_n^{p2} &= \sum_{i=1}^{n} E_i, \\
B_{n-1}^{p2} &= \sum_{i=1}^{n} B_{i,1} E_i, \\
&\cdots \\
B_1^{p2} &= \sum_{i=1}^{n} B_{i,n-1} E_i.
\end{aligned} \tag{2.19}
$$

We summarize the constitutive laws of generalized serial and parallel models in Table 2.1, where Eqs. 2.12 and 2.13 are rearranged for convenient comparisons. We found that the constitutive law of serial model of type 1 has the identical form with the parallel model of type 1 except some coefficients having different formulations. Correspondingly, the constitutive laws of serial model of type 2 also has the same form with the parallel model of type 2 by replacing the summation limit $n+1$ by n. Note that same constitutive laws yield same deformation behaviors. Therefore, for simulating a certain behavior, we can use either a serial model or a parallel model. Actually, for any type of physically-based model, which consists of any numbers of basic elements connected in any configuration, we are always able to find one pair of serial and parallel models which are corresponding to each other and yield the same behaviors. This allows us to investigate only one kind of model instead of both for simulating a certain behaviors of deformable objects. In this dissertation, we mainly investigate the parallel models. In addition, according to Eq. 2.2, if the total stress at the serial model is available,

Table 2.1: The constitutive laws of generalized serial and parallel models

Models	Type	The constitutive law
Serial	1	$\sum_{j=0}^{n} B_j^{s1} \frac{\partial^j \sigma}{\partial t^j} = \sum_{i=1}^{n+1} A_{i-1} \frac{\partial^i \epsilon}{\partial t^i}$
	2	$\sum_{j=0}^{n+1} B_j^{s2} \frac{\partial^j \sigma}{\partial t^j} = \sum_{i=1}^{n+1} A_{i-1} \frac{\partial^i \epsilon}{\partial t^i}$
Parallel	1	$\sum_{i=0}^{n} A_i \frac{\partial^i \sigma}{\partial t^i} = \sum_{j=1}^{n+1} B_j^{p1} \frac{\partial^j \epsilon}{\partial t^j}$
	2	$\sum_{i=0}^{n} A_i \frac{\partial^i \sigma}{\partial t^i} = \sum_{j=1}^{n} B_j^{p2} \frac{\partial^j \epsilon}{\partial t^j}$

we can easily obtain the strain at each basic element by solving a series of ordinary differential equations and therefore have the total strain by summing up the individual strain at each element. On the other hand, equation 2.15 indicates that the convenient calculation of rheological stress can be achieved by using the parallel models. This tells us how to choose a model between serial and parallel models. If you are interested in the calculation of deformation, you should use a serial model. On the contrary, you should go with parallel models if you have more concern with force behaviors. In this dissertation, we choose parallel models because the experimental measurements including continuous force responses and static images of deformed shapes. We suppose that the continuous deformation measurements are not available.

2.3 Analysis of Parallel Models

2.3.1 Experimental Rheological Behaviors

Typical rheological behaviors (force and deformed shapes) of commercial available clay and Japanese sweets material are shown in Figs. 2.5 and 2.6. Clays were bought from supermarket and were supposed to be played by children above 3 years old. The sweets materials were provided by OIMATU, a sweets company in Kyoto. Detailed experimental setup and results will be presented in Chapter 6.

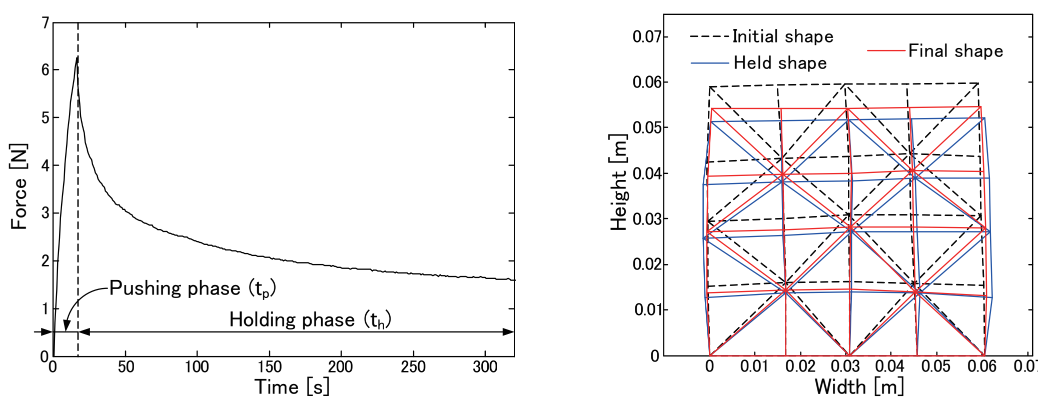

(a) (b)

Figure 2.5: Experimental measurements of commercial available clay: (a) force response, and (b) deformed shapes.

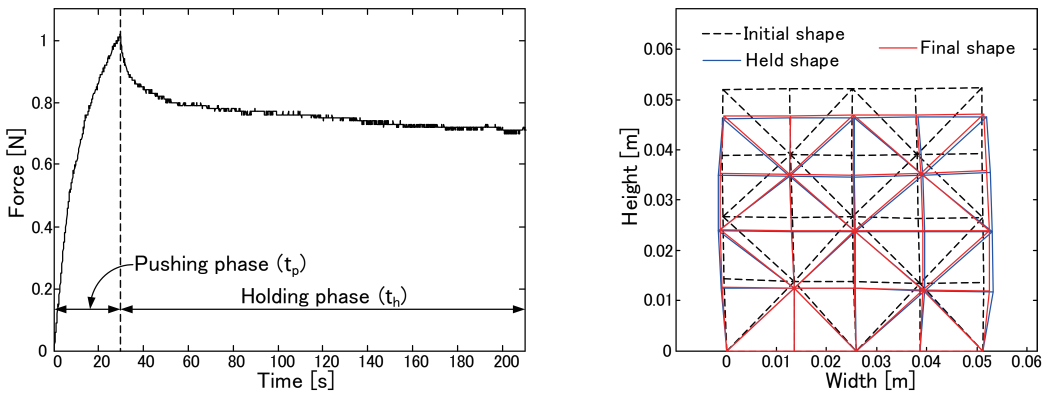

(a) (b)

Figure 2.6: Experimental measurements of Japanese sweets material: (a) force response, and (b) deformed shapes.

Our target is to find an appropriate model to simulate the rheological behaviors of these objects. Normally, physical parameters of an object should keep the same even though its size may change or it may be deformed in different ways. This feature allows us to use a regular shaped object with simple tests to estimate the properties of the object. Such tests include the uniaxial compressive and tensile tests as used in material engineering. In our study, we conducted a compressive test with a pushing-holding-releasing procedure. We fashioned a 2D rheological object with a flat-squared shape. We firstly pushed the entire top surface of the object with a constant velocity to reach a desired displacement during time 0 to t_p, which was called pushing phase (Figs. 2.5a and 2.6a). During this phase, force was increasing with the deformation increasing. Before releasing, the deformed shape was maintained from time t_p to $t_p + t_h$. This time period was called holding phase and the deformed shape during this phase was called held-shape (Figs. 2.5b and 2.6b). In the holding phase, rheological force was decreasing (called force relaxation) in a nonlinear manner. After unloading, however, rheological force went to zero and the deformed shape were partially recovered. Figures 2.5 and 2.6 also indicate that rheological behaviors of different materials are quite different. Comparing with clay, the force relaxation behavior of sweets material is slower and the residual deformation is larger. Let us now investigate the ability of physically-based models for reproducing the above-mentioned rheological behaviors.

2.3.2 Analytical Expressions of Rheological Stresses

We take the parallel model of type 1 as an example to show the derivations of analytical expressions of rheological stresses. During the pushing phase, the strain rate is constant, *i.e.*, $\dot{\epsilon} = p$. By solving Eq. 2.15, we have the analytical stress expression in the pushing phase as below:

$$\sigma(t) = \sum_{i=1}^{n} c_i p\big(1 - e^{-\frac{E_i}{c_i}t}\big) + c_{n+1}p, \quad (0 \leq t \leq t_p). \tag{2.20}$$

In the holding phase, solving Eq. (2.15) with $\dot{\epsilon} = 0$ and initial condition of $\sigma_i(t_p)$, we can formulate the analytical stress expression in this phase as:

$$\sigma(t) = \sum_{i=1}^{n} c_i p\big(1 - e^{-\frac{E_i}{c_i}t_p}\big)e^{-\frac{E_i}{c_i}(t-t_p)}, \quad (t_p \leq t \leq t_p + t_h). \tag{2.21}$$

2.3.3 Analytical Expression of Residual Strain

After unloading, we intuitively consider to solve the constitutive law Eq. 2.16 with $\sigma = 0$ to formulate the strain recovering profile over time. Unfortunately, when the order of time derivative of strain ϵ exceeds two, it becomes impossible to solve Eq. 2.16 because we have no information about the initial condition of strain derivatives. Therefore, we turn our attention to focus on each viscous element. Let $\epsilon_i^{ela}(t)$ and $\epsilon_i^{vis}(t)$ be the strain at each elastic and viscous element, respectively. Note that the stress at a Maxwell element is equal to the stress at the elastic element and the viscous element as well. Thus, total stress after unloading can be formulated as:

$$\sigma(t) = \sum_{i=1}^{n+1} \sigma_i(t) = \sum_{i=1}^{n} c_i \dot{\epsilon}_i^{vis}(t) + c_{n+1}\dot{\epsilon}(t) = 0. \tag{2.22}$$

Integrating the above equation from time $t_p + t_h$ to time infinite, we have

$$\sum_{i=1}^{n} c_i \int_{t_p+t_h}^{\infty} \dot{\epsilon}_i^{vis}(t)\mathrm{d}t + c_{n+1}\int_{t_p+t_h}^{\infty} \dot{\epsilon}(t)\mathrm{d}t = 0, \tag{2.23}$$

and thus

$$\sum_{i=1}^{n} c_i\big[\epsilon_i^{vis}(\infty) - \epsilon_i^{vis}(t_p + t_h)\big] + c_{n+1}\big[\epsilon(\infty) - \epsilon(t_p + t_h)\big] = 0. \tag{2.24}$$

It is important to note that the residual strain at every viscous element in a parallel model should be the same and equal to the total residual strain when time goes to infinite, *i.e.*, $\epsilon_1^{vis}(\infty)=\epsilon_2^{vis}(\infty)=\cdots=\epsilon_n^{vis}(\infty)=\epsilon(\infty)$, because all elastic elements completely recovered from the deformation. Thus, equation 2.24 yields

$$\epsilon(\infty) = \sum_{i=1}^{n} \frac{c_i \epsilon_i^{vis}(t_p + t_h)}{\sum_{j=1}^{n+1} c_j} + \frac{c_{n+1}\epsilon(t_p + t_h)}{\sum_{j=1}^{n+1} c_j}. \tag{2.25}$$

In addition, each viscous element has its own constitutive law as $\sigma_i = c_i \dot{\epsilon}_i^{vis}$. Integrating it through time 0 to time $t_p + t_h$ and rearranging it, we have

$$\epsilon_i^{vis}(t_p + t_h) = \frac{1}{c_i} \int_0^{t_p+t_h} \sigma_i(t)\mathrm{d}t. \tag{2.26}$$

Substituting Eq. 2.26 into Eq. 2.25 and considering $\sigma(t) = \sum_{i=1}^{n+1} \sigma_i(t)$, we finally end up with the expression of total residual strain as:

$$\epsilon(\infty) = \frac{1}{\sum_{i=1}^{n+1} c_i} \int_0^{t_p+t_h} \sigma(t)\mathrm{d}t. \tag{2.27}$$

This equation indicates that the final residual strain in a parallel model is dominated by the summation of viscous moduli and the integration of force through the pushing and holding phase.

For the parallel model of type 2, we can obtain the same formulation of stress expression in the holding phase and the same formulation of final residual strain with the summation limit $n + 1$ replaced by n in Eq. 2.27. The only difference of the parallel model of type 2 is the stress expression in the pushing phase, which is

$$\sigma(t) = \sum_{i=1}^{n} c_i p\big(1 - e^{-\frac{E_i}{c_i}t}\big), \quad (0 \leq t \leq t_p). \tag{2.28}$$

2.4 Discussions of Physically-Based Models

Typical simulation results of rheological stress and strain were shown in Fig. 2.7 by using a five-element model (the last row of Fig. 2.2b) and a two-layered Maxwell model (the middle row of Fig. 2.2b). According to Eqs. 2.20, 2.21, and 2.28, we find that the stress curve can be determined by viscous moduli c_i and

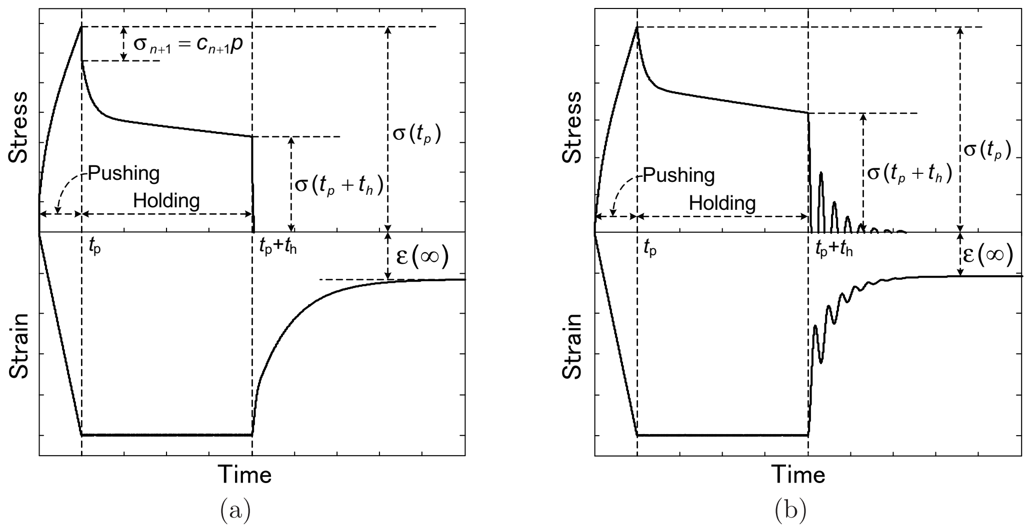

Figure 2.7: Typical simulation results of rheological behaviors by using: (a) 5-element model, and (b) 2-layered Maxwell model.

time coefficients E_i/c_i of exponential functions. The coefficients E_i/c_i dominate the stress relaxation behavior during the holding phase, as formulated in Eq. 2.21 and shown in Fig. 2.7. In order to obtain similar force relaxation curves with real materials as shown in Figs. 2.5 and 2.6, at least two exponential terms are needed [Wang & Hirai (2009)], one with large value of E_i/c_i and another one with small E_i/c_i. The large E_i/c_i describes the rapid relaxation in force and the small one denotes the slow decreasing. For example, figure 2.8 shows the curve fitting results of force relaxation behaviors of commercial clay material by using a force expression with one and two exponential terms, respectively. We can see that two exponential terms are enough to achieve a good reproduction of force relaxation behavior. The values of E_i/c_i used in Fig 2.8b were $E_1/c_1 = 0.2514$ and $E_2/c_2 = 0.00213$. After determining E_i/c_i and substituting into Eq. 2.20, we find that the viscous moduli c_i will dominate peak stress at time t_p. Note that there is a sudden drop in stress (Fig. 2.7a) at the end of pushing phase for five-element model (parallel type 1). This sudden drop is denoted by $\sigma = c_{n+1}p$. Figure 2.7b showed that the two-layered Maxwell model(parallel type 2) results in attenuated vibrations in both stress and strain curves after unloading. Based on the above discussions, we can say that the physically-based models with at least two exponential terms in force expressions have the ability to accurately

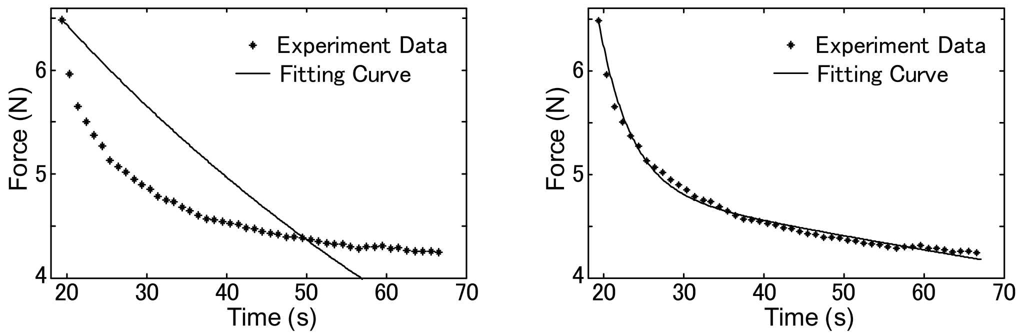

(a) (b)

Figure 2.8: Curve fitting of force relaxation behaviors by using expressions with: (a) one exponential term, and (b) two exponential terms.

reproduce rheological force behaviors. Our work [Wang & Hirai (2009)] has shown good reproductions of rheological forces for commercial clay. However, we failed to reproduce the final recovered shape at the same time. Let us now discuss the reason of this failure.

According to Eq. 2.27, the residual strain is dominated by the summation $\sum_{i=1}^{n+1} c_i$. On the other hand, parameters c_i also strongly affect stress amplitude as formulated in Eqs. 2.20, 2.21, and 2.28. This causes a contradiction between the reproductions of stress and residual strain. For example, if we determine the parameters c_i from stress, the summation of c_i will therefore yields a certain residual strain. We are unable to change this residual strain to another desired one. On the contrary, if we firstly calculate the summation of c_i based on Eq. 2.27, we have an upper limit ($\sum_{i=1}^{n+1} c_i$) for each modulus c_i and we have to keep each c_i under this limit during the reproduction of stress. For some materials, we may be able to achieve a good reproduction of stress with c_i under this limit, as will be presented in Chapter 6. For most materials, however, this limit always will be broken in order to well capture the stress. The above discussions suggest that the physically-based models have some difficulties to reproduce both rheological force and deformation, especially residual deformation, simultaneously. The reason of this difficulty is the linearity of the physically-based models, especially, the linear viscous elements, which dominated both residual strain and stress behaviors.

To solve this problem, the first idea come to our mind is to change the physically-based models. We can add more elements to the physical model or change the configurations of the basic elements. However, this will not work well. Actually, we are able to find a corresponding parallel model for any physical model no matter how many elements are involved and how these elements are connected. We have already discussed that a contradiction phenomenon always exist for arbitrary parallel model. Therefore, we are unable to solve this problem by adding more elements or changing the elements connections in physically-based models. The second idea for solving this problem is to introduce some nonlinear physical models. From textbooks or literatures, we can find some nonlinear physical models, such as the followings:

$$\begin{aligned}
\text{Wertheim (1847)} \quad & \epsilon^2 = a\sigma^2 + b\sigma, \\
\text{Morgan (1960)} \quad & \epsilon = a\sigma^n, \\
\text{Kenedi et al. (1964)} \quad & \sigma = k\epsilon^d, \quad \text{and} \quad \sigma = B\left[e^{ms} - 1\right], \\
\text{Ridge and Wright (1964)} \quad & \epsilon = C + k\sigma^b, \quad \text{and} \quad \epsilon = x + y\log\sigma.
\end{aligned} \tag{2.29}$$

Unfortunately, most of these nonlinear models cannot be extended to 2D/3D FE models. Even some of them may be able to be extended to 2D/3D models, the FE simulation will be very time consuming and it may be impossible to estimate all the parameters. We have tried to introduce some nonlinear models into our FE simulation, but we did not obtain any good result for reproducing both rheological force and residual deformation simultaneously so far. We have therefore turn to another idea which will be introduced in the next section.

2.5 Dual-Moduli Viscous Element

According to the above discussions, we found that the summation $\sum_{i=1}^{n} c_i$ dominates both rheological forces and residual deformation simultaneously. Therefore, it is difficult to use one set of c_i to capture both force and residual deformation simultaneously. In addition, we found that one set of c_i is enough to capture both force and deformation behaviors during operations, such as pushing and holding phase. However, this set of parameter c_i cannot guarantee good reproduction of residual deformation. It is also clear that the force response goes to zero immediately after releasing. During deformation recovery, we do not concern about force any more. Therefore, we are able to use another set of c_i to capture residual

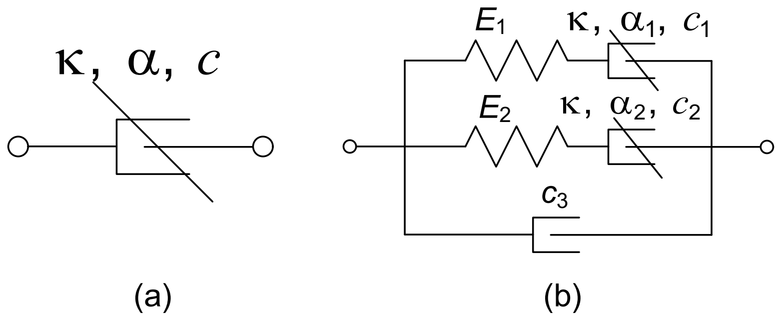

Figure 2.9: (a) the dual-moduli viscous element and (b) parallel 5-element model with two dual-moduli viscous elements.

deformation. We can switch these two sets of parameters during simulation when the deformation starts to recover. We have therefore introduced a dual-moduli viscous element, as shown in Fig. 2.9a into our physically-based model in order to reproduce both rheological force and deformation, especially residual deformation simultaneously. The governing equation for the dual-moduli viscous element can be formulated as

$$\sigma(t) = (\kappa\alpha + c)\dot{\epsilon}(t), \tag{2.30}$$

where scalars α and c were parameters to be determined. Switch function κ takes the following values:

$$\kappa = \begin{cases} 1 & \text{Criterion is satisfied,} \\ -1 & \text{Otherwise.} \end{cases} \tag{2.31}$$

This dual-moduli viscous element has an ability to switch the parameters from one to the other during simulation. The physical meaning of this element can be explained as the property changing of a material during operation and recovery. For example, some elastic materials experience a hysteresis phenomenon during loading and unloading operations. The material properties are slightly changed during hysteresis. In addition, some metal materials also demonstrate strain hardening behavior when they are strained beyond the yield point. In this case, the properties of the materials are also changed during the operation. For rheological materials, both hysteresis and strain hardening may also happen and may be in more stronger way. This causes the material properties changing significantly during loading and the materials therefore behave in another way after unloading. In other words, the physical parameters of rheological objects may be continuously changing during operations and reach another set of values when operations are finished. Unfortunately, continuous change of parameters during operation brings troubles in implement of parameter estimation. In our work, therefore, we suppose that the parameters are kept constants during operation and change to another set when the operation is finished.

The criterion used in Eq. 2.31 has different options depending on different applications. If the operation time is available before simulation, the simulation time can be a perfect criterion to trigger the parameter switching. In some applications such as surgical training and virtual reality, the simulation time may be not available in advance. Fortunately in such cases, an interaction often happens between the object and external instruments. This interaction can provide a good criterion for the parameter switching since the deformation recovery normally happens after the interaction was finished. This will be further investigated in Chapter 4. By introducing two dual-moduli viscous elements into a parallel five-element model, we can formulate an effective model (Fig. 2.9b) for capturing both rheological forces and deformation behaviors.

2.6 Concluding Remarks

In this chapter, the physically-based models for simulating rheological behaviors were summarized. We categorized such models into two groups: serial and parallel models. The constitutive laws for both generalized serial and parallel models were derived. We surprisingly found that the serial and parallel models are corresponding to each other and can be replaced by each other. This allowed us to focus on one group only and save us much time to go over various kinds of physically-based models. We also found that the serial models yield easy calculation of strain while the parallel models result in convenient calculation of stress. This suggested us how to choose the models between both groups depending on our applications. Analytical expressions of rheological stress and residual strain were derived and compared with rheological behaviors of real material. We found that at least two exponential terms in stress expressions are required to accurately reproduce the rheological stress behaviors. We also found the value of summation $\sum_{i=1}^{n} c_i$ dominates the residual strain and strongly affect the force amplitude as well. There is a contradiction between the reproductions of rheological forces and residual deformation. The linear physically-based models have troubles to capture both rheological forces and deformation behaviors simultaneously. We have therefore introduced a dual-moduli viscous element into our physically-based model to cope with this problem. This model has an ability to switch parameters from one to the other during simulation and each set of parameters was responsible for capturing rheological forces and residual deformation respectively. The physical meaning of this element can be explained as hysteresis and strain hardening behaviors of rheological objects. In the following chapters, the FE dynamic models, parameter estimation methods, and experimental results will be addressed.

Chapter 3

2D/3D FE Dynamic Model

FEM is the most successful method for numerical computation of object deformation. In FE modeling, an object is described by a set of elements (*e.g.*, triangles in 2D case or tetrahedra in 3D case). Dynamic behaviors of the object are then determined by analyzing the behaviors of individual element. In this chapter, we formulate the 2D/3D dynamic model of deformable objects based on the linear Cauchy and nonlinear Green strain tensors, respectively. We firstly derive the FE model of elastic material and then extended to rheological material.

3.1 FE Formulation with Cauchy Strain Tensor

3.1.1 2D Elastic Model

Linear elastic material (*e.g.*, a linear spring) in 1D deformation satisfies the following equation:

$$\sigma = E\epsilon, \tag{3.1}$$

where σ and ϵ are stress and strain. Constant E denotes Young's modulus. According to the Hooke's law, the above 1D relationship can be extended to 2D deformation for an isotropic material as

$$\sigma = (\lambda \mathbf{I}_\lambda + \mu \mathbf{I}_\mu)\epsilon, \tag{3.2}$$

where $\sigma = [\sigma_{xx}, \sigma_{yy}, \sigma_{xy}]^{\mathrm{T}}$ and $\epsilon = [\epsilon_{xx}, \epsilon_{yy}, \epsilon_{xy}]^{\mathrm{T}}$ are 2D stress and linear Cauchy strain tensors. Scalars λ and μ denote Lamé's constants, which can be calculated by Young's modulus E and Poisson's ratio γ as follows:

$$\lambda = \frac{\gamma E}{(1+\gamma)(1-2\gamma)}, \qquad \mu = \frac{E}{2(1+\gamma)}. \tag{3.3}$$

Constant matrices $\mathbf{I}_\lambda$ and $\mathbf{I}_\mu$ have the forms of

$$\mathbf{I}_\lambda = \begin{bmatrix} 1 & 1 & 0 \\ 1 & 1 & 0 \\ 0 & 0 & 0 \end{bmatrix}, \qquad \mathbf{I}_\mu = \begin{bmatrix} 2 & 0 & 0 \\ 0 & 2 & 0 \\ 0 & 0 & 1 \end{bmatrix}. \tag{3.4}$$

Let S be a region of a 2D elastic object. Assuming that the object is composed of linear elastic material, strain energy of the object is formulated as follows:

$$U = \int_S \frac{1}{2} \epsilon^{\mathrm{T}} \left(\lambda \mathbf{I}_\lambda + \mu \mathbf{I}_\mu \right) \epsilon h \, \mathrm{d}S.$$

Partitioning region S into a set of triangles, strain energy is described as

$$U = \sum_{\triangle \mathrm{P}_i \mathrm{P}_j \mathrm{P}_k} U_{i,j,k},$$

where

$$U_{i,j,k} = \int_{\triangle \mathrm{P}_i \mathrm{P}_j \mathrm{P}_k} \frac{1}{2} \epsilon^{\mathrm{T}} \left(\lambda \mathbf{I}_\lambda + \mu \mathbf{I}_\mu \right) \epsilon h \, \mathrm{d}S. \tag{3.5}$$

In the region of $\triangle \mathrm{P}_i \mathrm{P}_j \mathrm{P}_k$, displacement vector $\mathbf{u}_{\mathrm{P}} = [u, v]^{\mathrm{T}}$ at arbitrary point P inside $\triangle \mathrm{P}_i \mathrm{P}_j \mathrm{P}_k$ can be approximated by a linear combination of nodal displacements $\mathbf{u}_i = [u_i, v_i]^{\mathrm{T}}$, $\mathbf{u}_j = [u_j, v_j]^{\mathrm{T}}$, and $\mathbf{u}_k = [u_k, v_k]^{\mathrm{T}}$ as follows:

$$\begin{aligned} u &= u_i N_{i,j,k} + u_j N_{j,k,i} + u_k N_{k,i,j}, \\ v &= v_i N_{i,j,k} + v_j N_{j,k,i} + v_k N_{k,i,j}, \end{aligned} \tag{3.6}$$

where $N_{i,j,k}$, $N_{j,k,i}$, and $N_{k,i,j}$ are the interpolating shape functions. Each of them has a value of 1 at each nodal point P_i, P_j, or P_k, respectively and zeros at all other nodal points. Taking partial derivatives of u and v relative to x and y respectively, we have

$$\begin{aligned} \frac{\partial u}{\partial x} &= u_i \frac{\partial N_{i,j,k}}{\partial x} + u_j \frac{\partial N_{j,k,i}}{\partial x} + u_k \frac{\partial N_{k,i,j}}{\partial x}, \\ \frac{\partial u}{\partial y} &= u_i \frac{\partial N_{i,j,k}}{\partial y} + u_j \frac{\partial N_{j,k,i}}{\partial y} + u_k \frac{\partial N_{k,i,j}}{\partial y}, \\ \frac{\partial v}{\partial x} &= v_i \frac{\partial N_{i,j,k}}{\partial x} + v_j \frac{\partial N_{j,k,i}}{\partial x} + v_k \frac{\partial N_{k,i,j}}{\partial x}, \\ \frac{\partial v}{\partial y} &= v_i \frac{\partial N_{i,j,k}}{\partial y} + v_j \frac{\partial N_{j,k,i}}{\partial y} + v_k \frac{\partial N_{k,i,j}}{\partial y}. \end{aligned} \tag{3.7}$$

Let $[\xi_i, \eta_i]^{\mathrm{T}}$, $[\xi_j, \eta_j]^{\mathrm{T}}$, and $[\xi_k, \eta_k]^{\mathrm{T}}$ be initial coordinates of nodal points P_i, P_j, and P_k, respectively. Partial derivatives of shape functions in Eq. 3.7 can be calculated as:

$$\begin{aligned}
N_{ix} &= \frac{\partial N_{i,j,k}}{\partial x} = \frac{\eta_j - \eta_k}{2\triangle}, \quad N_{iy} = \frac{\partial N_{i,j,k}}{\partial y} = -\frac{\xi_j - \xi_k}{2\triangle}, \\
N_{jx} &= \frac{\partial N_{j,k,i}}{\partial x} = \frac{\eta_k - \eta_i}{2\triangle}, \quad N_{jy} = \frac{\partial N_{j,k,i}}{\partial y} = -\frac{\xi_k - \xi_i}{2\triangle}, \\
N_{kx} &= \frac{\partial N_{k,i,j}}{\partial x} = \frac{\eta_i - \eta_j}{2\triangle}, \quad N_{ky} = \frac{\partial N_{k,i,j}}{\partial y} = -\frac{\xi_i - \xi_j}{2\triangle},
\end{aligned} \tag{3.8}$$

where $\triangle$ denotes the signed area of triangle $\triangle \mathrm{P}_i\mathrm{P}_j\mathrm{P}_k$ and was given by

$$\triangle \mathrm{P}_i\mathrm{P}_j\mathrm{P}_k = \frac{1}{2}\begin{bmatrix} \xi_i & \xi_j & \xi_k \end{bmatrix} \begin{bmatrix} \eta_j - \eta_k \\ \eta_k - \eta_i \\ \eta_i - \eta_j \end{bmatrix}.$$

Note that the Cauchy strain tensor $\epsilon = [\epsilon_{xx}, \epsilon_{yy}, \epsilon_{xy}]^{\mathrm{T}}$ was formulated as

$$\begin{aligned}
\epsilon_{xx} &= \frac{\partial u}{\partial x}, \\
\epsilon_{yy} &= \frac{\partial v}{\partial y}, \\
2\epsilon_{xy} &= \frac{\partial u}{\partial y} + \frac{\partial v}{\partial x}.
\end{aligned} \tag{3.9}$$

Substituting Eqs. 3.7 and 3.8 into Eq. 3.9 and then substituting the consequential Cauchy strain tensor into Eq. 3.5, we have

$$U_{i,j,k} = \frac{1}{2}\begin{bmatrix} \mathbf{u}_i^{\mathrm{T}} & \mathbf{u}_j^{\mathrm{T}} & \mathbf{u}_k^{\mathrm{T}} \end{bmatrix} \mathbf{K}_{i,j,k} \begin{bmatrix} \mathbf{u}_i \\ \mathbf{u}_j \\ \mathbf{u}_k \end{bmatrix}, \tag{3.10}$$

where stiffness matrix $\mathbf{K}_{i,j,k}$ can be decomposed into two as follows:

$$\mathbf{K}_{i,j,k} = \lambda \mathbf{J}_{\lambda}^{i,j,k} + \mu \mathbf{J}_{\mu}^{i,j,k}. \tag{3.11}$$

Matrices $\mathbf{J}_{\lambda}^{i,j,k}$ and $\mathbf{J}_{\mu}^{i,j,k}$ have the following forms:

$$\begin{aligned}
\mathbf{J}_{\lambda}^{i,j,k} &= \frac{h}{4\triangle \mathrm{P}_i\mathrm{P}_j\mathrm{P}_k} \begin{bmatrix} \mathbf{A}_{j,k;\,j,k} & \mathbf{A}_{j,k;\,k,i} & \mathbf{A}_{j,k;\,i,j} \\ \mathbf{A}_{k,i;\,j,k} & \mathbf{A}_{k,i;\,k,i} & \mathbf{A}_{k,i;\,i,j} \\ \mathbf{A}_{i,j;\,j,k} & \mathbf{A}_{i,j;\,k,i} & \mathbf{A}_{i,j;\,i,j} \end{bmatrix}, \\
\mathbf{J}_{\mu}^{i,j,k} &= \frac{h}{4\triangle \mathrm{P}_i\mathrm{P}_j\mathrm{P}_k} \begin{bmatrix} 2\mathbf{B}_{j,k;\,j,k} + \mathbf{C}_{j,k;\,j,k} & 2\mathbf{B}_{j,k;\,k,i} + \mathbf{C}_{j,k;\,k,i} & 2\mathbf{B}_{j,k;\,i,j} + \mathbf{C}_{j,k;\,i,j} \\ 2\mathbf{B}_{k,i;\,j,k} + \mathbf{C}_{k,i;\,j,k} & 2\mathbf{B}_{k,i;\,k,i} + \mathbf{C}_{k,i;\,k,i} & 2\mathbf{B}_{k,i;\,i,j} + \mathbf{C}_{k,i;\,i,j} \\ 2\mathbf{B}_{i,j;\,j,k} + \mathbf{C}_{i,j;\,j,k} & 2\mathbf{B}_{i,j;\,k,i} + \mathbf{C}_{i,j;\,k,i} & 2\mathbf{B}_{i,j;\,i,j} + \mathbf{C}_{i,j;\,i,j} \end{bmatrix},
\end{aligned} \tag{3.12}$$

where

$$
\begin{aligned}
\mathbf{A}_{i,j;l,m} &\triangleq \begin{bmatrix} (\eta_i - \eta_j)(\eta_l - \eta_m) & -(\eta_i - \eta_j)(\xi_l - \xi_m) \\ -(\xi_i - \xi_j)(\eta_l - \eta_m) & (\xi_i - \xi_j)(\xi_l - \xi_m) \end{bmatrix}, \\
\mathbf{B}_{i,j;l,m} &\triangleq \begin{bmatrix} (\eta_i - \eta_j)(\eta_l - \eta_m) & 0 \\ 0 & (\xi_i - \xi_j)(\xi_l - \xi_m) \end{bmatrix}, \\
\mathbf{C}_{i,j;l,m} &\triangleq \begin{bmatrix} (\xi_i - \xi_j)(\xi_l - \xi_m) & -(\xi_i - \xi_j)(\eta_l - \eta_m) \\ -(\eta_i - \eta_j)(\xi_l - \xi_m) & (\eta_i - \eta_j)(\eta_l - \eta_m) \end{bmatrix}.
\end{aligned}
\tag{3.13}
$$

Note that matrices $\mathbf{J}_\lambda^{i,j,k}$ and $\mathbf{J}_\mu^{i,j,k}$ depend on geometric quantities, say, coordinates of nodal points alone. As a result, the global stiffness matrix $\mathbf{K}$ also can be decomposed into two terms as follows:

$$
\mathbf{K} = \lambda \mathbf{J}_\lambda + \mu \mathbf{J}_\mu, \tag{3.14}
$$

where $\mathbf{J}_\lambda$ and $\mathbf{J}_\mu$ are referred to as connection matrices. Both matrices also depend on geometric quantities alone and can be calculated by incorporating matrices $\mathbf{J}_\lambda^{i,j,k}$ and $\mathbf{J}_\mu^{i,j,k}$ of each triangles based on the contribution of each triangle to the whole triangle mesh. Let N be the number of nodal points in an FE triangle mesh. The dimensions of both connection matrices are $2N \times 2N$.

After having the global stiffness matrix $\mathbf{K}$, strain energy of the object was formulated by

$$
U = \frac{1}{2} \mathbf{u}_N^{\mathrm{T}} \mathbf{K} \mathbf{u}_N, \tag{3.15}
$$

where $\mathbf{u}_N$ represents the nodal displacement vector. Taking the derivative of the above strain energy relative to vector $\mathbf{u}_N$, we have the formulation of a set of elastic forces generated on all nodal points as

$$
\mathbf{F}_{2D}^{ela} = \mathbf{K}\mathbf{u}_N = (\lambda \mathbf{J}_\lambda + \mu \mathbf{J}_\mu)\mathbf{u}_N. \tag{3.16}
$$

Comparing Eqs. 3.1, 3.2, and 3.16, we found that the 2D stress-strain relation Eq. 3.2 can be obtained from 1D relation Eq. 3.1 by replacing Young's modulus E by a matrix with two Lamé's constants λ and μ. Furthermore, the 2D FE force-displacement relationship Eq. 3.16 can be obtained from 2D stress-strain relation Eq. 3.2 by replacing σ by $\mathbf{F}_{2D}^{ela}$, ϵ by $\mathbf{u}_N$, $\mathbf{I}_\lambda$ by $\mathbf{J}_\lambda$, and $\mathbf{I}_\mu$ by $\mathbf{J}_\mu$, respectively. In the next section, we extend the 2D elastic formulation to a 2D rheological formulation.

3.1.2 2D Rheological Model

A Maxwell model, as shown in Fig. 2.1(c), is a simplest physical model for simulating rheological behaviors. The Maxwell model consists of an elastic and a viscous elements connected in serial. The 1D stress-strain relationship of the Maxwell model can be formulated as

$$\dot{\sigma} = -\frac{E}{c}\sigma + E\dot{\epsilon}, \tag{3.17}$$

Solving the above ordinary differential equation yields:

$$\sigma(t) = \int_0^t R(t-t')\dot{\epsilon}(t')\mathrm{d}t', \tag{3.18}$$

where $R(t-t') = Ee^{-\frac{E}{c}(t-t')}$ is referred as a relaxation function, which determines the nature of rheological deformation. Replacing two elastic constants λ and μ in Eq. 3.2 by two relaxation functions yields a relaxation matrix in 2D isotropic deformation of the Maxwell model:

$$\mathbf{R}(t-t') = r_\lambda(t-t')\mathbf{I}_\lambda + r_\mu(t-t')\mathbf{I}_\mu, \tag{3.19}$$

where

$$r_\lambda(t-t') = \lambda e^{-\frac{E}{c}(t-t')}, \qquad r_\mu(t-t') = \mu e^{-\frac{E}{c}(t-t')}. \tag{3.20}$$

Replacing $R(t-t')$ in Eq. 3.18 by Eq. 3.19, we have the 2D stress-strain relationship of the Maxwell model as

$$\sigma(t) = \int_0^t \left[r_\lambda(t-t')\mathbf{I}_\lambda + r_\mu(t-t')\mathbf{I}_\mu\right]\dot{\epsilon}(t')\mathrm{d}t'. \tag{3.21}$$

From the above equation, replacing $\sigma(t)$ by $\mathbf{F}_{2D}^{Max}(t)$, ϵ by $\mathbf{u}_N$, $\mathbf{I}_\lambda$ by $\mathbf{J}_\lambda$, $\mathbf{I}_\mu$ by $\mathbf{J}_\mu$, we have the 2D force-displacement relationship of the Maxwell model as

$$\mathbf{F}_{2D}^{Max}(t) = \int_0^t \left[\lambda e^{-\frac{E}{c}(t-t')}\mathbf{J}_\lambda + \mu e^{-\frac{E}{c}(t-t')}\mathbf{J}_\mu\right]\dot{\mathbf{u}}_N(t')\mathrm{d}t'. \tag{3.22}$$

Differentiating the above equation, we finally have

$$\dot{\mathbf{F}}_{2D}^{Max} = -\frac{E}{c}\mathbf{F}_{2D}^{Max} + (\lambda\mathbf{J}_\lambda + \mu\mathbf{J}_\mu)\dot{\mathbf{u}}_N, \tag{3.23}$$

Comparing Eq. 3.17 and Eq. 3.23, we find that the 1D constitutive law of Maxwell model can be easily extended to 2D case by simple replacements as performed above.

Then, let us investigate the formulation of a parallel five-element model, as shown in the last row of Fig. 2.2(b). The parallel five-element model consists of two Maxwell models and one viscous element connected in parallel. Let σ_1, σ_2, and σ_3 be the stress at the first, the second Maxwell models, and the third viscous element, respectively. Let σ and ϵ be the stress and strain at the five-element model. Due to the parallel configuration, the 1D stress-strain relationship can be formulated as:

$$\begin{aligned}
\dot{\sigma}_1 + \frac{E_1}{c_1}\sigma_1 &= E_1\dot{\epsilon}, \\
\dot{\sigma}_2 + \frac{E_2}{c_2}\sigma_2 &= E_2\dot{\epsilon}, \\
\sigma_3 &= c_3\dot{\epsilon}, \\
\sigma &= \sigma_1 + \sigma_2 + \sigma_3.
\end{aligned} \tag{3.24}$$

Following the same replacing procedures presented above, we can easily extend the 1D stress-strain relation Eq. 3.24 to 2D force-displacement relation as:

$$\begin{aligned}
\dot{\mathbf{F}}_1 + \frac{E_1}{c_1}\mathbf{F}_1 &= (\lambda_1^{ela}\mathbf{J}_\lambda + \mu_1^{ela}\mathbf{J}_\mu)\dot{\mathbf{u}}_N, \\
\dot{\mathbf{F}}_2 + \frac{E_2}{c_2}\mathbf{F}_2 &= (\lambda_2^{ela}\mathbf{J}_\lambda + \mu_2^{ela}\mathbf{J}_\mu)\dot{\mathbf{u}}_N, \\
\mathbf{F}_3 &= (\lambda_3^{vis}\mathbf{J}_\lambda + \mu_3^{vis}\mathbf{J}_\mu)\dot{\mathbf{u}}_N, \\
\mathbf{F}_{2D}^{rheo} &= \mathbf{F}_1 + \mathbf{F}_2 + \mathbf{F}_3,
\end{aligned} \tag{3.25}$$

where $\mathbf{F}_1$, $\mathbf{F}_2$, $\mathbf{F}_3$, and $\mathbf{F}_{2D}^{rheo}$ are force vectors corresponding to stress vectors σ_1, σ_2, σ_3, and σ, respectively. Parameters λ_1^{ela}, μ_1^{ela}, λ_2^{ela}, and μ_2^{ela} are Lamé constants corresponding to E_1 and E_2 and can be calculated by Eq. 3.3. Parameters λ_3^{vis} and μ_3^{vis} described the model's viscosity and are defined as

$$\lambda_3^{vis} = \frac{c_3\gamma}{(1+\gamma)(1-2\gamma)}, \qquad \mu_3^{vis} = \frac{c_3}{2(1+\gamma)}. \tag{3.26}$$

Supposing that a 2D object is fixed on the ground and the top surface of the object is pushed downward with a displacement function of $\mathbf{d}(t)$. These two constraints can be formulated as follows by using constraint stabilization method (CSM) [Baumgarte (1972)].

$$\begin{aligned} \mathbf{A}^T \ddot{\mathbf{u}}_N + \mathbf{A}^T(2\omega\dot{\mathbf{u}}_N + \omega^2\mathbf{u}_N) = 0, \\ \mathbf{B}^T(\ddot{\mathbf{u}}_N - \ddot{\mathbf{d}}) + \mathbf{B}^T[2\omega(\dot{\mathbf{u}}_N - \dot{\mathbf{d}}) + \omega^2(\mathbf{u}_N - \mathbf{d})] = 0, \end{aligned} \tag{3.27}$$

where matrices $\mathbf{A}$ and $\mathbf{B}$ denote which nodal points should be constrained on the bottom and top surface, respectively. Scalar ω is a predetermined angular frequency and is set to 2000 for both constraints.

Let $\mathbf{M}$ be an inertia matrix and $\ell_{\mathbf{1}}$ and $\ell_{\mathbf{2}}$ be the Lagrange multipliers which denote a set of constraint forces corresponding to both geometric constraints. Using the Lagrange dynamic method, dynamic equations of the nodal points are given by

$$-\mathbf{F}_{2D}^{rheo} + \mathbf{A}\ell_{\mathbf{1}} + \mathbf{B}\ell_{\mathbf{2}} - \mathbf{M}\ddot{\mathbf{u}}_N = 0. \tag{3.28}$$

Combining Eqs. 3.25, 3.27, 3.28, and considering $\mathbf{v}_N = \dot{\mathbf{u}}_N$, we have a set of differential equations for simulating the 2D FE dynamic behaviors of a rheological object under a pushing or pulling operations. In the next section, the 2D FE model will be extended to 3D model by changing the triangle mesh to tetrahedral mesh and adding the z-axis components in all the matrices and vectors. Figure 3.1 demonstrates 2D simulation results of rheological behaviors. The center part of the top surface of a 2D rheological object was pushed downward from 0 s to 20 s with a constant velocity. The deformation was then maintained for 20 seconds. From 40 s, the deformation started to recover. Figure 3.1f shows the force responses on the bottom surface of the object.

3.1.3 3D FE Model of Rheological Object

In our 3D FE formulation, an object is constructed by a set of tetrahedra. Let P_i be a nodal point of a tetrahedron and $[\xi_i, \eta_i, \zeta_i]^{\mathrm{T}}$ be coordinates of point P_i. Let $\Diamond \mathrm{P}_i\mathrm{P}_j\mathrm{P}_k\mathrm{P}_l$ be a tetrahedron consisting of nodal points P_i, P_j, P_k, and P_l. Note that linear isotropic elastic material satisfies

$$\sigma = \mathbf{D}\epsilon, \tag{3.29}$$

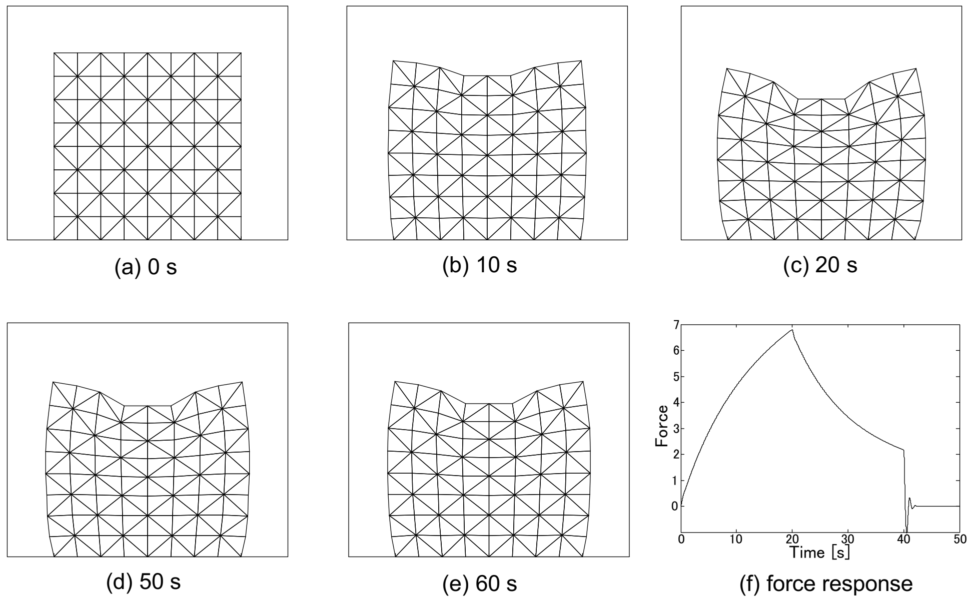

Figure 3.1: Simulation behaviors of a 2D rheological object: initial shape (a), deformed shape (b) at time 10 s, (c) at 20 s, (d) at 50 s, (e) at 60 s, and (f) force response on the bottom surface.

where

$$\mathbf{D} = \begin{bmatrix} \lambda+2\mu & \lambda & \lambda & 0 & 0 & 0 \\ \lambda & \lambda+2\mu & \lambda & 0 & 0 & 0 \\ \lambda & \lambda & \lambda+2\mu & 0 & 0 & 0 \\ 0 & 0 & 0 & \mu & 0 & 0 \\ 0 & 0 & 0 & 0 & \mu & 0 \\ 0 & 0 & 0 & 0 & 0 & \mu \end{bmatrix}.$$

Stress vector σ and linear strain vector ϵ in 3D case are defined as

$$\sigma = [\sigma_{\xi\xi}, \sigma_{\eta\eta}, \sigma_{\zeta\zeta}, \sigma_{\eta\zeta}, \sigma_{\zeta\xi}, \sigma_{\xi\eta}]^{\mathrm{T}},$$
$$\epsilon = [\epsilon_{\xi\xi}, \epsilon_{\eta\eta}, \epsilon_{\zeta\zeta}, 2\epsilon_{\eta\zeta}, 2\epsilon_{\zeta\xi}, 2\epsilon_{\xi\eta}]^{\mathrm{T}}.$$

Performing similar derivation as presented in 2D elastic deformation, we can obtain a stiffness matrix $\mathbf{K}_{i,j,k,l}$ for a tetrahedron $\Diamond \mathrm{P}_i\mathrm{P}_j\mathrm{P}_k\mathrm{P}_l$ as follows:

$$\mathbf{K}_{i,j,k,l} = \lambda \mathbf{J}_{\lambda}^{i,j,k,l} + \mu \mathbf{J}_{\mu}^{i,j,k,l}, \tag{3.30}$$

where

$$\mathbf{J}_\lambda^{i,j,k,l} = \frac{1}{36\Diamond}\begin{bmatrix} \mathbf{A}_{j,k,l;\,j,k,l} & -\mathbf{A}_{j,k,l;\,k,l,i} & \mathbf{A}_{j,k,l;\,l,i,j} & -\mathbf{A}_{j,k,l;\,i,j,k} \\ -\mathbf{A}_{k,l,i;\,j,k,l} & \mathbf{A}_{k,l,i;\,k,l,i} & -\mathbf{A}_{k,l,i;\,l,i,j} & \mathbf{A}_{k,l,i;\,i,j,k} \\ \mathbf{A}_{l,i,j;\,j,k,l} & -\mathbf{A}_{l,i,j;\,k,l,i} & \mathbf{A}_{l,i,j;\,l,i,j} & -\mathbf{A}_{l,i,j;\,i,j,k} \\ -\mathbf{A}_{i,j,k;\,j,k,l} & \mathbf{A}_{i,j,k;\,k,l,i} & -\mathbf{A}_{i,j,k;\,l,i,j} & \mathbf{A}_{i,j,k;\,i,j,k} \end{bmatrix},$$

$$\begin{aligned} \mathbf{J}_\mu^{i,j,k,l} = \frac{1}{36\Diamond}&\begin{bmatrix} 2\mathbf{B}_{j,k,l;\,j,k,l} & -2\mathbf{B}_{j,k,l;\,k,l,i} & 2\mathbf{B}_{j,k,l;\,l,i,j} & -2\mathbf{B}_{j,k,l;\,i,j,k} \\ -2\mathbf{B}_{k,l,i;\,j,k,l} & 2\mathbf{B}_{k,l,i;\,k,l,i} & -2\mathbf{B}_{k,l,i;\,l,i,j} & 2\mathbf{B}_{k,l,i;\,i,j,k} \\ 2\mathbf{B}_{l,i,j;\,j,k,l} & -2\mathbf{B}_{l,i,j;\,k,l,i} & 2\mathbf{B}_{l,i,j;\,l,i,j} & -2\mathbf{B}_{l,i,j;\,i,j,k} \\ -2\mathbf{B}_{i,j,k;\,j,k,l} & 2\mathbf{B}_{i,j,k;\,k,l,i} & -2\mathbf{B}_{i,j,k;\,l,i,j} & 2\mathbf{B}_{i,j,k;\,i,j,k} \end{bmatrix} \\ + \frac{1}{36\Diamond}&\begin{bmatrix} \mathbf{C}_{j,k,l;\,j,k,l} & -\mathbf{C}_{j,k,l;\,k,l,i} & \mathbf{C}_{j,k,l;\,l,i,j} & -\mathbf{C}_{j,k,l;\,i,j,k} \\ -\mathbf{C}_{k,l,i;\,j,k,l} & \mathbf{C}_{k,l,i;\,k,l,i} & -\mathbf{C}_{k,l,i;\,l,i,j} & \mathbf{C}_{k,l,i;\,i,j,k} \\ \mathbf{C}_{l,i,j;\,j,k,l} & -\mathbf{C}_{l,i,j;\,k,l,i} & \mathbf{C}_{l,i,j;\,l,i,j} & -\mathbf{C}_{l,i,j;\,i,j,k} \\ -\mathbf{C}_{i,j,k;\,j,k,l} & \mathbf{C}_{i,j,k;\,k,l,i} & -\mathbf{C}_{i,j,k;\,l,i,j} & \mathbf{C}_{i,j,k;\,i,j,k} \end{bmatrix}. \end{aligned} \tag{3.31}$$

The signed volume of tetrahedron $\Diamond = \Diamond \mathrm{P}_i\mathrm{P}_j\mathrm{P}_k\mathrm{P}_l$ is given by

$$\begin{aligned} \Diamond \mathrm{P}_i\mathrm{P}_j\mathrm{P}_k\mathrm{P}_l &= \Diamond \mathrm{OP}_j\mathrm{P}_k\mathrm{P}_l + \Diamond \mathrm{P}_i\mathrm{OP}_k\mathrm{P}_l + \Diamond \mathrm{P}_i\mathrm{P}_j\mathrm{OP}_l + \Diamond \mathrm{P}_i\mathrm{P}_j\mathrm{P}_k\mathrm{O} \\ &= \Diamond \mathrm{OP}_j\mathrm{P}_k\mathrm{P}_l + \Diamond \mathrm{OP}_k\mathrm{P}_l\mathrm{P}_i + \Diamond \mathrm{OP}_l\mathrm{P}_i\mathrm{P}_j + \Diamond \mathrm{OP}_i\mathrm{P}_j\mathrm{P}_k, \end{aligned} \tag{3.32}$$

where the signed volume of tetrahedron $\Diamond \mathrm{OP}_i\mathrm{P}_j\mathrm{P}_k$ is defined as follows:

$$\Diamond \mathrm{OP}_i\mathrm{P}_j\mathrm{P}_k = \frac{1}{2}\frac{1}{3}\begin{vmatrix} \xi_i & \xi_j & \xi_k \\ \eta_i & \eta_j & \eta_k \\ \zeta_i & \zeta_j & \zeta_k \end{vmatrix}. \tag{3.33}$$

The matrices $\mathbf{A}_{i,j,k;\,l,m,n}$, $\mathbf{B}_{i,j,k;\,l,m,n}$, and $\mathbf{C}_{i,j,k;\,l,m,n}$ in Eq. 3.31 are defined as:

$$\begin{aligned} \mathbf{A}_{i,j,k;\,l,m,n} &\triangleq \begin{bmatrix} a_{i,j,k}a_{l,m,n} & a_{i,j,k}b_{l,m,n} & a_{i,j,k}c_{l,m,n} \\ b_{i,j,k}a_{l,m,n} & b_{i,j,k}b_{l,m,n} & b_{i,j,k}c_{l,m,n} \\ c_{i,j,k}a_{l,m,n} & c_{i,j,k}b_{l,m,n} & c_{i,j,k}c_{l,m,n} \end{bmatrix}, \\ \mathbf{B}_{i,j,k;\,l,m,n} &\triangleq \begin{bmatrix} a_{i,j,k}a_{l,m,n} & 0 & 0 \\ 0 & b_{i,j,k}b_{l,m,n} & 0 \\ 0 & 0 & c_{i,j,k}c_{l,m,n} \end{bmatrix}, \\ \mathbf{C}_{i,j,k;\,l,m,n} &\triangleq \\ &\begin{bmatrix} b_{i,j,k}b_{l,m,n} + c_{i,j,k}c_{l,m,n} & b_{i,j,k}a_{l,m,n} & c_{i,j,k}a_{l,m,n} \\ a_{i,j,k}b_{l,m,n} & c_{i,j,k}c_{l,m,n} + a_{i,j,k}a_{l,m,n} & c_{i,j,k}b_{l,m,n} \\ a_{i,j,k}c_{l,m,n} & b_{i,j,k}c_{l,m,n} & a_{i,j,k}a_{l,m,n} + b_{i,j,k}b_{l,m,n} \end{bmatrix}, \end{aligned} \tag{3.34}$$

where

$$
\begin{aligned}
a_{i,j,k} &= \begin{vmatrix} \eta_i & \eta_j \\ \zeta_i & \zeta_j \end{vmatrix} + \begin{vmatrix} \eta_j & \eta_k \\ \zeta_j & \zeta_k \end{vmatrix} + \begin{vmatrix} \eta_k & \eta_i \\ \zeta_k & \zeta_i \end{vmatrix}, \\
b_{i,j,k} &= \begin{vmatrix} \zeta_i & \zeta_j \\ \xi_i & \xi_j \end{vmatrix} + \begin{vmatrix} \zeta_j & \zeta_k \\ \xi_j & \xi_k \end{vmatrix} + \begin{vmatrix} \zeta_k & \zeta_i \\ \xi_k & \xi_i \end{vmatrix}, \\
c_{i,j,k} &= \begin{vmatrix} \xi_i & \xi_j \\ \eta_i & \eta_j \end{vmatrix} + \begin{vmatrix} \xi_j & \xi_k \\ \eta_j & \eta_k \end{vmatrix} + \begin{vmatrix} \xi_k & \xi_i \\ \eta_k & \eta_i \end{vmatrix}.
\end{aligned}
\tag{3.35}
$$

After having stiffness matrix on each tetrahedron as given in Eq. 3.30, we can calculate the global stiffness matrix as follows by incorporating the contribution of each tetrahedron:

$$
\mathbf{K}^{3D} = \lambda \mathbf{J}_{\lambda}^{3D} + \mu \mathbf{J}_{\mu}^{3D}, \tag{3.36}
$$

The dimensions of connection matrices $\mathbf{J}_{\lambda}^{3D}$ and $\mathbf{J}_{\mu}^{3D}$ are $3N \times 3N$. Therefore, a set of elastic forces $\mathbf{F}_{3D}^{ela}$ can be formulated as:

$$
\mathbf{F}_{3D}^{ela} = \mathbf{K}^{3D} \mathbf{u}_N^{3D} = \left(\lambda \mathbf{J}_{\lambda}^{3D} + \mu \mathbf{J}_{\mu}^{3D} \right) \mathbf{u}_N^{3D}, \tag{3.37}
$$

where vectors $\mathbf{F}_{3D}^{ela}$ and $\mathbf{u}_N^{3D}$ consist of x-, y-, and z-axis components of all nodal points and the dimensions of both vectors are $3N \times 1$. Comparing the above equation and Eq. 3.16, the difference between 2D and 3D FE formulation is the calculation of connection matrices and the configuration of force and displacement vectors. In 3D deformation, the object is constructed with a set of tetrahedra and all the matrices and vectors include the z-axis components in their formulations.

Similarly, we can extend 2D rheological FE formulation to 3D case. Replacing the 2D matrices and vectors in Eqs. 3.25, 3.27, 3.28 and considering $\mathbf{v}_N^{3D} = \dot{\mathbf{u}}_N^{3D}$, we have 3D FE formulation of rheological deformation as follows:

$$
\begin{aligned}
\dot{\mathbf{u}}_N^{3D} &= \mathbf{v}_N^{3D}, \\
\mathbf{M}_{3D}\dot{\mathbf{v}}_N^{3D} &= \mathbf{A}_{3D}\ell_1^{3D} + \mathbf{B}_{3D}\ell_2^{3D} - \mathbf{F}_{3D}^{rheo} + \mathbf{F}_{3D}^{ext}, \\
-\mathbf{A}_{3D}^T\dot{\mathbf{v}}_N^{3D} &= \mathbf{A}_{3D}^T\left(2\omega\mathbf{v}_N^{3D} + \omega^2\mathbf{u}_N^{3D}\right), \\
-\mathbf{B}_{3D}^T\dot{\mathbf{v}}_N^{3D} &= \mathbf{B}_{3D}^T\left[2\omega\left(\mathbf{v}_N^{3D} - \dot{\mathbf{d}}^{3D}\right) + \omega^2\left(\mathbf{u}_N^{3D} - \mathbf{d}^{3D}\right)\right] - \ddot{\mathbf{d}}^{3D}, \\
\dot{\mathbf{F}}_1^{3D} &= -\frac{E_1}{c_1}\mathbf{F}_1^{3D} + \left(\lambda_1^{ela}\mathbf{J}_\lambda^{3D} + \mu_1^{ela}\mathbf{J}_\mu^{3D}\right)\dot{\mathbf{u}}_N^{3D}, \\
\dot{\mathbf{F}}_2^{3D} &= -\frac{E_2}{c_2}\mathbf{F}_2^{3D} + \left(\lambda_2^{ela}\mathbf{J}_\lambda^{3D} + \mu_2^{ela}\mathbf{J}_\mu^{3D}\right)\dot{\mathbf{u}}_N^{3D}, \\
\mathbf{F}_3^{3D} &= \left(\lambda_3^{vis}\mathbf{J}_\lambda^{3D} + \mu_3^{vis}\mathbf{J}_\mu^{3D}\right)\mathbf{v}_N^{3D}, \\
\mathbf{F}_{3D}^{rheo} &= \mathbf{F}_1^{3D} + \mathbf{F}_2^{3D} + \mathbf{F}_3^{3D}.
\end{aligned}
\tag{3.38}
$$

Note that the above linear equations are solvable since the coefficient matrix is regular, implying that we can compute $\dot{\mathbf{u}}_N^{3D}$, $\dot{\mathbf{v}}_N^{3D}$, $\dot{\mathbf{F}}_1^{3D}$, and $\dot{\mathbf{F}}_2^{3D}$. Thus, we can obtain the integrals of these variables using the Runge-Kutta method and finally compute 3D rheological deformation and force behaviors. For example, Fig. 3.2 demonstrates simulated behaviors of a 3D cube. The entire top surface of the cube was compressed downward with a constant velocity from time 0 s to 20 s. Before releasing, the deformed object was maintained for 20 seconds. Then, the deformation was partially recovered until time 50 s. The rheological force behavior is also given in Fig. 3.2d. In addition, our FE model is not limited to regular-shaped objects. It can be used to simulate objects with arbitrary shape as long as tetrahedra mesh is available. For example, the deformation of a 3D index finger pushed by an external cube was performed as shown in Fig. 3.3. Both 2D and 3D views are given for the convenience of comparison. The contact modeling used in this example will be discussed in Chapter 4.

The FE models presented so far are based on linear Cauchy strain tensor. Linear FE formulation has an advantage of constant connection matrices $\mathbf{J}_\lambda$ and $\mathbf{J}_\mu$, which can be prepared before performing simulation. This results in more efficient simulation comparing with nonlinear FE formulation. However, linear FE models cannot cover large deformation and cannot simulate deformation with rotation motion, which may frequently happen in many applications, such as surgical simulation and food products manipulation. We will therefore introduce

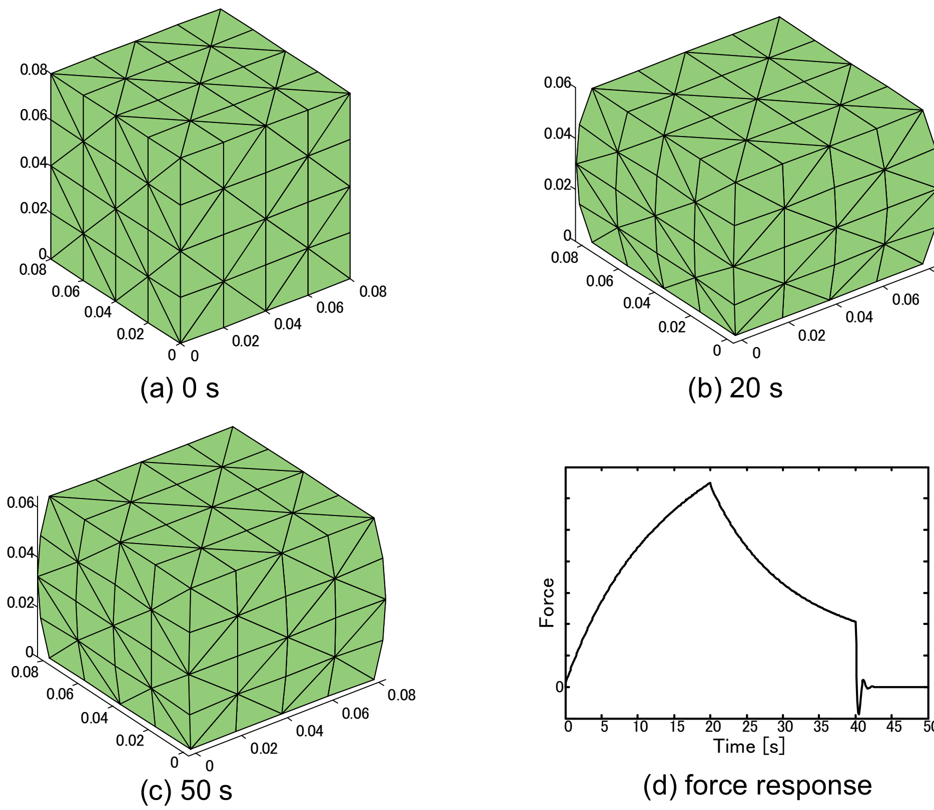

Figure 3.2: Simulation behaviors of a 3D rheological object: initial shape (a), deformed shape (b) at time 20 s, (c) at 50 s, and (d) force response on the bottom surface.

the nonlinear Green strain tensor into our FE model in the next section to deal with this problem.

3.2 FE Formulations with Green Strain Tensor

3.2.1 2D Elastic Model

The Green strain tensor is a nonlinear strain measure which can handle large deformation and rotation. For 2D elastic material, the components of Green

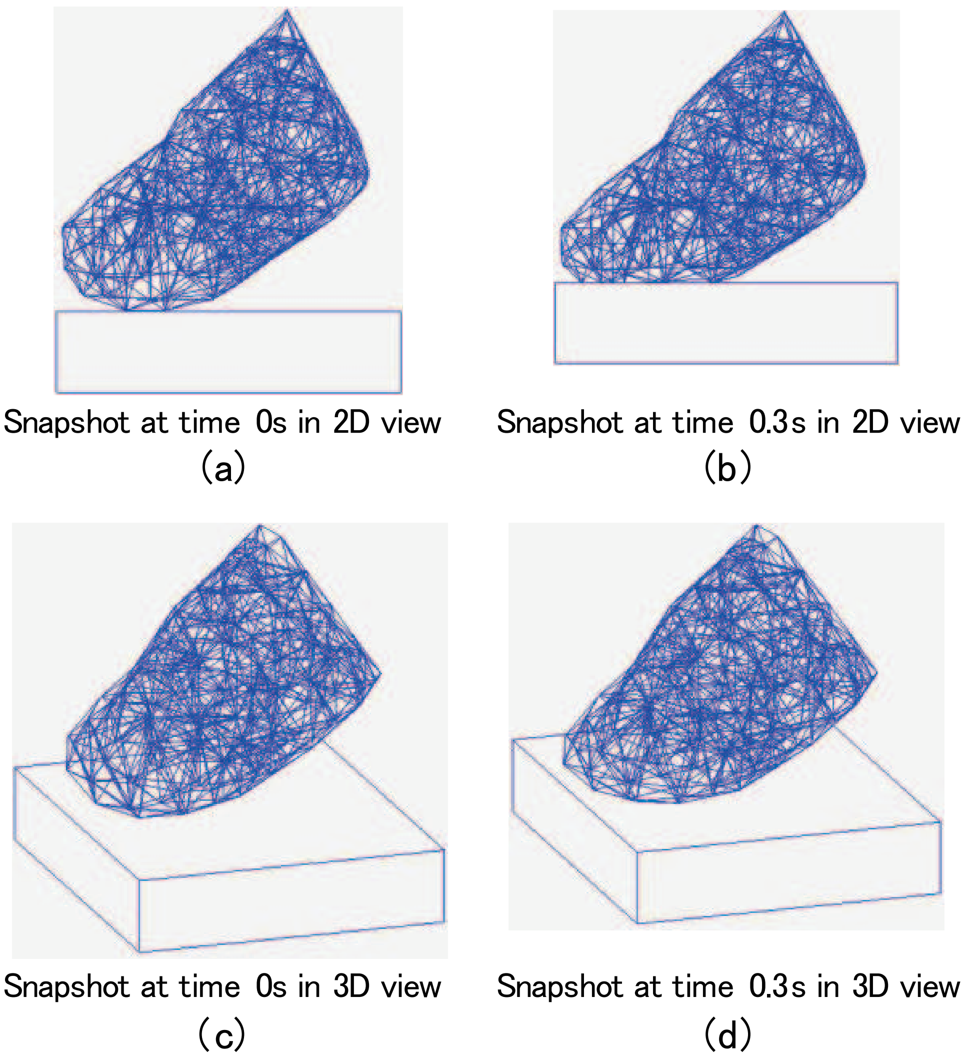

Figure 3.3: Simulation behaviors of a 3D finger pushed by an external cube: (a) initial shape in 2D view, (b) deformed shape at 0.3 s in 2D view, (c) initial shape in 3D view, and (d) deformed shape at 0.3 s in 3D view.

strain tensor ϵ^g are formulated as:

$$\begin{aligned}
\epsilon^g_{xx} &= \frac{\partial u}{\partial x} + \frac{1}{2}\left[\left(\frac{\partial u}{\partial x}\right)^2 + \left(\frac{\partial v}{\partial x}\right)^2\right], \\
\epsilon^g_{yy} &= \frac{\partial v}{\partial y} + \frac{1}{2}\left[\left(\frac{\partial u}{\partial y}\right)^2 + \left(\frac{\partial v}{\partial y}\right)^2\right], \\
2\epsilon^g_{xy} &= \left(\frac{\partial u}{\partial y} + \frac{\partial v}{\partial x}\right) + \left(\frac{\partial u}{\partial x}\frac{\partial u}{\partial y} + \frac{\partial v}{\partial x}\frac{\partial v}{\partial y}\right),
\end{aligned} \tag{3.39}$$

where $u(x, y)$ and $v(x, y)$ denote the displacement of arbitrary point $\mathrm{P}(x, y)$ along x-axis and y-axis respectively. Note that neglecting the quadratic part from the right side of the above equation yields the linear Cauchy strain tensor. Again assuming a 2D object composed of elastic material and constructed by a set of triangles, the strain energy of arbitrary triangle $\triangle \mathrm{P}_i\mathrm{P}_j\mathrm{P}_k$ can be formulated as

$$U_{i,j,k} = \int_{\triangle \mathrm{P}_i\mathrm{P}_j\mathrm{P}_k} \frac{1}{2} \left(\epsilon^g\right)^{\mathrm{T}} \left(\lambda \mathbf{I}_\lambda + \mu \mathbf{I}_\mu\right) \epsilon^g h \, \mathrm{d}S. \tag{3.40}$$

Substituting Eq. 3.4 into the above equation and considering $\epsilon^g = \left[\epsilon^g_{xx}, \epsilon^g_{yy}, 2\epsilon^g_{xy}\right]^{\mathrm{T}}$, we have

$$U_{i,j,k} = U^\lambda_{i,j,k} + U^\mu_{i,j,k}, \tag{3.41}$$

where

$$\begin{aligned} U^\lambda_{i,j,k} &= \int_{\triangle \mathrm{P}_i\mathrm{P}_j\mathrm{P}_k} \frac{1}{2}\lambda \left(\epsilon^g_{xx} + \epsilon^g_{yy}\right)^2 h \, \mathrm{d}S, \\ U^\mu_{i,j,k} &= \int_{\triangle \mathrm{P}_i\mathrm{P}_j\mathrm{P}_k} \frac{1}{2}\mu \left[2\left(\epsilon^g_{xx}\right)^2 + 2\left(\epsilon^g_{yy}\right)^2 + \left(2\epsilon^g_{xy}\right)^2\right] h \, \mathrm{d}S. \end{aligned} \tag{3.42}$$

In the region of $\triangle \mathrm{P}_i\mathrm{P}_j\mathrm{P}_k$, displacement vector $\mathbf{u}_{\mathrm{P}} = [u, v]^{\mathrm{T}}$ at arbitrary point P inside $\triangle \mathrm{P}_i\mathrm{P}_j\mathrm{P}_k$ can be approximated by a linear combination of nodal displacements $\mathbf{u}_i = [u_i, v_i]^{\mathrm{T}}$, $\mathbf{u}_j = [u_j, v_j]^{\mathrm{T}}$, and $\mathbf{u}_k = [u_k, v_k]^{\mathrm{T}}$ as follows:

$$\begin{aligned} u &= u_i N_{i,j,k} + u_j N_{j,k,i} + u_k N_{k,i,j}, \\ v &= v_i N_{i,j,k} + v_j N_{j,k,i} + v_k N_{k,i,j}, \end{aligned} \tag{3.43}$$

where $N_{i,j,k}$, $N_{j,k,i}$, and $N_{k,i,j}$ are the interpolating shape functions. Each of them has a value of 1 at each nodal point P_i, P_j, or P_k, respectively and zeros at all other nodal points. Taking partial derivatives of u and v relative to x and y respectively, we have

$$\begin{aligned} \frac{\partial u}{\partial x} &= u_i \frac{\partial N_{i,j,k}}{\partial x} + u_j \frac{\partial N_{j,k,i}}{\partial x} + u_k \frac{\partial N_{k,i,j}}{\partial x}, \\ \frac{\partial u}{\partial y} &= u_i \frac{\partial N_{i,j,k}}{\partial y} + u_j \frac{\partial N_{j,k,i}}{\partial y} + u_k \frac{\partial N_{k,i,j}}{\partial y}, \\ \frac{\partial v}{\partial x} &= v_i \frac{\partial N_{i,j,k}}{\partial x} + v_j \frac{\partial N_{j,k,i}}{\partial x} + v_k \frac{\partial N_{k,i,j}}{\partial x}, \\ \frac{\partial v}{\partial y} &= v_i \frac{\partial N_{i,j,k}}{\partial y} + v_j \frac{\partial N_{j,k,i}}{\partial y} + v_k \frac{\partial N_{k,i,j}}{\partial y}. \end{aligned} \tag{3.44}$$

Let $[\xi_i,\ \eta_i]^{\mathrm{T}}$, $[\xi_j,\ \eta_j]^{\mathrm{T}}$, and $[\xi_k,\ \eta_k]^{\mathrm{T}}$ be initial coordinates of nodal points P_i, P_j, and P_k, respectively. Partial derivatives of shape functions in Eq. 3.44 can be calculated as:

$$\begin{aligned}
N_{ix} &= \frac{\partial N_{i,j,k}}{\partial x} = \frac{\eta_j - \eta_k}{2\triangle}, \quad N_{iy} = \frac{\partial N_{i,j,k}}{\partial y} = -\frac{\xi_j - \xi_k}{2\triangle}, \\
N_{jx} &= \frac{\partial N_{j,k,i}}{\partial x} = \frac{\eta_k - \eta_i}{2\triangle}, \quad N_{jy} = \frac{\partial N_{j,k,i}}{\partial y} = -\frac{\xi_k - \xi_i}{2\triangle}, \\
N_{kx} &= \frac{\partial N_{k,i,j}}{\partial x} = \frac{\eta_i - \eta_j}{2\triangle}, \quad N_{ky} = \frac{\partial N_{k,i,j}}{\partial y} = -\frac{\xi_i - \xi_j}{2\triangle},
\end{aligned} \tag{3.45}$$

where $\triangle$ denotes the area of triangle $\triangle \mathrm{P}_i\mathrm{P}_j\mathrm{P}_k$. Substituting Eqs. 3.44 and 3.45 into Eq. 3.39, we have

$$\begin{aligned}
\epsilon^g_{xx} &= \alpha^{\mathrm{T}}\mathbf{q}, \\
\epsilon^g_{yy} &= \beta^{\mathrm{T}}\mathbf{q}, \\
2\epsilon^g_{xy} &= \zeta^{\mathrm{T}}\mathbf{q},
\end{aligned} \tag{3.46}$$

where

$$\alpha = \begin{bmatrix} N_{ix} \\ 0 \\ N_{jx} \\ 0 \\ N_{kx} \\ 0 \\ \frac{1}{2}(N_{ix})^2 \\ \frac{1}{2}(N_{ix})^2 \\ \frac{1}{2}(N_{jx})^2 \\ \frac{1}{2}(N_{jx})^2 \\ \frac{1}{2}(N_{kx})^2 \\ \frac{1}{2}(N_{kx})^2 \\ N_{jx}N_{kx} \\ N_{jx}N_{kx} \\ N_{kx}N_{ix} \\ N_{kx}N_{ix} \\ N_{ix}N_{jx} \\ N_{ix}N_{jx} \end{bmatrix}, \beta = \begin{bmatrix} 0 \\ N_{iy} \\ 0 \\ N_{jy} \\ 0 \\ N_{ky} \\ \frac{1}{2}(N_{iy})^2 \\ \frac{1}{2}(N_{iy})^2 \\ \frac{1}{2}(N_{jy})^2 \\ \frac{1}{2}(N_{jy})^2 \\ \frac{1}{2}(N_{ky})^2 \\ \frac{1}{2}(N_{ky})^2 \\ N_{jy}N_{ky} \\ N_{jy}N_{ky} \\ N_{ky}N_{iy} \\ N_{ky}N_{iy} \\ N_{iy}N_{jy} \\ N_{iy}N_{jy} \end{bmatrix}, \zeta = \begin{bmatrix} N_{iy} \\ N_{ix} \\ N_{jy} \\ N_{jx} \\ N_{ky} \\ N_{kx} \\ N_{ix}N_{iy} \\ N_{ix}N_{iy} \\ N_{jx}N_{jy} \\ N_{jx}N_{jy} \\ N_{kx}N_{ky} \\ N_{kx}N_{ky} \\ N_{jx}N_{ky} + N_{kx}N_{jy} \\ N_{jx}N_{ky} + N_{kx}N_{jy} \\ N_{kx}N_{iy} + N_{ix}N_{ky} \\ N_{kx}N_{iy} + N_{ix}N_{ky} \\ N_{ix}N_{jy} + N_{jx}N_{iy} \\ N_{ix}N_{jy} + N_{jx}N_{iy} \end{bmatrix}, \mathbf{q} = \begin{bmatrix} u_i \\ v_i \\ u_j \\ v_j \\ u_k \\ v_k \\ (u_i)^2 \\ (v_i)^2 \\ (u_j)^2 \\ (v_j)^2 \\ (u_k)^2 \\ (v_k)^2 \\ u_j u_k \\ v_j v_k \\ u_k u_i \\ v_k v_i \\ u_i u_j \\ v_i v_j \end{bmatrix}. \tag{3.47}$$

Substituting Eq. 3.46 into Eq. 3.42 and taking the partial derivative of Eq. 3.41 relative to displacement vector $\mathbf{u}_{i,j,k} = [u_i, v_i, u_j, v_j, u_k, v_k]^{\mathrm{T}}$, we have the elastic force formulation with Green strain tensor as:

$$\mathbf{F}^{i,j,k}_{ela(g)} = \mathbf{F}^{i,j,k}_{\lambda(g)} + \mathbf{F}^{i,j,k}_{\mu(g)}, \tag{3.48}$$

where

$$\mathbf{F}^{i,j,k}_{\lambda(g)} = \lambda h \triangle \left(\alpha^{\mathrm{T}}\mathbf{q} + \beta^{\mathrm{T}}\mathbf{q}\right) \begin{bmatrix} \alpha^{\mathrm{T}}\frac{\partial \mathbf{q}}{\partial u_i} + \beta^{\mathrm{T}}\frac{\partial \mathbf{q}}{\partial u_i} \\ \alpha^{\mathrm{T}}\frac{\partial \mathbf{q}}{\partial v_i} + \beta^{\mathrm{T}}\frac{\partial \mathbf{q}}{\partial v_i} \\ \alpha^{\mathrm{T}}\frac{\partial \mathbf{q}}{\partial u_j} + \beta^{\mathrm{T}}\frac{\partial \mathbf{q}}{\partial u_j} \\ \alpha^{\mathrm{T}}\frac{\partial \mathbf{q}}{\partial v_j} + \beta^{\mathrm{T}}\frac{\partial \mathbf{q}}{\partial v_j} \\ \alpha^{\mathrm{T}}\frac{\partial \mathbf{q}}{\partial u_k} + \beta^{\mathrm{T}}\frac{\partial \mathbf{q}}{\partial u_k} \\ \alpha^{\mathrm{T}}\frac{\partial \mathbf{q}}{\partial v_k} + \beta^{\mathrm{T}}\frac{\partial \mathbf{q}}{\partial v_k} \end{bmatrix},$$

$$\mathbf{F}^{i,j,k}_{\mu(g)} = \mu h \triangle \begin{bmatrix} 2\left(\alpha^{\mathrm{T}}\mathbf{q}\right)\left(\alpha^{\mathrm{T}}\frac{\partial \mathbf{q}}{\partial u_i}\right) + 2\left(\beta^{\mathrm{T}}\mathbf{q}\right)\left(\beta^{\mathrm{T}}\frac{\partial \mathbf{q}}{\partial u_i}\right) + \left(\zeta^{\mathrm{T}}\mathbf{q}\right)\left(\zeta^{\mathrm{T}}\frac{\partial \mathbf{q}}{\partial u_i}\right) \\ 2\left(\alpha^{\mathrm{T}}\mathbf{q}\right)\left(\alpha^{\mathrm{T}}\frac{\partial \mathbf{q}}{\partial v_i}\right) + 2\left(\beta^{\mathrm{T}}\mathbf{q}\right)\left(\beta^{\mathrm{T}}\frac{\partial \mathbf{q}}{\partial v_i}\right) + \left(\zeta^{\mathrm{T}}\mathbf{q}\right)\left(\zeta^{\mathrm{T}}\frac{\partial \mathbf{q}}{\partial v_i}\right) \\ 2\left(\alpha^{\mathrm{T}}\mathbf{q}\right)\left(\alpha^{\mathrm{T}}\frac{\partial \mathbf{q}}{\partial u_j}\right) + 2\left(\beta^{\mathrm{T}}\mathbf{q}\right)\left(\beta^{\mathrm{T}}\frac{\partial \mathbf{q}}{\partial u_j}\right) + \left(\zeta^{\mathrm{T}}\mathbf{q}\right)\left(\zeta^{\mathrm{T}}\frac{\partial \mathbf{q}}{\partial u_j}\right) \\ 2\left(\alpha^{\mathrm{T}}\mathbf{q}\right)\left(\alpha^{\mathrm{T}}\frac{\partial \mathbf{q}}{\partial v_j}\right) + 2\left(\beta^{\mathrm{T}}\mathbf{q}\right)\left(\beta^{\mathrm{T}}\frac{\partial \mathbf{q}}{\partial v_j}\right) + \left(\zeta^{\mathrm{T}}\mathbf{q}\right)\left(\zeta^{\mathrm{T}}\frac{\partial \mathbf{q}}{\partial v_j}\right) \\ 2\left(\alpha^{\mathrm{T}}\mathbf{q}\right)\left(\alpha^{\mathrm{T}}\frac{\partial \mathbf{q}}{\partial u_k}\right) + 2\left(\beta^{\mathrm{T}}\mathbf{q}\right)\left(\beta^{\mathrm{T}}\frac{\partial \mathbf{q}}{\partial u_k}\right) + \left(\zeta^{\mathrm{T}}\mathbf{q}\right)\left(\zeta^{\mathrm{T}}\frac{\partial \mathbf{q}}{\partial u_k}\right) \\ 2\left(\alpha^{\mathrm{T}}\mathbf{q}\right)\left(\alpha^{\mathrm{T}}\frac{\partial \mathbf{q}}{\partial v_k}\right) + 2\left(\beta^{\mathrm{T}}\mathbf{q}\right)\left(\beta^{\mathrm{T}}\frac{\partial \mathbf{q}}{\partial v_k}\right) + \left(\zeta^{\mathrm{T}}\mathbf{q}\right)\left(\zeta^{\mathrm{T}}\frac{\partial \mathbf{q}}{\partial v_k}\right) \end{bmatrix}. \tag{3.49}$$

Substituting vectors α, β, ζ, and $\mathbf{q}$ of Eq. 3.47 into the above equation and performing a series of transformations, we can end up with a formulation of elastic forces with green strain as follows, which has a similar form with Eq. 3.16:

$$\mathbf{F}^{i,j,k}_{ela(g)} = \left(\lambda \mathbf{J}^{i,j,k}_{\lambda(g)} + \mu \mathbf{J}^{i,j,k}_{\mu(g)}\right) \mathbf{u}_{i,j,k}, \tag{3.50}$$

where

$$\begin{aligned} \mathbf{J}^{i,j,k}_{\lambda(g)} &= \mathbf{J}^{cons}_{\lambda} + \mathbf{J}^{var1}_{\lambda} + \mathbf{J}^{var2}_{\lambda}, \\ \mathbf{J}^{i,j,k}_{\mu(g)} &= \mathbf{J}^{cons}_{\mu} + \mathbf{J}^{var1}_{\mu} + \mathbf{J}^{var2}_{\mu}, \end{aligned} \tag{3.51}$$

with constant matrices $\mathbf{J}_\lambda^{cons}$ and $\mathbf{J}_\mu^{cons}$ given by:

$$
\mathbf{J}_\lambda^{cons} = h\triangle \begin{bmatrix}
N_{ix}^2 & N_{ix}N_{iy} & N_{ix}N_{jx} & N_{ix}N_{jy} & N_{ix}N_{kx} & N_{ix}N_{ky} \\
N_{iy}N_{ix} & N_{iy}^2 & N_{iy}N_{jx} & N_{iy}N_{jy} & N_{iy}N_{kx} & N_{iy}N_{ky} \\
N_{jx}N_{ix} & N_{jx}N_{iy} & N_{jx}^2 & N_{jx}N_{jy} & N_{jx}N_{kx} & N_{jx}N_{ky} \\
N_{jy}N_{ix} & N_{jy}N_{iy} & N_{jy}N_{jx} & N_{jy}^2 & N_{jy}N_{kx} & N_{jy}N_{ky} \\
N_{kx}N_{ix} & N_{kx}N_{iy} & N_{kx}N_{jx} & N_{kx}N_{jy} & N_{kx}^2 & N_{kx}N_{ky} \\
N_{ky}N_{ix} & N_{ky}N_{iy} & N_{ky}N_{jx} & N_{ky}N_{jy} & N_{ky}N_{kx} & N_{ky}^2
\end{bmatrix},
$$

$$
\mathbf{J}_\mu^{cons} = h\triangle \left[\begin{matrix}
2N_{ix}^2 + N_{iy}^2 & N_{iy}N_{ix} & 2N_{ix}N_{jx} + N_{iy}N_{jy} \\
N_{ix}N_{iy} & 2N_{iy}^2 + N_{ix}^2 & N_{ix}N_{jy} \\
2N_{jx}N_{ix} + N_{jy}N_{iy} & N_{jy}N_{ix} & 2N_{jx}^2 + N_{jy}^2 \\
N_{jx}N_{iy} & 2N_{jy}N_{iy} + N_{jx}N_{ix} & N_{jx}N_{jy} \\
2N_{kx}N_{ix} + N_{ky}N_{iy} & N_{ky}N_{ix} & 2N_{kx}N_{jx} + N_{ky}N_{jy} \\
N_{kx}N_{iy} & 2N_{ky}N_{iy} + N_{kx}N_{ix} & N_{kx}N_{jy}
\end{matrix}\right.
$$

$$
\left.\begin{matrix}
N_{iy}N_{jx} & 2N_{ix}N_{kx} + N_{iy}N_{ky} & N_{iy}N_{kx} \\
2N_{iy}N_{jy} + N_{ix}N_{jx} & N_{ix}N_{ky} & 2N_{iy}N_{ky} + N_{ix}N_{kx} \\
N_{jy}N_{jx} & 2N_{jx}N_{kx} + N_{jy}N_{ky} & N_{jy}N_{kx} \\
2N_{jy}^2 + N_{jx}^2 & N_{jx}N_{ky} & 2N_{jy}N_{ky} + N_{jx}N_{kx} \\
N_{ky}N_{jx} & 2N_{kx}^2 + N_{ky}^2 & N_{ky}N_{kx} \\
2N_{ky}N_{jy} + N_{kx}N_{jx} & N_{kx}N_{ky} & 2N_{ky}^2 + N_{kx}^2
\end{matrix}\right]. \tag{3.52}
$$

Time-varying matrices $\mathbf{J}_\lambda^{var1}$ and $\mathbf{J}_\mu^{var1}$ have the following symmetrical forms:

$$\mathbf{J}_\lambda^{var1} = h\triangle\left(\alpha^{\mathrm{T}}\mathbf{q} + \beta^{\mathrm{T}}\mathbf{q}\right) \left[\begin{matrix} N_{ix}^2 + N_{iy}^2 & 0 & 2N_{ix}N_{jx} + N_{iy}N_{jy} \\ 0 & N_{iy}^2 + N_{ix}^2 & 0 \\ N_{jx}N_{ix} + N_{jy}N_{iy} & 0 & N_{jx}^2 + N_{jy}^2 \\ 0 & N_{jy}N_{iy} + N_{jx}N_{ix} & 0 \\ N_{kx}N_{ix} + N_{ky}N_{iy} & 0 & N_{kx}N_{jx} + N_{ky}N_{jy} \\ 0 & N_{ky}N_{iy} + N_{kx}N_{ix} & 0 \end{matrix}\right.$$

$$\left.\begin{matrix} 0 & N_{ix}N_{kx} + N_{iy}N_{ky} & 0 \\ N_{iy}N_{jy} + N_{ix}N_{jx} & 0 & N_{iy}N_{ky} + N_{ix}N_{kx} \\ 0 & N_{jx}N_{kx} + N_{jy}N_{ky} & 0 \\ N_{jy}^2 + N_{jx}^2 & 0 & N_{jy}N_{ky} + N_{jx}N_{kx} \\ 0 & N_{kx}^2 + N_{ky}^2 & 0 \\ N_{ky}N_{jy} + N_{kx}N_{jx} & 0 & N_{ky}^2 + N_{kx}^2 \end{matrix}\right].$$

$$\mathbf{J}_\mu^{var1} = 2h\triangle\left(\alpha^{\mathrm{T}}\mathbf{q}\right) \begin{bmatrix} N_{ix}^2 & 0 & N_{ix}N_{jx} & 0 & N_{ix}N_{kx} & 0 \\ 0 & N_{ix}^2 & 0 & N_{ix}N_{jx} & 0 & N_{ix}N_{kx} \\ N_{jx}N_{ix} & 0 & N_{jx}^2 & 0 & N_{jx}N_{kx} & 0 \\ 0 & N_{jx}N_{ix} & 0 & N_{jx}^2 & 0 & N_{jx}N_{kx} \\ N_{kx}N_{ix} & 0 & N_{kx}N_{jx} & 0 & N_{kx}^2 & 0 \\ 0 & N_{kx}N_{ix} & 0 & N_{kx}N_{jx} & 0 & N_{kx}^2 \end{bmatrix}$$

$$+ 2h\triangle\left(\beta^{\mathrm{T}}\mathbf{q}\right) \begin{bmatrix} N_{iy}^2 & 0 & N_{iy}N_{jy} & 0 & N_{iy}N_{ky} & 0 \\ 0 & N_{iy}^2 & 0 & N_{iy}N_{jy} & 0 & N_{iy}N_{ky} \\ N_{jy}N_{iy} & 0 & N_{jy}^2 & 0 & N_{jy}N_{ky} & 0 \\ 0 & N_{jy}N_{iy} & 0 & N_{jy}^2 & 0 & N_{jy}N_{ky} \\ N_{ky}N_{iy} & 0 & N_{ky}N_{jy} & 0 & N_{ky}^2 & 0 \\ 0 & N_{ky}N_{iy} & 0 & N_{ky}N_{jy} & 0 & N_{ky}^2 \end{bmatrix}$$

$$+ h\triangle\left(\gamma^{\mathrm{T}}\mathbf{q}\right) \left[\begin{matrix} 2N_{ix}N_{iy} & 0 & N_{ix}N_{jy} + N_{jx}N_{iy} \\ 0 & 2N_{ix}N_{iy} & 0 \\ N_{jx}N_{iy} + N_{ix}N_{jy} & 0 & 2N_{jx}N_{jy} \\ 0 & N_{jx}N_{iy} + N_{ix}N_{jy} & 0 \\ N_{kx}N_{iy} + N_{ix}N_{ky} & 0 & N_{kx}N_{jy} + N_{jx}N_{ky} \\ 0 & N_{kx}N_{iy} + N_{ix}N_{ky} & 0 \end{matrix}\right.$$

$$\left.\begin{matrix} 0 & N_{ix}N_{ky} + N_{kx}N_{iy} & 0 \\ N_{ix}N_{jy} + N_{jx}N_{iy} & 0 & N_{ix}N_{ky} + N_{kx}N_{iy} \\ 0 & N_{jx}N_{ky} + N_{kx}N_{jy} & 0 \\ 2N_{jy}N_{jx} & 0 & N_{jx}N_{ky} + N_{kx}N_{jy} \\ 0 & 2N_{kx}N_{ky} & 0 \\ N_{kx}N_{jy} + N_{jx}N_{ky} & 0 & 2N_{kx}N_{ky} \end{matrix}\right]. \tag{3.53}$$

Time-varying matrices $\mathbf{J}_{\lambda}^{var2}$ and $\mathbf{J}_{\mu}^{var2}$ have the following unsymmetrical forms:

$$\mathbf{J}_{\lambda}^{var2} = \frac{h\triangle}{2}\left[\begin{array}{cccccc}
N_{ix}(\mathbf{H}_1^{\alpha}+\mathbf{H}_1^{\beta})^{\mathrm{T}}\mathbf{u}_{i,j,k} & N_{ix}(\mathbf{H}_2^{\alpha}+\mathbf{H}_2^{\beta})^{\mathrm{T}}\mathbf{u}_{i,j,k} & N_{ix}(\mathbf{H}_3^{\alpha}+\mathbf{H}_3^{\beta})^{\mathrm{T}}\mathbf{u}_{i,j,k} & N_{ix}(\mathbf{H}_4^{\alpha}+\mathbf{H}_4^{\beta})^{\mathrm{T}}\mathbf{u}_{i,j,k} & N_{ix}(\mathbf{H}_5^{\alpha}+\mathbf{H}_5^{\beta})^{\mathrm{T}}\mathbf{u}_{i,j,k} & N_{ix}(\mathbf{H}_6^{\alpha}+\mathbf{H}_6^{\beta})^{\mathrm{T}}\mathbf{u}_{i,j,k} \\
N_{iy}(\mathbf{H}_1^{\alpha}+\mathbf{H}_1^{\beta})^{\mathrm{T}}\mathbf{u}_{i,j,k} & N_{iy}(\mathbf{H}_2^{\alpha}+\mathbf{H}_2^{\beta})^{\mathrm{T}}\mathbf{u}_{i,j,k} & N_{iy}(\mathbf{H}_3^{\alpha}+\mathbf{H}_3^{\beta})^{\mathrm{T}}\mathbf{u}_{i,j,k} & N_{iy}(\mathbf{H}_4^{\alpha}+\mathbf{H}_4^{\beta})^{\mathrm{T}}\mathbf{u}_{i,j,k} & N_{iy}(\mathbf{H}_5^{\alpha}+\mathbf{H}_5^{\beta})^{\mathrm{T}}\mathbf{u}_{i,j,k} & N_{iy}(\mathbf{H}_6^{\alpha}+\mathbf{H}_6^{\beta})^{\mathrm{T}}\mathbf{u}_{i,j,k} \\
N_{jx}(\mathbf{H}_1^{\alpha}+\mathbf{H}_1^{\beta})^{\mathrm{T}}\mathbf{u}_{i,j,k} & N_{jx}(\mathbf{H}_2^{\alpha}+\mathbf{H}_2^{\beta})^{\mathrm{T}}\mathbf{u}_{i,j,k} & N_{jx}(\mathbf{H}_3^{\alpha}+\mathbf{H}_3^{\beta})^{\mathrm{T}}\mathbf{u}_{i,j,k} & N_{jx}(\mathbf{H}_4^{\alpha}+\mathbf{H}_4^{\beta})^{\mathrm{T}}\mathbf{u}_{i,j,k} & N_{jx}(\mathbf{H}_5^{\alpha}+\mathbf{H}_5^{\beta})^{\mathrm{T}}\mathbf{u}_{i,j,k} & N_{jx}(\mathbf{H}_6^{\alpha}+\mathbf{H}_6^{\beta})^{\mathrm{T}}\mathbf{u}_{i,j,k} \\
N_{jy}(\mathbf{H}_1^{\alpha}+\mathbf{H}_1^{\beta})^{\mathrm{T}}\mathbf{u}_{i,j,k} & N_{jy}(\mathbf{H}_2^{\alpha}+\mathbf{H}_2^{\beta})^{\mathrm{T}}\mathbf{u}_{i,j,k} & N_{jy}(\mathbf{H}_3^{\alpha}+\mathbf{H}_3^{\beta})^{\mathrm{T}}\mathbf{u}_{i,j,k} & N_{jy}(\mathbf{H}_4^{\alpha}+\mathbf{H}_4^{\beta})^{\mathrm{T}}\mathbf{u}_{i,j,k} & N_{jy}(\mathbf{H}_5^{\alpha}+\mathbf{H}_5^{\beta})^{\mathrm{T}}\mathbf{u}_{i,j,k} & N_{jy}(\mathbf{H}_6^{\alpha}+\mathbf{H}_6^{\beta})^{\mathrm{T}}\mathbf{u}_{i,j,k} \\
N_{kx}(\mathbf{H}_1^{\alpha}+\mathbf{H}_1^{\beta})^{\mathrm{T}}\mathbf{u}_{i,j,k} & N_{kx}(\mathbf{H}_2^{\alpha}+\mathbf{H}_2^{\beta})^{\mathrm{T}}\mathbf{u}_{i,j,k} & N_{kx}(\mathbf{H}_3^{\alpha}+\mathbf{H}_3^{\beta})^{\mathrm{T}}\mathbf{u}_{i,j,k} & N_{kx}(\mathbf{H}_4^{\alpha}+\mathbf{H}_4^{\beta})^{\mathrm{T}}\mathbf{u}_{i,j,k} & N_{kx}(\mathbf{H}_5^{\alpha}+\mathbf{H}_5^{\beta})^{\mathrm{T}}\mathbf{u}_{i,j,k} & N_{kx}(\mathbf{H}_6^{\alpha}+\mathbf{H}_6^{\beta})^{\mathrm{T}}\mathbf{u}_{i,j,k} \\
N_{ky}(\mathbf{H}_1^{\alpha}+\mathbf{H}_1^{\beta})^{\mathrm{T}}\mathbf{u}_{i,j,k} & N_{ky}(\mathbf{H}_2^{\alpha}+\mathbf{H}_2^{\beta})^{\mathrm{T}}\mathbf{u}_{i,j,k} & N_{ky}(\mathbf{H}_3^{\alpha}+\mathbf{H}_3^{\beta})^{\mathrm{T}}\mathbf{u}_{i,j,k} & N_{ky}(\mathbf{H}_4^{\alpha}+\mathbf{H}_4^{\beta})^{\mathrm{T}}\mathbf{u}_{i,j,k} & N_{ky}(\mathbf{H}_5^{\alpha}+\mathbf{H}_5^{\beta})^{\mathrm{T}}\mathbf{u}_{i,j,k} & N_{ky}(\mathbf{H}_6^{\alpha}+\mathbf{H}_6^{\beta})^{\mathrm{T}}\mathbf{u}_{i,j,k}
\end{array}\right],$$

$$\mathbf{J}_{\mu}^{var2} = \frac{h\triangle}{2}\left[\begin{array}{cccccc}
2N_{ix}(\mathbf{H}_1^{\alpha})^{\mathrm{T}}\mathbf{u}_{i,j,k}+N_{iy}(\mathbf{H}_1^{\zeta})^{\mathrm{T}}\mathbf{u}_{i,j,k} & 2N_{ix}(\mathbf{H}_2^{\alpha})^{\mathrm{T}}\mathbf{u}_{i,j,k}+N_{iy}(\mathbf{H}_2^{\zeta})^{\mathrm{T}}\mathbf{u}_{i,j,k} & 2N_{ix}(\mathbf{H}_3^{\alpha})^{\mathrm{T}}\mathbf{u}_{i,j,k}+N_{iy}(\mathbf{H}_3^{\zeta})^{\mathrm{T}}\mathbf{u}_{i,j,k} & 2N_{ix}(\mathbf{H}_4^{\alpha})^{\mathrm{T}}\mathbf{u}_{i,j,k}+N_{iy}(\mathbf{H}_4^{\zeta})^{\mathrm{T}}\mathbf{u}_{i,j,k} & 2N_{ix}(\mathbf{H}_5^{\alpha})^{\mathrm{T}}\mathbf{u}_{i,j,k}+N_{iy}(\mathbf{H}_5^{\zeta})^{\mathrm{T}}\mathbf{u}_{i,j,k} & 2N_{ix}(\mathbf{H}_6^{\alpha})^{\mathrm{T}}\mathbf{u}_{i,j,k}+N_{iy}(\mathbf{H}_6^{\zeta})^{\mathrm{T}}\mathbf{u}_{i,j,k} \\
2N_{iy}(\mathbf{H}_1^{\beta})^{\mathrm{T}}\mathbf{u}_{i,j,k}+N_{ix}(\mathbf{H}_1^{\zeta})^{\mathrm{T}}\mathbf{u}_{i,j,k} & 2N_{iy}(\mathbf{H}_2^{\beta})^{\mathrm{T}}\mathbf{u}_{i,j,k}+N_{ix}(\mathbf{H}_2^{\zeta})^{\mathrm{T}}\mathbf{u}_{i,j,k} & 2N_{iy}(\mathbf{H}_3^{\beta})^{\mathrm{T}}\mathbf{u}_{i,j,k}+N_{ix}(\mathbf{H}_3^{\zeta})^{\mathrm{T}}\mathbf{u}_{i,j,k} & 2N_{iy}(\mathbf{H}_4^{\beta})^{\mathrm{T}}\mathbf{u}_{i,j,k}+N_{ix}(\mathbf{H}_4^{\zeta})^{\mathrm{T}}\mathbf{u}_{i,j,k} & 2N_{iy}(\mathbf{H}_5^{\beta})^{\mathrm{T}}\mathbf{u}_{i,j,k}+N_{ix}(\mathbf{H}_5^{\zeta})^{\mathrm{T}}\mathbf{u}_{i,j,k} & 2N_{iy}(\mathbf{H}_6^{\beta})^{\mathrm{T}}\mathbf{u}_{i,j,k}+N_{ix}(\mathbf{H}_6^{\zeta})^{\mathrm{T}}\mathbf{u}_{i,j,k} \\
2N_{jx}(\mathbf{H}_1^{\alpha})^{\mathrm{T}}\mathbf{u}_{i,j,k}+N_{jy}(\mathbf{H}_1^{\zeta})^{\mathrm{T}}\mathbf{u}_{i,j,k} & 2N_{jx}(\mathbf{H}_2^{\alpha})^{\mathrm{T}}\mathbf{u}_{i,j,k}+N_{jy}(\mathbf{H}_2^{\zeta})^{\mathrm{T}}\mathbf{u}_{i,j,k} & 2N_{jx}(\mathbf{H}_3^{\alpha})^{\mathrm{T}}\mathbf{u}_{i,j,k}+N_{jy}(\mathbf{H}_3^{\zeta})^{\mathrm{T}}\mathbf{u}_{i,j,k} & 2N_{jx}(\mathbf{H}_4^{\alpha})^{\mathrm{T}}\mathbf{u}_{i,j,k}+N_{jy}(\mathbf{H}_4^{\zeta})^{\mathrm{T}}\mathbf{u}_{i,j,k} & 2N_{jx}(\mathbf{H}_5^{\alpha})^{\mathrm{T}}\mathbf{u}_{i,j,k}+N_{jy}(\mathbf{H}_5^{\zeta})^{\mathrm{T}}\mathbf{u}_{i,j,k} & 2N_{jx}(\mathbf{H}_6^{\alpha})^{\mathrm{T}}\mathbf{u}_{i,j,k}+N_{jy}(\mathbf{H}_6^{\zeta})^{\mathrm{T}}\mathbf{u}_{i,j,k} \\
2N_{jy}(\mathbf{H}_1^{\beta})^{\mathrm{T}}\mathbf{u}_{i,j,k}+N_{jx}(\mathbf{H}_1^{\zeta})^{\mathrm{T}}\mathbf{u}_{i,j,k} & 2N_{jy}(\mathbf{H}_2^{\beta})^{\mathrm{T}}\mathbf{u}_{i,j,k}+N_{jx}(\mathbf{H}_2^{\zeta})^{\mathrm{T}}\mathbf{u}_{i,j,k} & 2N_{jy}(\mathbf{H}_3^{\beta})^{\mathrm{T}}\mathbf{u}_{i,j,k}+N_{jx}(\mathbf{H}_3^{\zeta})^{\mathrm{T}}\mathbf{u}_{i,j,k} & 2N_{jy}(\mathbf{H}_4^{\beta})^{\mathrm{T}}\mathbf{u}_{i,j,k}+N_{jx}(\mathbf{H}_4^{\zeta})^{\mathrm{T}}\mathbf{u}_{i,j,k} & 2N_{jy}(\mathbf{H}_5^{\beta})^{\mathrm{T}}\mathbf{u}_{i,j,k}+N_{jx}(\mathbf{H}_5^{\zeta})^{\mathrm{T}}\mathbf{u}_{i,j,k} & 2N_{jy}(\mathbf{H}_6^{\beta})^{\mathrm{T}}\mathbf{u}_{i,j,k}+N_{jx}(\mathbf{H}_6^{\zeta})^{\mathrm{T}}\mathbf{u}_{i,j,k} \\
2N_{kx}(\mathbf{H}_1^{\alpha})^{\mathrm{T}}\mathbf{u}_{i,j,k}+N_{ky}(\mathbf{H}_1^{\zeta})^{\mathrm{T}}\mathbf{u}_{i,j,k} & 2N_{kx}(\mathbf{H}_2^{\alpha})^{\mathrm{T}}\mathbf{u}_{i,j,k}+N_{ky}(\mathbf{H}_2^{\zeta})^{\mathrm{T}}\mathbf{u}_{i,j,k} & 2N_{kx}(\mathbf{H}_3^{\alpha})^{\mathrm{T}}\mathbf{u}_{i,j,k}+N_{ky}(\mathbf{H}_3^{\zeta})^{\mathrm{T}}\mathbf{u}_{i,j,k} & 2N_{kx}(\mathbf{H}_4^{\alpha})^{\mathrm{T}}\mathbf{u}_{i,j,k}+N_{ky}(\mathbf{H}_4^{\zeta})^{\mathrm{T}}\mathbf{u}_{i,j,k} & 2N_{kx}(\mathbf{H}_5^{\alpha})^{\mathrm{T}}\mathbf{u}_{i,j,k}+N_{ky}(\mathbf{H}_5^{\zeta})^{\mathrm{T}}\mathbf{u}_{i,j,k} & 2N_{kx}(\mathbf{H}_6^{\alpha})^{\mathrm{T}}\mathbf{u}_{i,j,k}+N_{ky}(\mathbf{H}_6^{\zeta})^{\mathrm{T}}\mathbf{u}_{i,j,k} \\
2N_{ky}(\mathbf{H}_1^{\beta})^{\mathrm{T}}\mathbf{u}_{i,j,k}+N_{kx}(\mathbf{H}_1^{\zeta})^{\mathrm{T}}\mathbf{u}_{i,j,k} & 2N_{ky}(\mathbf{H}_2^{\beta})^{\mathrm{T}}\mathbf{u}_{i,j,k}+N_{kx}(\mathbf{H}_2^{\zeta})^{\mathrm{T}}\mathbf{u}_{i,j,k} & 2N_{ky}(\mathbf{H}_3^{\beta})^{\mathrm{T}}\mathbf{u}_{i,j,k}+N_{kx}(\mathbf{H}_3^{\zeta})^{\mathrm{T}}\mathbf{u}_{i,j,k} & 2N_{ky}(\mathbf{H}_4^{\beta})^{\mathrm{T}}\mathbf{u}_{i,j,k}+N_{kx}(\mathbf{H}_4^{\zeta})^{\mathrm{T}}\mathbf{u}_{i,j,k} & 2N_{ky}(\mathbf{H}_5^{\beta})^{\mathrm{T}}\mathbf{u}_{i,j,k}+N_{kx}(\mathbf{H}_5^{\zeta})^{\mathrm{T}}\mathbf{u}_{i,j,k} & 2N_{ky}(\mathbf{H}_6^{\beta})^{\mathrm{T}}\mathbf{u}_{i,j,k}+N_{kx}(\mathbf{H}_6^{\zeta})^{\mathrm{T}}\mathbf{u}_{i,j,k}
\end{array}\right], \tag{3.54}$$

where

$$\mathbf{H}_1^\alpha = \begin{bmatrix} N_{ix}^2 \\ 0 \\ N_{ix}N_{jx} \\ 0 \\ N_{ix}N_{kx} \\ 0 \end{bmatrix}, \quad \mathbf{H}_2^\alpha = \begin{bmatrix} 0 \\ N_{ix}^2 \\ 0 \\ N_{ix}N_{jx} \\ 0 \\ N_{ix}N_{kx} \end{bmatrix}, \quad \mathbf{H}_3^\alpha = \begin{bmatrix} N_{jx}N_{ix} \\ 0 \\ N_{jx}^2 \\ 0 \\ N_{jx}N_{kx} \\ 0 \end{bmatrix},$$

$$\mathbf{H}_4^\alpha = \begin{bmatrix} 0 \\ N_{jx}N_{ix} \\ 0 \\ Njx^2 \\ 0 \\ N_{jx}N_{kx} \end{bmatrix}, \quad \mathbf{H}_5^\alpha = \begin{bmatrix} N_{kx}N_{ix} \\ 0 \\ N_{kx}N_{jx} \\ 0 \\ N_{kx}^2 \\ 0 \end{bmatrix}, \quad \mathbf{H}_6^\alpha = \begin{bmatrix} 0 \\ N_{kx}N_{ix} \\ 0 \\ N_{kx}N_{jx} \\ 0 \\ N_{kx}^2 \end{bmatrix},$$

$$\mathbf{H}_1^\beta = \begin{bmatrix} N_{iy}^2 \\ 0 \\ N_{iy}N_{jy} \\ 0 \\ N_{iy}N_{ky} \\ 0 \end{bmatrix}, \quad \mathbf{H}_2^\beta = \begin{bmatrix} 0 \\ N_{iy}^2 \\ 0 \\ N_{iy}N_{jy} \\ 0 \\ N_{iy}N_{ky} \end{bmatrix}, \quad \mathbf{H}_3^\beta = \begin{bmatrix} N_{jy}N_{iy} \\ 0 \\ N_{jy}^2 \\ 0 \\ N_{jy}N_{ky} \\ 0 \end{bmatrix},$$

$$\mathbf{H}_4^\beta = \begin{bmatrix} 0 \\ N_{jy}N_{iy} \\ 0 \\ Njy^2 \\ 0 \\ N_{jy}N_{ky} \end{bmatrix}, \quad \mathbf{H}_5^\beta = \begin{bmatrix} N_{ky}N_{iy} \\ 0 \\ N_{ky}N_{jy} \\ 0 \\ N_{ky}^2 \\ 0 \end{bmatrix}, \quad \mathbf{H}_6^\beta = \begin{bmatrix} 0 \\ N_{ky}N_{iy} \\ 0 \\ N_{ky}N_{jy} \\ 0 \\ N_{ky}^2 \end{bmatrix},$$

$$\mathbf{H}_1^\zeta = \begin{bmatrix} 2N_{ix}N_{iy} \\ 0 \\ N_{ix}N_{jy}+N_{jx}N_{iy} \\ 0 \\ N_{ix}N_{ky}+N_{kx}N_{iy} \\ 0 \end{bmatrix}, \ \mathbf{H}_2^\zeta = \begin{bmatrix} 0 \\ 2N_{ix}N_{iy} \\ 0 \\ N_{ix}N_{jy}+N_{jx}N_{iy} \\ 0 \\ N_{ix}N_{ky}+N_{kx}N_{iy} \end{bmatrix}, \ \mathbf{H}_3^\zeta = \begin{bmatrix} N_{ix}N_{jy}+N_{jx}N_{iy} \\ 0 \\ 2N_{jx}N_{jy} \\ 0 \\ N_{jx}N_{ky}+N_{kx}N_{jy} \\ 0 \end{bmatrix},$$

$$\mathbf{H}_4^\zeta = \begin{bmatrix} 0 \\ N_{ix}N_{jy}+N_{jx}N_{iy} \\ 0 \\ 2N_{jx}N_{jy} \\ 0 \\ N_{jx}N_{ky}+N_{kx}N_{jy} \end{bmatrix}, \ \mathbf{H}_5^\zeta = \begin{bmatrix} N_{ix}N_{ky}+N_{kx}N_{iy} \\ 0 \\ N_{jx}N_{ky}+N_{kx}N_{jy} \\ 0 \\ 2N_{kx}N_{ky} \\ 0 \end{bmatrix}, \ \mathbf{H}_6^\zeta = \begin{bmatrix} 0 \\ N_{ix}N_{ky}+N_{kx}N_{iy} \\ 0 \\ N_{jx}N_{ky}+N_{kx}N_{jy} \\ 02N_{kx}N_{ky} \end{bmatrix}. \tag{3.55}$$

From the above derivations we found that the connection matrices $\mathbf{J}_{\lambda(g)}^{i,j,k}$ and

$\mathbf{J}_{\mu(g)}^{i,j,k}$ are no longer constant and depend on the time-varying displacement vector $\mathbf{u}_{i,j,k}$. We were not able to prepare those two matrices before simulation and we have to calculate them at every time step.

3.2.2 2D Rheological Model

Following the same replacement procedure presented in Section 3.1, we can extend the above elastic model to a rheological model. Performing a series of replacements to Eq. 3.25, we have

$$\begin{aligned}
&\dot{\mathbf{F}}_1^g + \frac{E_1}{c_1}\mathbf{F}_1^g = (\lambda_1^{ela}\mathbf{J}_\lambda^g + \mu_1^{ela}\mathbf{J}_\mu^g)\dot{\mathbf{u}}_N, \\
&\dot{\mathbf{F}}_2^g + \frac{E_2}{c_2}\mathbf{F}_2^g = (\lambda_2^{ela}\mathbf{J}_\lambda^g + \mu_2^{ela}\mathbf{J}_\mu^g)\dot{\mathbf{u}}_N, \\
&\mathbf{F}_3^g = (\lambda_3^{vis}\mathbf{J}_\lambda^g + \mu_3^{vis}\mathbf{J}_\mu^g)\dot{\mathbf{u}}_N, \\
&\mathbf{F}_{2D(g)}^{rheo} = \mathbf{F}_1^g + \mathbf{F}_2^g + \mathbf{F}_3^g,
\end{aligned} \tag{3.56}$$

where superscript g denotes the variables with a formulation of Green strain tensor. Total connection matrices $\mathbf{J}_\lambda^g$ and $\mathbf{J}_\mu^g$ were calculated by incorporating the matrices $\mathbf{J}_{\lambda(g)}^{i,j,k}$ and $\mathbf{J}_{\mu(g)}^{i,j,k}$ of each triangles based on the contribution of each triangle to the whole triangle mesh. Vector $\mathbf{F}_{2D(g)}^{rheo}$ is the rheological forces generated on each nodal point.

For performing an operation on a virtual object, boundary constraints need to be formulated. For example, we suppose a 2D object was fixed on the ground and the top edge or some nodal points were pushed down or pulled up with a displacement function of $\mathbf{d}(t)$. Two boundary constraints on both top and bottom edges can be formulated as given in Eq. 3.27:

Let $\mathbf{M}$ be the inertia matrix of the object and ℓ_1 and ℓ_2 be the Lagrange multipliers which denote a set of constraint forces corresponding to both boundary constraints. Using the Lagrange dynamic method, a set of dynamic equations of all nodal points is formulated as

$$-\mathbf{F}_{2D(g)}^{rheo} + \mathbf{A}\boldsymbol{\ell_1} + \mathbf{B}\boldsymbol{\ell_2} - \mathbf{M}\ddot{\mathbf{u}}_N = 0. \tag{3.57}$$

Combining Eqs. 3.56, 3.27, 3.57, and considering $\mathbf{v}_N = \dot{\mathbf{u}}_N$, we can end up with a set of differential equations which describe the 2D dynamic behaviors of a rheological object formulated with nonlinear Green strain tensor. By numerically solving these equations, we can calculate the deformation and forces at each nodal points of the object.

3.2.3 Simulation Comparisons Between FE Models with Cauchy and Green Strain Tensors

In order to show the difference between the linear Cauchy strain and nonlinear Green strain, several FE simulations were performed with formulations of both strain tensors. The first simulation is under an input of constant velocities. Within the first 2 seconds, 3 nodal points on the top surface of the objects were pushed downward to a desired displacement of 0.01 m, 0.02 m, 0.03 m, and 0.04 m respectively, as shown in Fig. 3.4a. The deformed shapes were then held unchange for 2 seconds before releasing. The final recovered shapes and force responses from FE models with both strain tensors were shown in Fig. 3.4b and 3.4c. The second simulation was performed with different force inputs acting on the top right corner of the object, as shown in Fig. 3.5a. The force input can be easily incorporated with the above-mentioned FE model by adding an external force vector $\mathbf{F}^{ext}$ into Eq. 3.57. In this simulation, the top right corners of the objects were pulled upward with constant forces for 2 seconds. The deformed objects were then released with 2 seconds for recovery. The deformed and recovered shapes for both strain tensors were shown in Fig. 3.5b and 3.5c respectively.

From Figs. 3.4b and 3.5b we find that linear model with Cauchy strain tensor always yields linear behaviors, *i.e.,* the output is always proportional to the input and no matter the input is force or displacement. However, such behaviors will not happen in real rheological objects when the deformation is getting large. This is the limitation of the linear model. The nonlinear modeling is therefore necessary to cover such large deformation. Figures 3.4c and 3.5c show that output behaviors simulated with Green strain tensor do not have the proportional relationship with the inputs of both forces and displacements. When the inputs take small values (*e.g.,* Dis=0.01 m in Fig. 3.4 and F=0.01 N in Fig. 3.5), the outputs behaviors simulated by Cauchy and Green strain tensors have small differences. However, the differences increased with the increase of input values as shown in Fig. 3.4

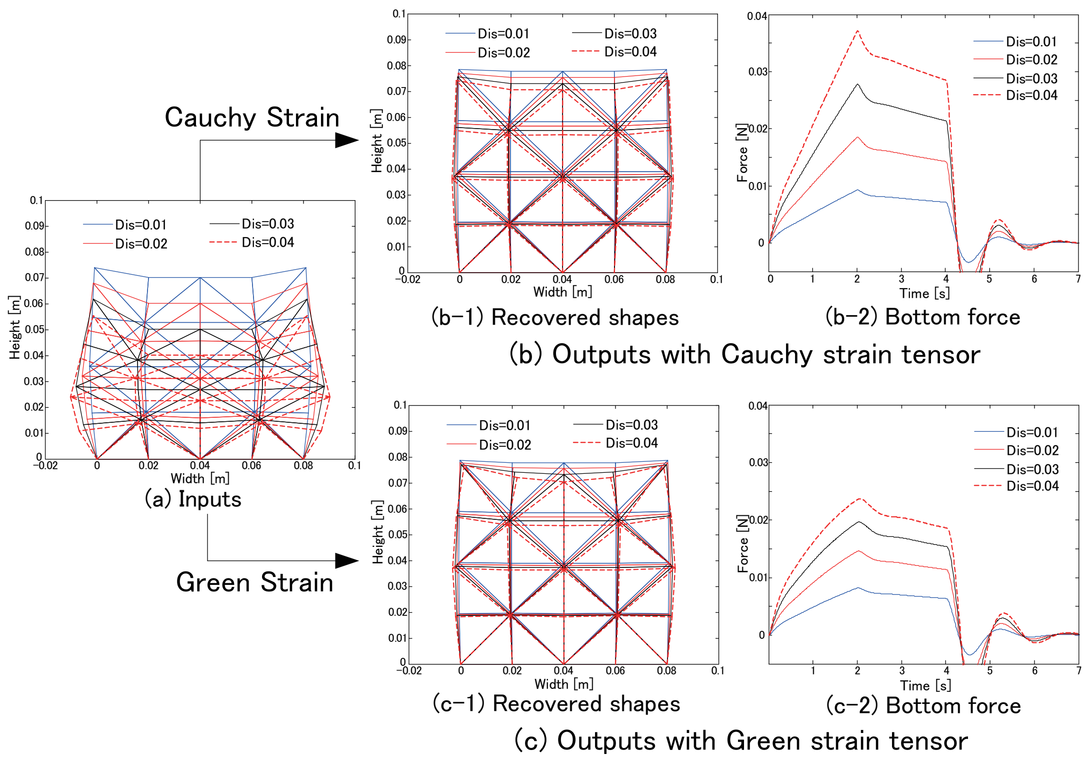

Figure 3.4: FE simulations of rheological behaviors under an input of different displacements, where the FE models were formulated with (b) Cauchy and (c) Green strain tensors.

and 3.5. Apparently, the simulation results with nonlinear Green strain tensor demonstrate more natural behaviors when the deformation becomes large.

In order to further compare the ability of both models for handling deformation with rotation motion, pushing and rolling simulations with both models were performed. An object with circular shape is pushed downward by an external instrument for 5 seconds with a constant velocity of 0.01 m/s and then the instrument starts to move left for another 5 seconds with the same velocity. The instrument is then moved upward and let the deformation to recover. The total simulation time is 15 seconds. The material properties of the object are represented by a parallel five-element physical model with parameters: $E_1 = 200$ Pa, $E_2 = 500$ Pa, $c_1 = 8000$ Pa·s, $c_2 = 5000$ Pa·s, and $c_3 = 100$ Pa·s. Several simulation snapshots using both models are given in Figs. 3.6 and 3.7, respectively. From Fig. 3.6, we find that linear Cauchy strain tensor results in some strange

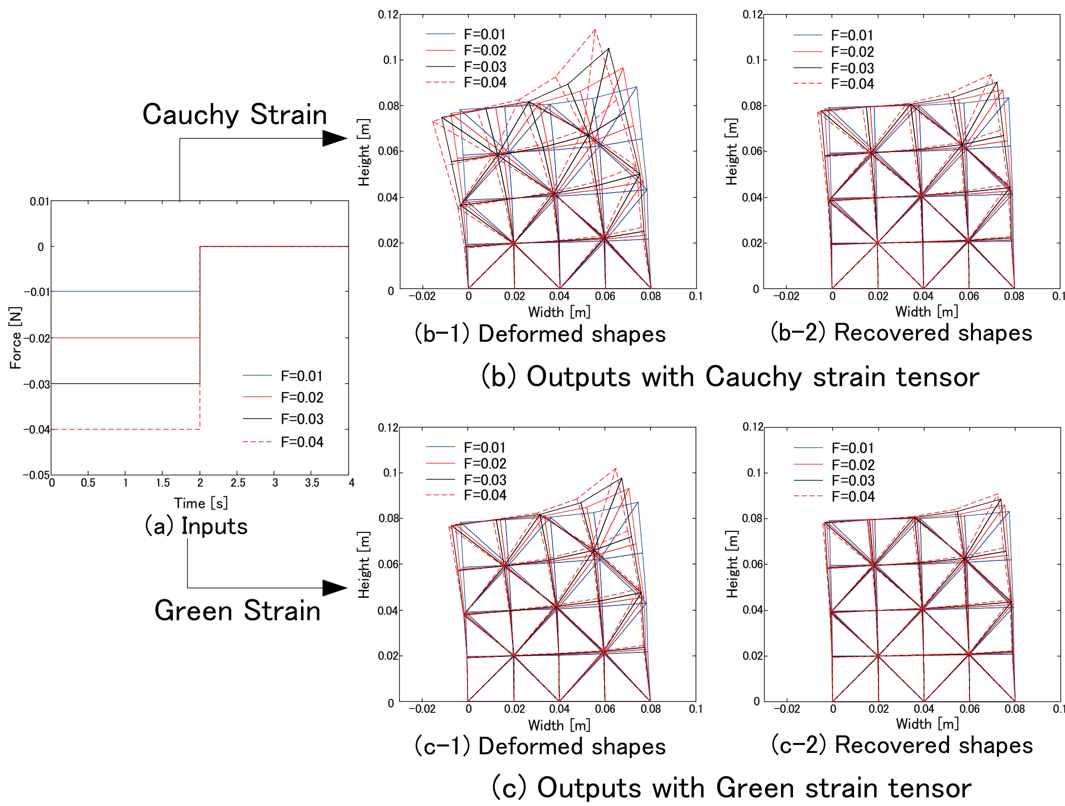

Figure 3.5: FE simulations of rheological behaviors under an input of different forces, where the FE models were formulated with (b) Cauchy and (c) Green strain tensors.

behaviors when simulating deformation with rotation motion. The triangular mesh of the object is expanded during rolling motion which should not happen in a real world object. After recovery, the object become much bigger (Fig. 3.6d) comparing with the initial shape (Fig. 3.6a). On the other hand, the object simulated with nonlinear Green strain does not show such strange behaviors, as shown in Fig. 3.7. We therefore conclude that the nonlinear Green strain tensor provide more natural deformation behaviors comparing with linear Cauchy strain tensor for dealing with large deformation and rotation. The modeling of contact between a rheological object and an external instrument shown in Figs. 3.6 and 3.7 will be introduced in the next chapter.

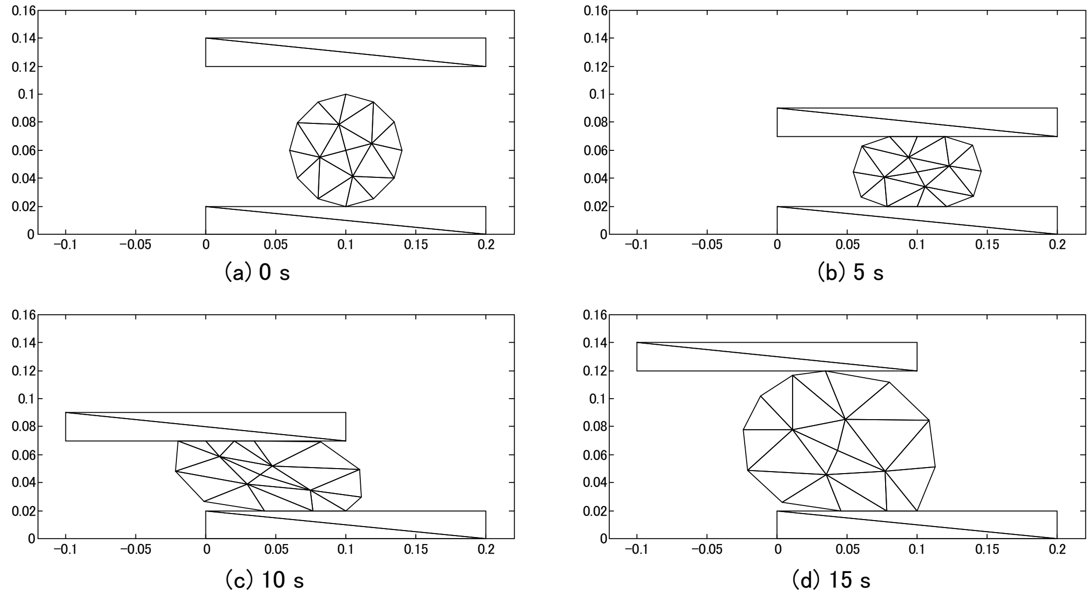

Figure 3.6: Simulation snapshots of a rheological object pushed and rolled by an external instrument, where the model of the object was formulated by linear Cauchy strain tensor.

3.3 FE Formulation with the Dual-Moduli Viscous Elements

As presented in Chapter 2, a five-element physically-based model with two dual-moduli viscous elements can yield simultaneous reproductions of both rheological forces and deformation behaviors. Now, let us extend the 1D physically-based model to a 2D FE dynamic model.

Recall that a stress-strain relationship in a Maxwell model is described by Eq. 3.17. Thus, replacing viscous coefficient c by dual-moduli viscous coefficient $\kappa\alpha + c$, we have the stress-strain relationship in a Maxwell model with a dual-moduli viscous element as:

$$\dot{\sigma} = -\frac{E}{\kappa\alpha + c}\sigma + E\dot{\epsilon}. \tag{3.58}$$

Then, by performing the same replacements for deriving 2D FE model (Eq. 3.25), we have a 2D FE formulation with a physically-based model including two dual-

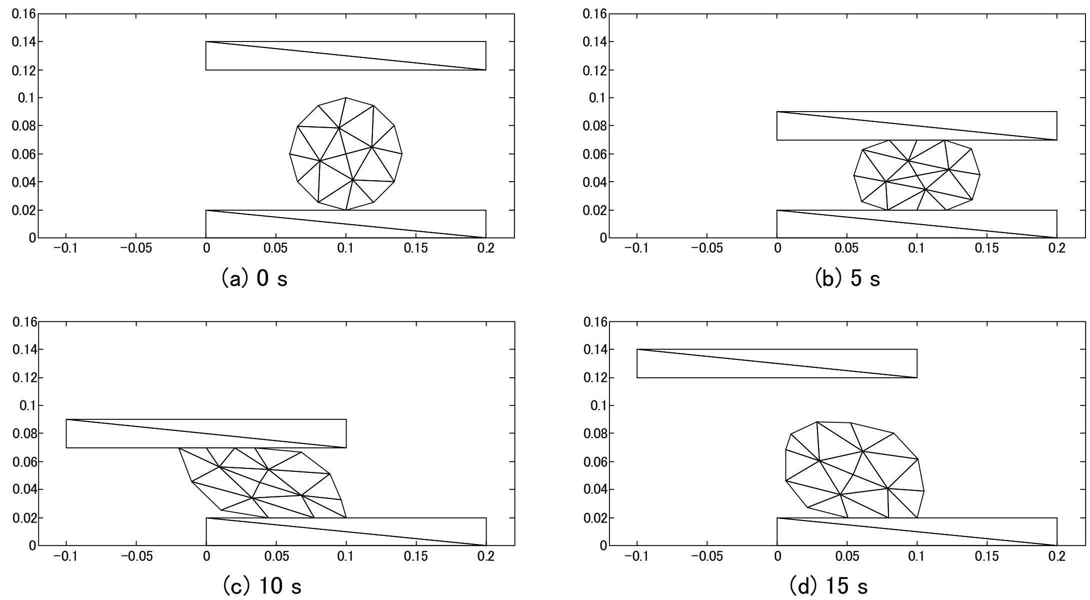

Figure 3.7: Simulation snapshots of a rheological object pushed and rolled by an external instrument, where the model of the object was formulated by nonlinear Green strain tensor.

moduli viscous elements shown in Fig. 2.9b as:

$$\begin{aligned}
\dot{\mathbf{F}}_1 + \frac{E_1}{\kappa\alpha_1 + c_1}\mathbf{F}_1 &= (\lambda_1^{ela}\mathbf{J}_\lambda + \mu_1^{ela}\mathbf{J}_\mu)\dot{\mathbf{u}}_N, \\
\dot{\mathbf{F}}_2 + \frac{E_2}{\kappa\alpha_2 + c_2}\mathbf{F}_2 &= (\lambda_2^{ela}\mathbf{J}_\lambda + \mu_2^{ela}\mathbf{J}_\mu)\dot{\mathbf{u}}_N, \\
\mathbf{F}_3 &= (\lambda_3^{vis}\mathbf{J}_\lambda + \mu_3^{vis}\mathbf{J}_\mu)\dot{\mathbf{u}}_N, \\
\mathbf{F}_{2D}^{rheo} &= \mathbf{F}_1 + \mathbf{F}_2 + \mathbf{F}_3,
\end{aligned} \tag{3.59}$$

This formulation also can be easily extended to 3D cases and models with the Green strain tensor as well by performing similar replacements as we did here.

3.4 Concluding Remarks

In this chapter, the formulations of FE dynamic models for simulating rheological behaviors were presented. We started from a 2D formulation of elastic model based on generalized Hooke's law and linear Cauchy strain tensor. The FE formulation of elastic deformation was then extended to 2D rheological model and further extended to handle 3D rheological deformation. Simulation results were given. In FE model with linear Cauchy strain tensor, the connection matrices are constant and can be prepared in advance which can yield more efficient calculations comparing with nonlinear models. However, FE model with linear Cauchy strain tensor is not suitable for simulating large deformation and rotation. We have therefore introduced nonlinear Green strain tensor to model large deformation and rotation. The derivation of FE model with Green strain tensor was presented. It also starts from the formulation of elastic deformation and further extended to rheological deformation by performing a series of replacements. Simulation results using FE models with Cauchy and Green strain tensors were then given to compare the differences between both models. We found that the FE model with nonlinear Green strain tensor yields more natural behaviors when dealing with large deformation and rotation. However, since the connection matrices are no longer constant, we are not able to prepare these matrices in advance and have to calculate them in every time step. This makes the FE simulation with nonlinear Green strain tensor very time-consuming. At last, we also presented FE model with a five-element physical model which includes two dual-moduli viscous elements.

Chapter 4

Modeling of Non-Uniform Object and Contact Interaction

The FE dynamic models presented in the last chapter are basically used to simulate uniform and isotropic objects. However most objects in the real world are not uniform and may include several different layers with different material properties. In addition, a contact interaction between an object and an external instrument may often happen during handling or manipulation. We therefore investigate the modeling of non-uniform layered objects and contact interaction between a rheological object and external instruments in this chapter.

4.1 FE Modeling of Non-Uniform Layered Object

When we started to model non-uniform objects, the first idea came to our mind is to set different parameters to each triangle. However, this idea does not work well. If we look at the dynamic equations presented in the last chapter, for instance, Eq. 3.25, we find that all the parameters are associated with nodal points rather than triangles. In other words, the physical parameters in our FE models are point-wise instead of triangle-wise, which makes the difficulty of choosing appropriate parameters for the boundary nodal points between two layers when dealing with

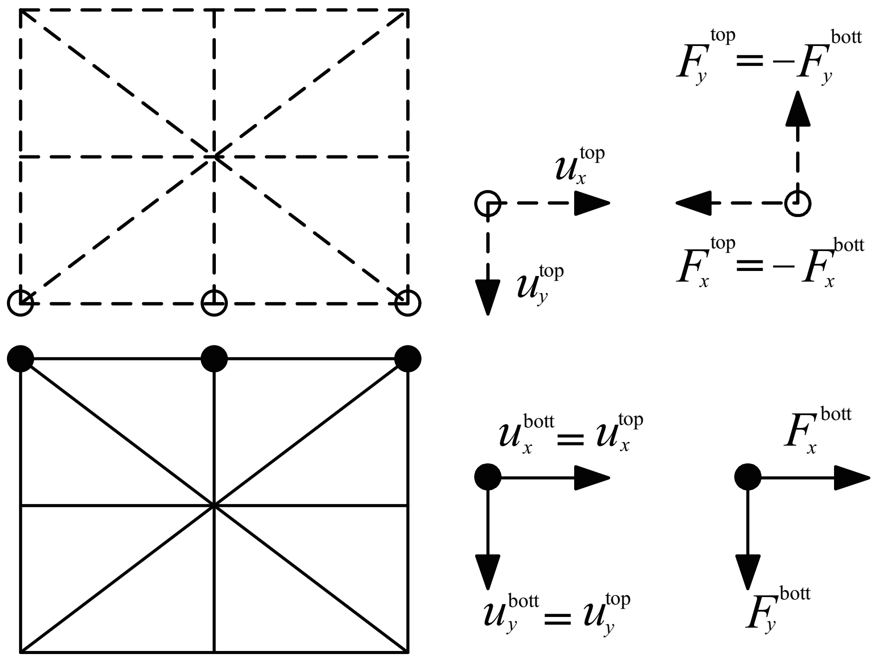

Figure 4.1: Modeling strategy for non-uniformed layered object.

layered objects. We have therefore proposed the following idea for modeling non-uniform layered objects.

Considering a two-layered object with different material properties in each layer, we artificially separate this non-uniform layered object into two uniform objects with their own properties during simulation, as shown in Fig. 4.1. Note that the boundary nodal points on both layers (*i.e.*, the hollow nodes on the top layer and the solid nodes on the bottom layer) always have the same displacements (as they are in fact the same points), *i.e.*:

$$\mathbf{u}^{bott} = \mathbf{u}^{top}. \tag{4.1}$$

The modeling of this layered object can therefore be divided into the modeling of two uniform objects with a displacement constraint on the boundary nodal points. As shown in Fig. 4.1, we imposed the displacements of the top boundary points onto the bottom boundary points during simulation by applying a displacement constraint of Eq. 4.1. Using the CSM, this constraint can be formulated as:

$$(\ddot{\mathbf{u}}^{bott} - \ddot{\mathbf{u}}^{top}) + 2\omega(\dot{\mathbf{u}}^{bott} - \dot{\mathbf{u}}^{top}) + \omega^2(\mathbf{u}^{bott} - \mathbf{u}^{top}) = 0. \tag{4.2}$$

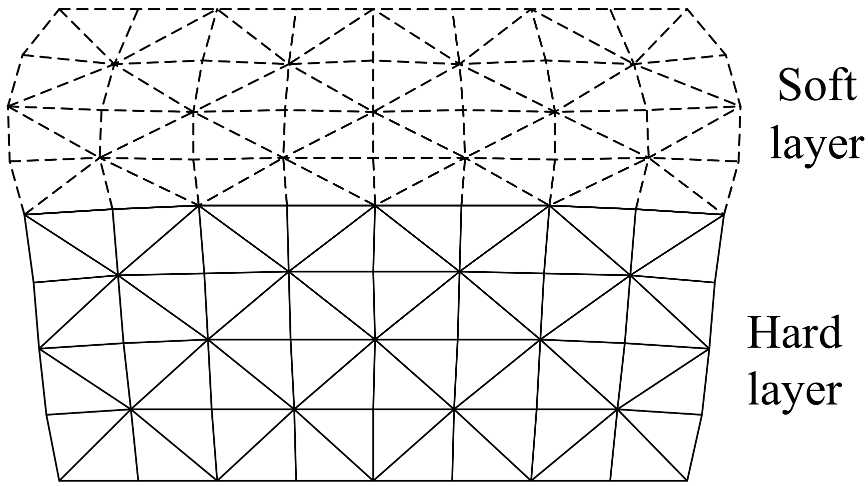

Figure 4.2: Deformed shape of a two-layered object with soft material in the top layer.

Accordingly, the constraint forces generated on the bottom boundary points are reacted back to the top boundary points, *i.e.*, $\mathbf{F}^{top} = -\mathbf{F}^{bott}$. By integrating Eq. 4.2 into the dynamic equations of the object on the bottom layer and substituting $\mathbf{F}^{top}$ as an external force into the dynamic equations of the object on the top layer, we can derive an FE model for simulating rheological behaviors of a non-uniform layered object. A typical deformation behavior of a two-layered object is shown in Fig. 4.2, where the top layer is three times softer (all parameters are three times smaller) than the bottom layer. Another example, as shown in Fig. 4.3, is a semi-spherical object made of two types of materials (denoted by solid and dash line, respectively) grasped by a robot hand. We can see that our modeling method demonstrated natural behaviors of non-uniform layered objects. In addition, this 2D FE model can be easily extended to a 3D case by changing the triangular meshes to tetrahedral meshes and adding z-axis components to all the vectors and matrices.

4.2 Contact Modeling

The contact modeling is always required when dealing with interactions between a deformable object and an external instrument and is important for many applica-

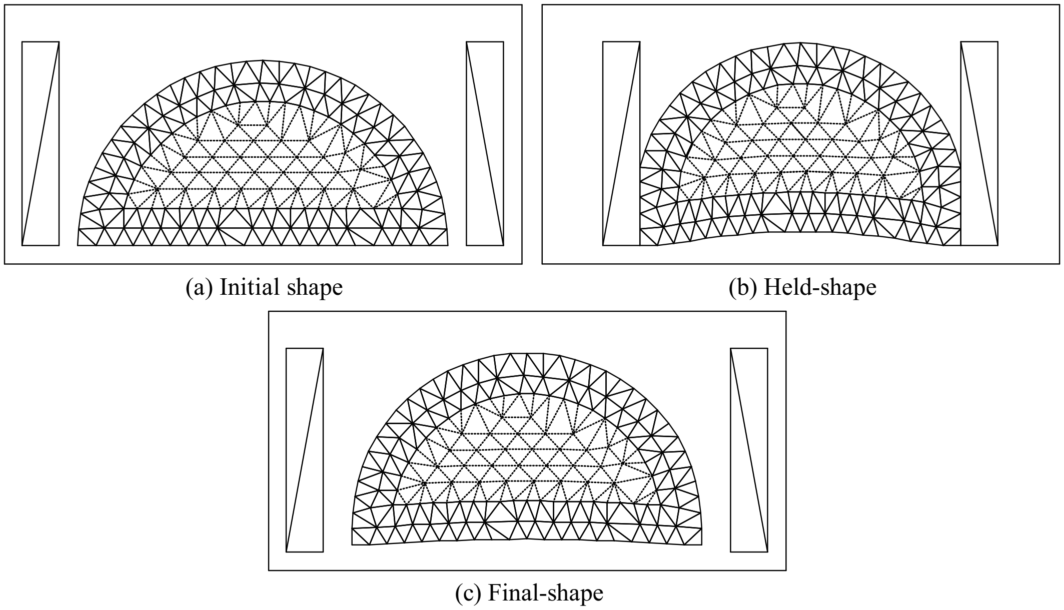

Figure 4.3: Deformation behaviors of a semi-spherical object made of two types of materials grasped by a robot hand.

tions, such as food manufacturing simulation and surgical operation. Depending on the contact area between the object and the external instrument, we roughly divide contact models into two categories, as shown in Fig. 4.4. The modeling of these two kinds of contacts, however, is quite different. In wide area contact (Fig. 4.4a), contact modeling only requires a detection of contact moment and a constraint condition between the instrument and the object can then be imposed. On the other hand, in small area contact (Fig. 4.4b), the object needs a remeshing or at least a local remeshing to ensure that the contact nodes on the instrument are coincided with some nodes on the object. Otherwise, the instrument and the object may penetrate each other in some regions. In the following subsections, we will investigate the contact modeling of both categories.

4.2.1 Wide Area Contact

In the modeling of wide area contact, we should keep the object mesh unchange and only focus on the detection of contact moment, losing contact moment, and imposing constraints on the contact nodes.

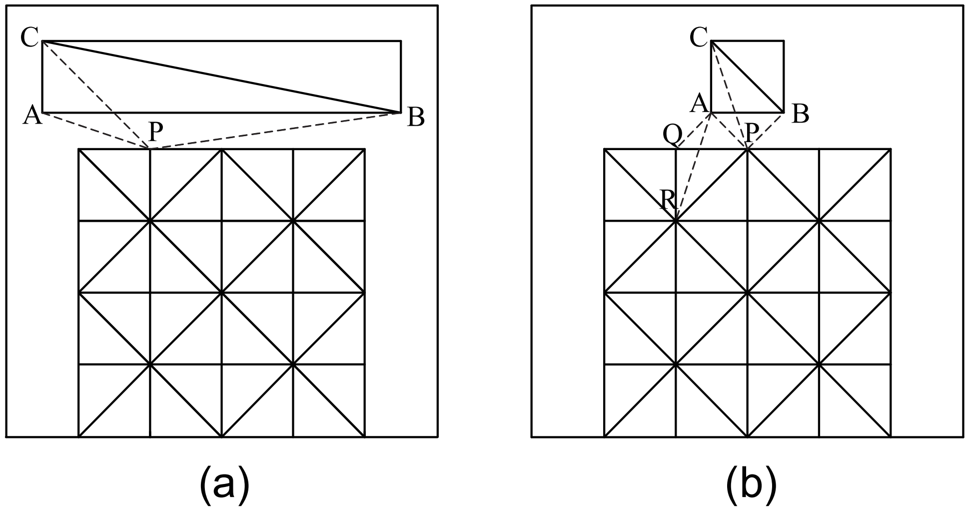

Figure 4.4: Two kinds of contact models: (a) wide area contact, and (b) narrow area contact.

4.2.1.1 Contact Moment Detection

As shown in Fig. 4.4a, the object and the instrument are constructed by triangular meshes. Since the instrument is assumed to be rigid, we can use a simplest mesh (only two triangles) for its modeling. During simulation, the instrument is moving downward with a constant velocity to compress the object with a specific displacement. We virtually connect one node P on the object with three nodes of a triangle (△ABC) on the instrument to construct three triangles: △PAB, △PBC, and △PCA. Let $\triangle \mathrm{P}_i\mathrm{P}_j\mathrm{P}_k$ be an arbitrary triangle with three vertices: P_i, P_j, and P_k. Coordinates of these vertices are $[x_i, y_i]$, $[x_j, y_j]$, and $[x_k, y_k]$, respectively. We define a signed area of a triangle as:

$$\triangle\ \mathrm{P}_i\mathrm{P}_j\mathrm{P}_k = \frac{1}{2}[x_i, x_j, x_k]\begin{bmatrix} y_j - y_k \\ y_k - y_i \\ y_i - y_j \end{bmatrix}. \tag{4.3}$$

This signed area is positive if the triangular loop (the order of the three vertices of a triangle) is counter clockwise while is negative if the loop is clockwise. Now, let us check the signed areas of the triangles △PAB, △PBC, and △PCA shown in Fig. 4.4a, we find that the area of △PAB is negative. However, once the nodal point P is located on any edge or inside of the triangle △ABC, each signed area of above three triangles will became zero or positive. This can serve as a criterion to detect the contact moment and start the contact constraint. In every time step, we check all the nodal points on the object to see if any of them is in contact with the instrument or not. The algorithm can be roughly described as follows:

In each time step

for loop: each nodal point on the object (node P for instance)

for loop: each triangle on the instrument ($\triangle$ABC *for instance)*

if $\triangle PAB \geq 0$ *and* $\triangle PBC \geq 0$ *and* $\triangle PCA \geq 0$

Start contact;

end if, for.

4.2.1.2 Constraints for Contact Nodes

Once the instrument was in contact with the object, the contact points on both instrument and object would have the same displacement and velocity. Let $\mathbf{v}_c^{ins}$, $\mathbf{v}_c^{obj}$, $\mathbf{u}_c^{ins}$, and $\mathbf{u}_c^{obj}$ be the velocity and displacement vectors of the contact points on the instrument and object respectively after contact moment. Using CSM, a set of constraint equations are formulated as:

$$\mathbf{C}^T(\dot{\mathbf{v}}_c^{obj} - \dot{\mathbf{v}}_c^{ins}) + \mathbf{C}^T[2\omega(\mathbf{v}_c^{obj} - \mathbf{v}_c^{ins}) + \omega^2(\mathbf{u}_c^{obj} - \mathbf{u}_c^{ins})] = 0, \qquad (4.4)$$

where constant matrix $\mathbf{C}$ denotes which nodal points on the object are in contact. Note that vectors $\mathbf{v}_c^{ins}$ and $\mathbf{u}_c^{ins}$ of arbitrary point on edge AB (Fig. 4.4a) can be obtained from velocities and displacements of vertices A and B by using interpolation. Combining Eq. 4.4 with the FE model presented in Chapter 3, we are able to simulate the contact interaction between a rheological object and an external instrument.

4.2.1.3 Losing Contact and Switching Parameters

Once the instrument started to move back after pushing and holding operations, we at first thought that it is necessary to determine the losing contact moment and then release the constraint accordingly. However, we found out that we do not have to do that and our contact model has an ability to automatically lose the contact as long as the instrument started to leave the object. Let us recall the idea of our contact model and dig a little bit deeper. During each time step in simulation, if any nodal point on the object is located inside the instrument, it will be pushed down to coincide with the instrument boundary after this time step due to the CSM constraint. Note that this pushing down action will happen in next time step but not in the current time step. In other word, the CSM constraints for the points in contact are always performed one time step later than the time step where the contact happens. Now, let us consider the losing contact situation. When the instrument started to move back, the object will also start to recover. If the recovery rate of the object is faster than the rate of instrument moving back, the contact is still in effect. However, the recovery rate of the object is always decreasing with time. In a certain time step, once the recovery rate of the object is slower than the moving back rate of the instrument, the nodal points in contact will be located outside the instrument boundary. This separation will happen because the CSM constraints are always one time step later than the detection of contact as we just discussed above. Once the separation happens, the contact constraint therefore will be automatically released. This made our contact model much simple and natural.

According to the above discussion, the moment of in contact and losing contact can be determined without explicitly using of simulation time. This can also serve as a good criterion for dual-moduli viscous element to switch parameters, as discussed in Section 2.5. We therefore use a flag to memorize the contact points and to serve as the criterion. The algorithm for contact modeling now becomes:

In each time step

for loop: each nodal point on the object (node P for instance)

Initialize: flag(p)=0;

for loop: each triangle on the instrument ($\triangle$ABC *for instance)*

if $\triangle PAB \geq 0$ *and* $\triangle PBC \geq 0$ *and* $\triangle PCA \geq 0$

flag(p)=1;

Start contact;

end if, for

We will switch the parameters when all contacting points lose their contacts. The switch function κ now becomes:

$$\kappa = \begin{cases} -1 & \text{flag(p)} = 0 \qquad \forall \text{p} \in \text{object}, \\ 1 & \text{otherwise.} \end{cases} \tag{4.5}$$

Now, we are able to perform the contact simulation with the parameter switching strategy to reproduce both rheological force and deformation behaviors. The next subsection will demonstrate some simulation results to show the ability of our contact model.

4.2.1.4 Contact Simulation

Using the proposed FE contact model, we are able to simulate deformation behaviors of the rheological objects undergoing a compressing, holding, and releasing procedures. The first example is a semi-circular shaped object deformed by a flat squared instrument. Total simulation time is 16 seconds. The instrument moves down 25 mm in first 4 seconds with a constant velocity. Then, the instrument stops pushing and maintains the deformed object for another 4 seconds. The instrument then moves back to the original position within 4 seconds. After the instrument moves back to the original position, the object still has 4 seconds to recover. Some snapshots of simulation results are shown in Fig. 4.5, where the FE model with dual-moduli viscous elements is employed. All the parameters used here are estimated from real Japanese sweets materials and how to estimate these parameters will be discussed in the next chapter. To compare the different performance, simulation snapshots of FE model without dual-moduli viscous elements are also given in Fig. 4.6. We can easily see the differences between Figs. 4.5 and 4.6. At simulation time 8.2 s, the instrument and object has lost contact

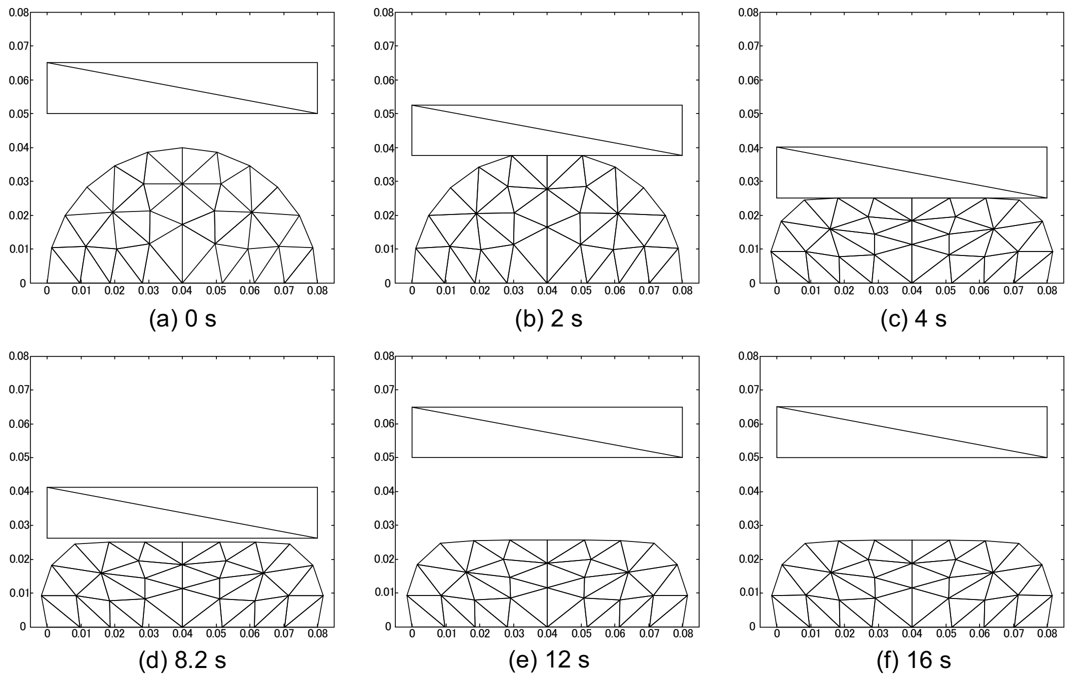

Figure 4.5: Simulation snapshots of a semi-circular object pushed down by a flat squared instrument with parameter switching strategy.

in Fig. 4.5d but still in contact in Fig. 4.6a. The final recovered shapes of both cases are also quite different. The deformation recovery takes longer time if we do not use the dual-moduli viscous elements.

The second example is a circular object operated by two external instruments with one from the top and another one from the bottom, as shown in Fig. 4.7. The bottom instrument is static and the top instrument is moving down to push the object. Figure 4.7b showed that the object have already deformed and contacted with the bottom instrument due to gravity before the top instrument touches the object. The final recovered shape is also not symmetrical relative to the horizontal axis due to the gravity. Figure 4.7 shows the simulation results of FE model with dual-moduli viscous elements. Some snapshots of simulation results without dual-moduli viscous elements are also given in Fig. 4.8 to show the differences. In addition, simulation results of contact model also can be found in Figs. 3.5 and 3.6 in the last chapter.

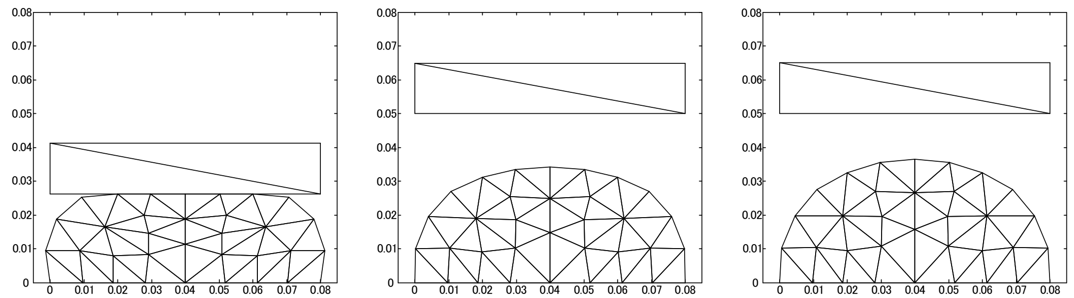

(a) 8.2 s (b) 12 s (c) 16 s

Figure 4.6: Simulation snapshots of a semi-circular object pushed down by a flat squared instrument without parameter switching strategy.

4.2.2 Narrow Area Contact

Different with wide area contact, the modeling of narrow area contact requires either a global remeshing or a local remeshing because the contact area of the instrument is smaller than the area of the object as shown in Fig. 4.4b. Moreover,same with wide area contact, narrow area contact also needs a detection of contact moment, which will serve as a trigger to start the performance of remeshing.

4.2.2.1 Object Remeshing

In order to generate triangular mesh automatically, we have employed a MATLAB toolbox of 2D meshing routines named MESH2D, which allows automatic generation of unstructured triangular meshes for general 2D geometry. For using MESH2D, one all need to do is to provide some boundary points which can best describe the object shape (piecewise linear geometry input). By setting some parameters, we also can control the mesh resolution or specify some special nodal points and some special connections between some nodal points. In our application, we only use the basic function and input several boundary points into MESH2D. In every time step during integration, we perform the following processes:

1. Perform the contact detection to see if the instrument and the object are in contact or not. If it is not in contact, jump to step 2. If it is in contact,

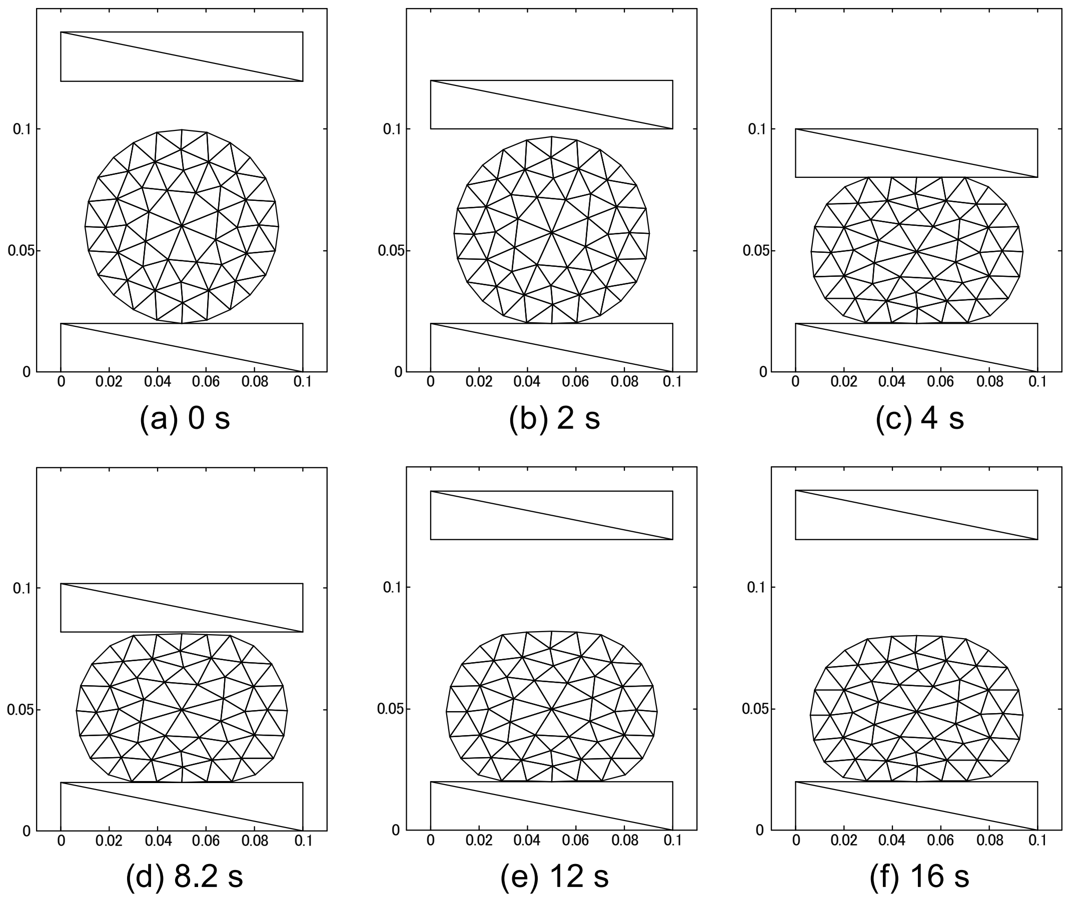

Figure 4.7: Simulation snapshots of a circular object operated by two instruments with parameter switching strategy.

jump to step 3 and perform the steps followed.

2. Using the initial triangular meshes for both object and the instrument to calculate all the variables and finish the calculation for this time step.

3. Remember the current coordinates of the contact points on the instrument. These points and the initial boundary points will serve as a set of new boundary points to generate the new mesh.

4. Perform the remeshing using MESH2D and recalculate all the required matrices, such as the inertial matrix and connection matrices.

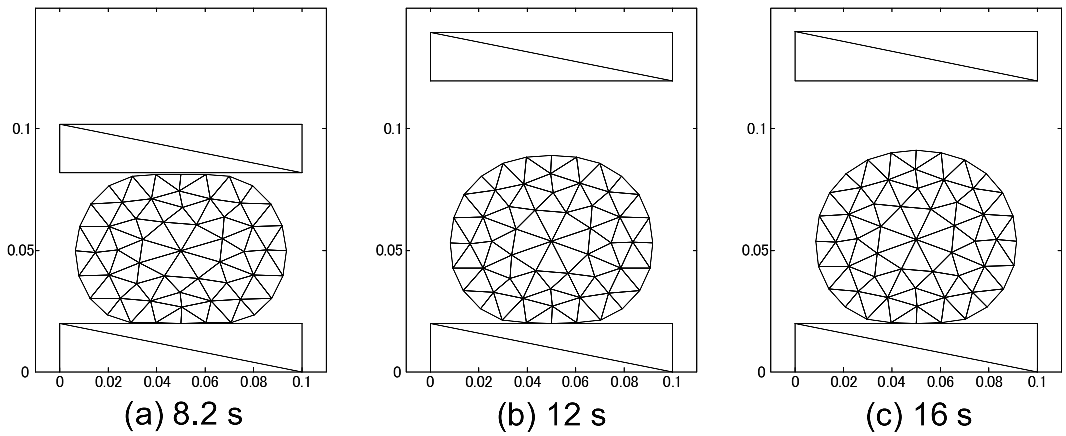

Figure 4.8: Simulation snapshots of a circular object operated by two instruments without parameter switching strategy.

5. Use the new mesh and new matrices to calculate all the variables needed to be integrated and finish the calculation of the current time step.

Note that since the remeshing and calculations of connection matrices, which are usually quite large, must be performed inside the time integration, this contact simulation with remeshing is quite time-consuming.

4.2.2.2 Contact Simulation with Remeshing

A simulation was conducted to show the performance of narrow area contact model with remeshing. A 2D squared object was deformed by a instrument whose contact area is a quarter of the contact area of the object. The instrument and the object have an initial distance of 0.2 m. The instrument was moved down 0.4 m from the initial position in 2 seconds with a constant velocity. Before releasing, the deformed object was maintained for 2 seconds. Then, the instrument was moved back to its initial position in 2 seconds with a constant velocity. After this, the deformed object still had another 2 seconds to recover. The total simulation time is therefore 8 seconds. Several simulation snapshots are given in Fig. 4.9. We can see that the instrument starts to contact with the object at the moment of 1 s and the two contact points in the instrument are not coincide with any nodal point on the object. In the next time step, the object is remeshed and now two

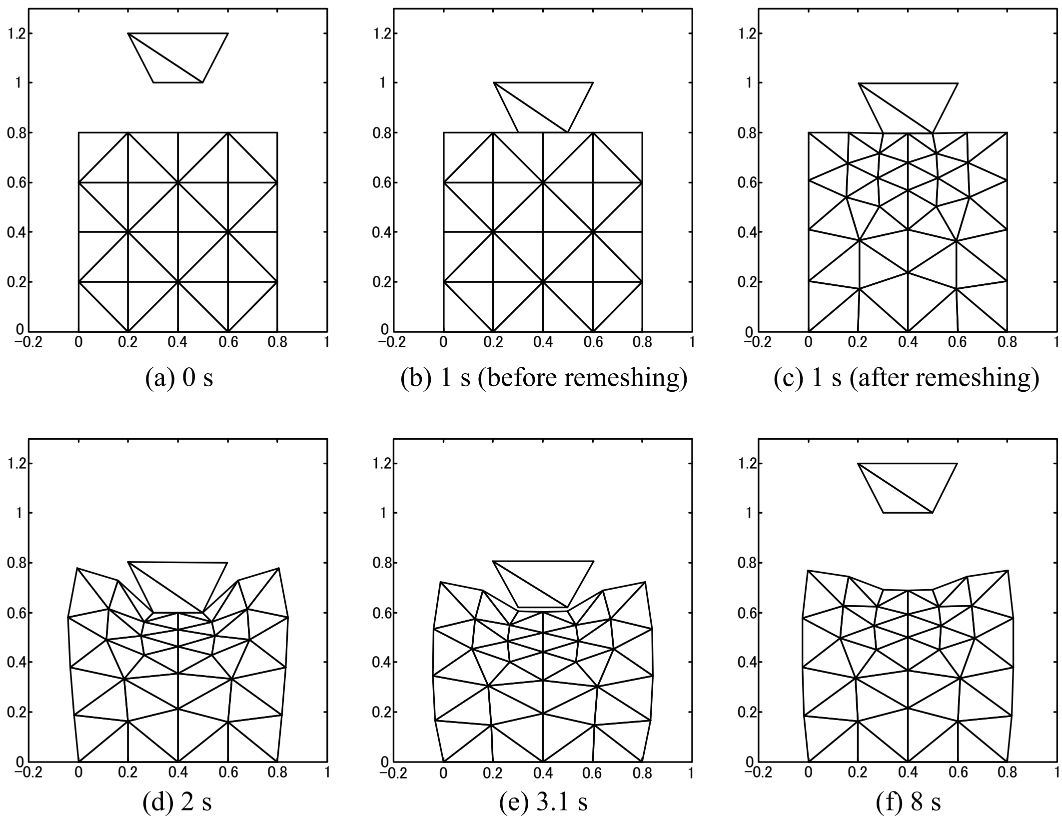

Figure 4.9: Simulation results of narrow area contact with remeshing.

new points on the object are generated and are coincided with the corresponding nodes on the instrument. The constraints are then imposed on these contact points to perform the contact simulation.

4.3 Concluding Remarks

In this chapter, the modeling of non-uniform layered objects and contact interaction between rheological object and external instrument were formulated. We artificially separated a non-uniform layered object into several uniform ones and performed the uniform simulation independently. The non-uniform behaviors were then obtained by imposing a constraint on the nodal points of the boundary between both layers. This idea works very well for different shaped objects. For modeling of contact interaction, we roughly divided the contact models into two categories depending on the contact areas of the object and the instrument. For wide area contact, the only thing we need to do is to detect the contact moment and then impose constraints on the contacting points. However for narrow area contact, we have to perform object remeshing or at least local remeshing during the simulation. To conduct the remeshing, we need an automatic mesh generation during simulation. This can be done by using a MATLAB toolbox named MESH2D. In each time step, the detection of contact moment is also performed. Once the contact starts, the remeshing is performed and then the constraints are also imposed on the contact nodal points. Simulation results were performed to demonstrate the performance of both contact models.

Chapter 5

Parameter Estimation

In order to accurately simulate the behaviors of real objects, the properties (physical parameters) have to be determined in advance. However, the estimation of those parameters is a challenging work, especially for rheological objects which always yield residual deformation after a loading-unloading operation. These estimated parameters have to be able to regenerate the rheological force, deformed shape (*e.g.*, the held-shape) during the operation and the final deformed shape (the final-shape) after recovery as well. This chapter introduce the methods used in our work to estimate physical parameters for simultaneous reproductions of both rheological forces and deformation, especially the residual deformation behaviors. At first, let us investigate the contributions of mesh resolution and each parameter to the rheological behaviors based on 2D FE simulation.

5.1 FE Simulation Analysis

Let us take the FE model presented in Section 3.1.2 as an example to perform the simulation analysis. This 2D FE model includes 6 unknown physical parameters, *i.e.*, Young's moduli E_1, E_2, viscous moduli c_1, c_2, c_3, and Poisson's ratio γ. We suppose that a 2D flat-squared object with a size of $0.08\,\mathrm{m}\times0.08\,\mathrm{m}$ was fixed on the ground and the entire top surface was pushed down with a constant velocity of $0.002\,\mathrm{m/s}$ during time 0 to 10 seconds. This time period is referred to as pushing phase. The deformation was then held for 10 seconds before releasing. Similarly, this time period is referred to as holding phase. The deformed shape in this phase is called held-shape accordingly. After releasing the constraint, the deformed object still has 20 seconds to recover from the deformation. The deformed shape in the end of simulation is referred as final-shape accordingly. Therefore, the total simulation time is set to 40 seconds. Such pushing and holding procedures are used throughout our simulation analysis and similar ones are also employed in our experimental validations. One may ask why we use this simple simulation or experimental setups. We believe that firstly the material properties (physical parameters) will not differ even though the object may have different sizes or shapes or may be subjected to different operations. Secondly, if we could estimate all the parameters by using a simple setup, there would be no problem to estimate them using more complicated setups. Now, let us see how the mesh resolution and physical parameters will affect the simulation behaviors.

5.1.1 Contribution of Mesh Resolution

As we all known, mesh resolution in FE simulation significantly affects the simulation cost and the simulation accuracy as well. In a certain application, we therefore have to compromise between time cost and simulation accuracy. Since the objects with flat-squared shape are used in most of our simulations and experimental tests, it is necessary to investigate the influence of mesh resolution on our applications. Simulation results with different mesh resolutions are given in Fig. 5.1, where mesh resolution 2×2 means the width and height sides are both divided into two segments. From Fig. 5.1, we can see that the mesh resolution of 4×4 is fine enough to simulate the behaviors for this simple setup. Finer

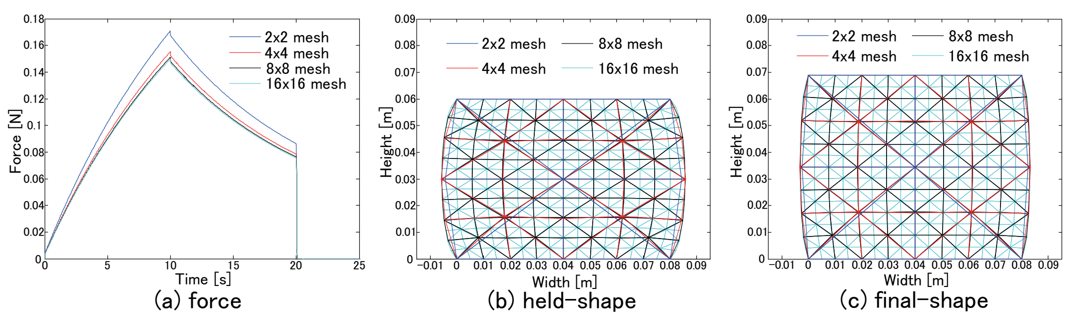

Figure 5.1: Simulation results with different mesh resolutions.

mesh resolutions do not yield significant difference in both force and deformation behaviors. We have therefore employed 4×4 mesh resolution throughout our simulations and parameter estimation processes.

5.1.2 Contributions of Young's Moduli

Figures 5.2 and 5.3 show simulation behaviors using different Young's moduli E_1 and E_2, respectively. We can see that both elastic moduli have similar influences on the rheological behaviors. Larger values of those moduli yield larger force amplitudes in the pushing phase and faster decay in the holding phase. This can be explained by Eqs. 2.20 and 2.21, where the value of E_i/c_i determines the increasing and decreasing speed of force amplitude during pushing and holding phases respectively. Note that the held-shapes with different Young's moduli are exactly the same. On the other hand, the final-shapes are dependent on these moduli. Larger values resulted in larger residual (permanent) deformation. Considering the five-element physical model (the last row of Fig. 2.2b), during pushing phase, all elastic elements (denoted by E_1 and E_2) and viscous elements (denoted by c_1, c_2, and c_3) are compressed with some deformation. During holding phase, the total deformation of the object is kept unchange. However, the deformation generated in the elastic elements will change to the deformation of viscous elements, which also yields the force relaxation (reduction) behavior in holding phase. Larger elastic moduli (E_1 or E_2) therefore produce bigger deformation changing rate and finally yield larger residual deformation in a certain time period.

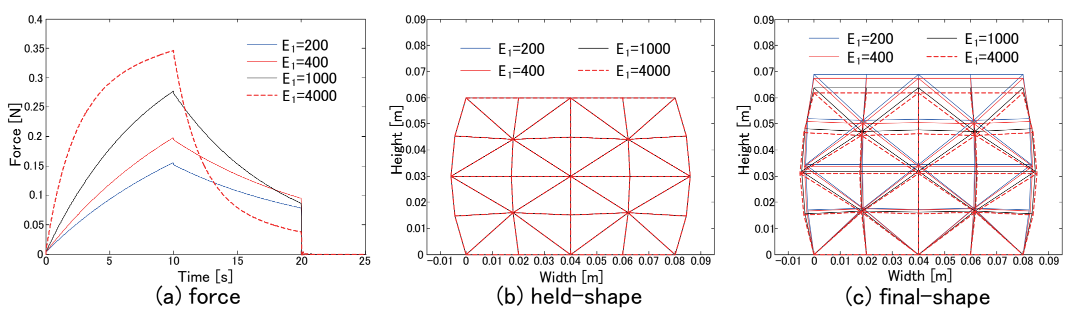

Figure 5.2: Simulation results with different Young's modulus E_1.

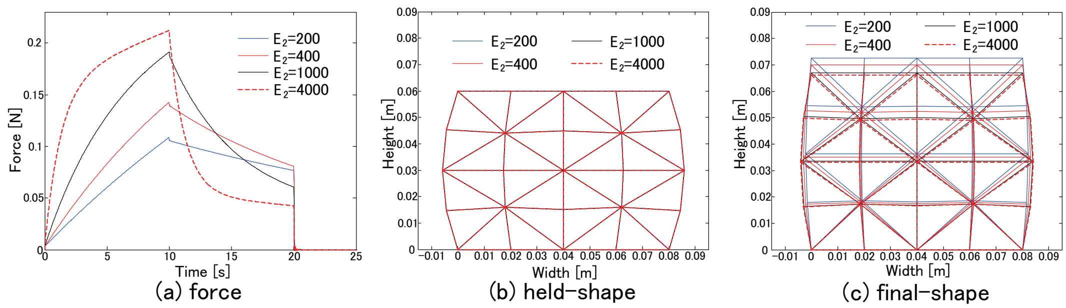

Figure 5.3: Simulation results with different Young's modulus E_2.

5.1.3 Contributions of Viscous Moduli

Figures 5.4 and 5.5 show different simulation behaviors using different viscous moduli c_1 and c_2, respectively. We can see that parameters c_1 and c_2 also have similar influences on the rheological behaviors. Larger values of c_1 and c_2 yield larger force amplitudes in pushing phase and slower decay in holding phase. Explanations also can be obtained by looking at Eqs. 2.20 and 2.21. Similarly, both parameters c_1 and c_2 do not affect deformed shapes during holding phase. However, larger values of c_1 and c_2 yield smaller residual (permanent) deformation. During the holding phase, larger viscous moduli c_1 and c_2 actually will slow down the deformation changing rate. Therefore, less deformation will be changed to viscous element and more deformation will be recovered after releasing, which results in less residual deformation.

Figure 5.6 shows different simulation results with different values of viscous modulus c_3. If we compare Eqs. 2.20 and 2.21 at time t_p (10 s in this case),

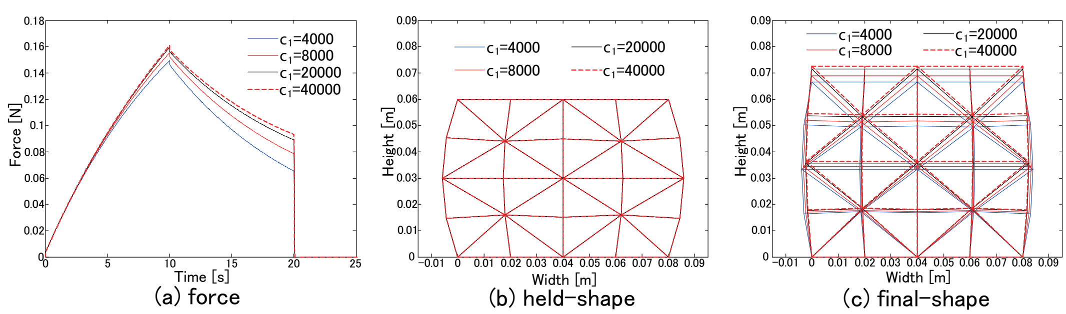

Figure 5.4: Simulation results with different viscous modulus c_1.

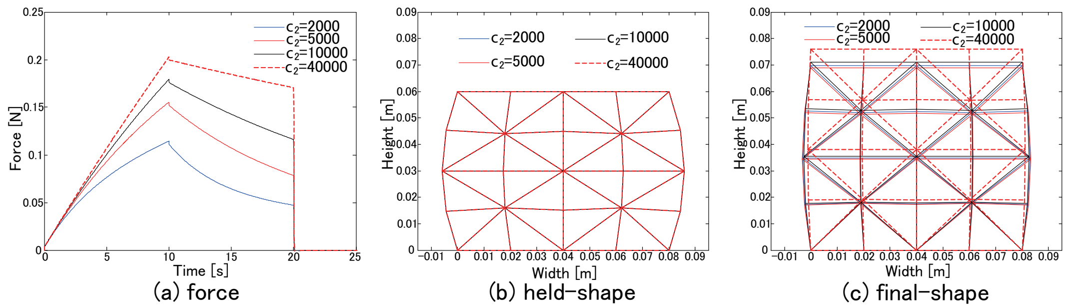

Figure 5.5: Simulation results with different viscous modulus c_2.

we find that c_{n+1} (c_3 in this case) is responsible for the sudden drop in force at time t_p. The force behaviors in the holding phase are the same with different parameter c_3, as shown in Fig. 5.6a. Once again, the held-shape is not dependent on parameter c_3. However, c_3 has a little effect on the final-shapes but not in a significant way, as shown in Fig. 5.6c. Since parameter c_3 does not affect simulated behaviors in a significant way, one may ask why we have to include this viscous element in our FE model. Actually, without using parameter c_3, we are still able to reproduce rheological force and deformation. However without using c_3, vibration always happens in both force and displacement curve after releasing, as shown in Fig. 2.7b. A small value of parameter c_3 can remove this vibration and without changing the simulated behaviors significantly.

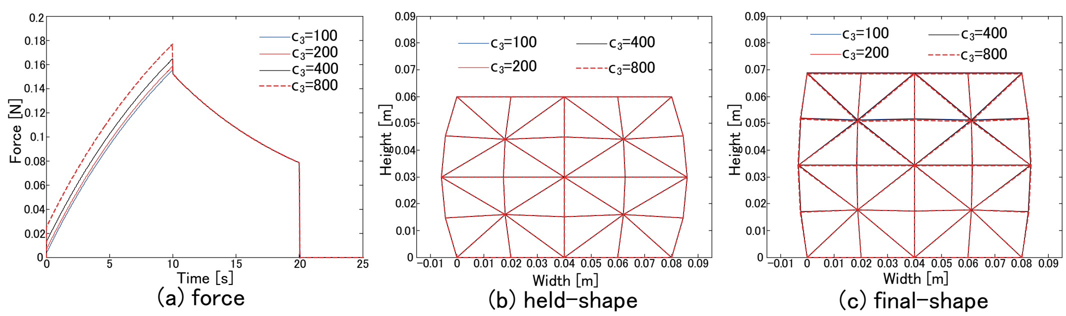

Figure 5.6: Simulation results with different viscous modulus c_3.

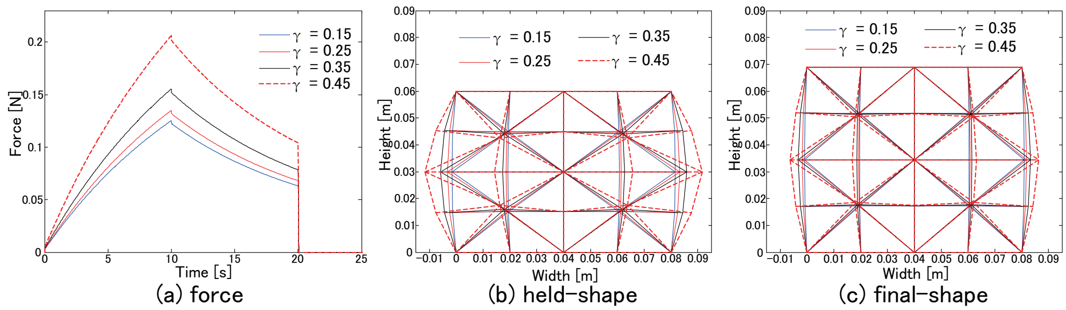

Figure 5.7: Simulation results with different Poisson's ratio γ.

5.1.4 Contribution of Poisson's Ratio

Figure 5.7 shows different simulated behaviors using different values of Poisson's ratios γ. We can see that parameter γ affects all the rheological behaviors: force, held-shape, and final-shape. Larger parameter γ results in larger force responses and larger transverse deformation behaviors but does not affect the normal deformation in both held-shape and final-shape. This coincides with the definition of Poisson's ratio, *i.e.*, a ratio between the transverse strain and axial strain. We summarize the influences of all physical parameters (five-element physical model for instance) on rheological behaviors in Table 5.1. Interestingly, we find that only Poisson's ratio γ affect the held-shape and all the other parameters do not affect this shape at all. This feature allows us to estimate Poisson's ratio γ separately.

Table 5.1: Influences of physical parameters on rheological behaviors

Parameter	Force in pushing	Force relaxation	Held-shape	Final-shape
E_1	○	○	×	○
E_2	○	○	×	○
c_1	○	○	×	○
c_2	○	○	×	○
c_3	○	×	×	○
γ	○	○	○	○

5.2 Parameter Estimation Based on Inverse FE Optimization

Parameter estimation of deformable objects has been studied intensively, as presented in Chapter 1. One popular and robust method is based on optimization, which aims at minimizing the difference between simulation or calculation results and experimental measurements. When the simulation or calculation is performed by using FE model, this optimization process is usually called inverse FE optimization (Fig. 1.3), *i.e.*, the FE simulation or calculation is iterated with updated physical parameters until the differences between the simulation and experiment becomes minimal. In our work, this method was also used to determine the physical parameters of rheological objects. However, due to the presence of residual deformation, accurately reproductions of both rheological forces and residual deformation are quite challenging and parameter estimation for capturing both force and residual deformation is also quite difficult. In order to deal with this problem, we firstly proposed a parameter estimation method with the following three steps:

1. Minimize the held-shape to estimate Poisson's ratio γ;
2. Calculate the summation $\sum_{i=1}^{n} c_i$ to approximate the final-shape;
3. Minimize the force differences to estimate the remaining parameters with a constraint of summation $\sum_{i=1}^{n} c_i$ from the second step.

The details about each step will be presented in the following subsections.

5.2.1 Estimation of Poisson's Ratio γ

As we discussed in the last section, only Poisson's ratio γ affects the held-shape and other parameters do not affect this shape at all. We can therefore estimate γ separately by minimizing the difference of held-shapes between simulation and experiments. The objective function used for this optimization is given by:

$$E(\gamma) = \sum_{i=1}^{m} \|\mathbf{x}_i^{sim}(\gamma) - \mathbf{x}_i^{exp}\|^2, \tag{5.1}$$

where $\mathbf{x}_i^{sim}(\gamma)$ and $\mathbf{x}_i^{exp}$ are the displacement vectors from simulation and experiment, respectively. Scalar $m = 2N$ with N be the total number of nodal points calculated in this optimization problem. The optimization is terminated when the tolerance on the function value $E(\gamma)$ is less than 1×10^{-12} or the tolerance on parameter γ is less than 1×10^{-6}. Optimization results will be presented in the next chapter and we can find a global minimum for this optimization problem actually.

5.2.2 Calculation of the Summation of Viscous Moduli

As we discussed in Section 2.3.3, we can calculate the residual strain by using the integration of stress history and the summation of viscous moduli, as given in Eq. 2.27. By extending this 1D equation to 2D case, we have

$$\mathbf{M}_\gamma \mathbf{u}_N(\infty) = \frac{1}{\sum_{i=1}^{n+1} c_i} \int_0^{t_p+t_h} \mathbf{F}(t)\mathrm{d}t. \tag{5.2}$$

where

$$\mathbf{M}_\gamma = \gamma_\lambda \mathbf{J}_\lambda + \gamma_\mu \mathbf{J}_\mu = \frac{\gamma}{(1+\gamma)(1-2\gamma)}\mathbf{J}_\lambda + \frac{1}{2(1+\gamma)}\mathbf{J}_\mu.$$

Note that the residual displacements $\mathbf{u}_N(\infty)$ and force history $\mathbf{F}(t)$ can be obtained from experimental measurements. Matrix $\mathbf{M}_\gamma$ can be prepared in advance and it only depends on the initial geometrical coordinates and Poisson's ratio γ. Therefore, Eq. 5.2 allows us to calculate the summation of viscous moduli $\sum_{i=1}^{n+1} c_i$ and this summation can be used as a constraint during the estimation of other parameters. Since the residual displacements $\mathbf{u}_N(\infty)$ was included in this calculation, the calculated value of $\sum_{i=1}^{n+1} c_i$ would guarantee a good reproduction of final-shape. Validation results will be presented in the next chapter.

5.2.3 Optimization of Force Differences Based on Iterative FE Simulation

After the first two steps as presented in the above, we have estimated one parameter γ and one constraint of $\sum_{i=1}^{n+1} c_i$. Considering the FE model with the parallel five-element model as an example which totally includes 6 physical parameters, we still have 4 independent parameters to be determined. This can be accomplished by minimizing the difference in rheological forces between simulation results and experimental measurements. The objective function of this optimization problem can be formulated as:

$$E(\boldsymbol{\Theta}) = \sum_{i=1}^{n} \|\mathbf{f}_i^{sim}(\boldsymbol{\Theta}) - \mathbf{f}_i^{exp}\|^2, \tag{5.3}$$

where vector $\boldsymbol{\Theta}$ consists of the parameters to be determined. Vector $\mathbf{f}_i^{exp}$ is the force measurements from experiments at the i-th sampling time and vector $\mathbf{f}_i^{sim}(\boldsymbol{\Theta})$ is the force response during simulation with parameter $\boldsymbol{\Theta}$. The threshold used to terminate the optimization is the tolerance on $E(\boldsymbol{\Theta})$ or the tolerance on $\boldsymbol{\Theta}$ less than 1×10^{-6}. In both optimizations presented in the first and third steps, the optimization toolbox of MATLAB and "Nonlinear Least Squares" method were employed to minimize the objective functions.

From Eq. 5.3, we can see that this optimization process involves iterative FE simulations, which is usually time consuming. Based on our experiences, this optimization process takes hours or days depending on the initial setting of the parameters. However, this simulation-based optimization is quite robust. As long as the simulation can be done, this optimization process can be performed as well and it does not require any special treatments of the physical models. We have tested this method with different physical models and it works well.

5.2.4 Optimization of Force Differences Based on Calculations

As presented in Section 2.3.2, the analytical expressions of stress in pushing and holding phases can be formulated as given in Eqs. 2.20 and 2.21. Extending these two equations from 1D to 2D case, we have

$$\mathbf{F}(t) = \sum_{i=1}^{n} c_i \big(1 - e^{-\frac{E_i}{c_i} t}\big) \mathbf{M}_\gamma \mathbf{v}_N^{Push}, \ (0 \le t \le t_p), \tag{5.4}$$

$$\mathbf{F}(t) = \sum_{i=1}^{n} c_i \big(1 - e^{-\frac{E_i}{c_i} t_p}\big) e^{-\frac{E_i}{c_i}(t - t_p)} \mathbf{M}_\gamma \mathbf{v}_N^{Push}, \ (t_p \le t \le t_p + t_h), \tag{5.5}$$

where vector $\mathbf{v}_N^{Push}$ consists of velocities of all nodal points during pushing phase. We assume that this is a constant vector which corresponding to the constant velocity p used in Eqs. 2.20 and 2.21. During the pushing phase, if we push the top surface of the object with a constant velocity and if this pushing velocity is not significantly big, this assumption can be satisfied. After we estimated the Poisson's ratio γ, vector $\mathbf{v}_N^{Push}$ can be easily obtained by performing the simulation in the pushing phase with all the other parameters taking arbitrary values since these parameters do not affect the deformation behaviors during pushing phase. Based on Eqs. 5.4 and 5.5, we are able to calculate the force responses during both pushing and holding phases and these calculated forces can be then used in Eq. 5.3 (instead of the simulated forces) to perform the force optimization. Since now there is no iterative FE simulations involved in this optimization process, we can obtain a optimal solution within only several seconds depending on the initial setting of parameters. However, this method only can be used in parallel physical models in which force expressions can be analytically derived. For other physical models, such as serial models, this method cannot be used and we have to perform simulation-based optimization instead, as proposed in the last subsection.

In some applications, if we only focus on reproducing force behaviors, the second step proposed in Section 5.2.2 can be ignored and all parameters except Poisson's ratio γ should be included in the force optimization (the third step). This will yield the best performance of force reproduction. But at the same time, we have to sacrifice some accuracy of the reproduction of final-shape. Detailed validation and discussions will be presented in the next chapter accompanying with various experimental results and comparisons.

5.2.5 Parameter Estimation of FE Model with Dual-Moduli Viscous Elements

In the above discussions, we supposed that only one set of parameters was used in the FE model. However, due to the linearity of the physically based models (*e.g.*, the parallel five-element model), it is difficult to reproduce both rheological forces and residual deformation simultaneously for most rheological objects. We have therefore introduced a dual-moduli viscous element into our FE formulation, as presented in Section 3.3. This dual-moduli viscous element has an ability to switch two parameters from one to the other during simulation. It can successfully capture both rheological deformation and force behaviors simultaneously. We have also proposed that the simulation time and losing contact moment can serve as a criterion to start the parameter switching.

Note that we usually switch the parameters at the moment when the operation is finished and the external instrument start to leave the object. During the operations (*e.g.*, pushing and holding), the deformation only depends on the Poisson's ratio γ. This suggests that we can use the estimated parameters by force optimization to reproduce both rheological force and deformation during operations. However, this set of parameters cannot guarantee accurate reproduction of residual deformation at the same time. We have therefore employed the dual-moduli viscous element to switch parameters when contact was lost. Since parameters c_i dominate the residual deformation as shown in Eq. 5.2, we only need to switch parameters c_i for capturing residual deformation. For example, we suppose the viscous moduli estimated by force optimization as c_i^{load} which will be used during operation (loading). We named another set of viscous moduli as c_i^{unload}, which will be used after operation (unloading). Our idea is to use those c_i^{unload} as unknown parameters to optimize the difference of final-shapes between experiments and simulation. Note that during this optimization the parameter c_i^{load} will be switched to c_i^{unload} automatically when the deformation starts to recover. The objective function of this optimization problem can be formulated as:

$$E(c_i^{unload}) = \sum_{i=1}^{m} \|\mathbf{x}_i^{sim}(c_i^{unload}) - \mathbf{x}_i^{exp}\|^2. \tag{5.6}$$

After having c_i^{unload}, we can easily determine the parameters used in the dual-moduli viscous elements by using the following equations:

$$\begin{aligned} c_i + \alpha_i &= c_i^{load}, \\ c_i - \alpha_i &= c_i^{unload}. \end{aligned} \tag{5.7}$$

Estimation results of FE model with dual-moduli viscous elements for objects made of Japanese sweets materials will be presented in the next chapter.

5.3 Concluding Remarks

In this chapter, the parameter estimation methods were presented for capturing both rheological forces and deformation behaviors simultaneously. At first, FE simulations were performed with different mesh resolutions and physical parameters to investigate the influence of these factors on the simulation behaviors. We found that a 4×4 triangular mesh is fine enough for the simple setup used in our parameter estimation procedures. We also found that only Poisson's ratio γ affect the held-shape and all the other parameters do not affect this shape at all. This allows us to estimated Poisson's ratio γ separately by minimizing the difference of held-shapes between simulation results and experimental measurements. We have therefore proposed a three-steps estimation method. Except estimating γ (the first step), we also calculate the summation of viscous coefficients $\sum_{i=1}^{n} c_i$ (the second step) by using the measured data of force and final-shape. This summation was then served as a constraint during estimating the other parameters (the third step) by minimizing the force differences. Depending on the force results obtained from FE simulation or straightforward calculation, the third step can be perform in two different ways. The simulation-based force optimization is robust and can be used in any model, but it is time-consuming since iterative FE simulations are involved. On the other hand, the calculation-based force optimization method is very efficient but only can be used in parallel physical models. In some applications, these two methods can be mixed to achieve the best estimation results. At last, the parameter estimation method for FE model with dual-moduli viscous elements was also presented based on the above-mentioned methods.

Chapter 6

Experiments and Validations

In the previous chapters, we have presented the FE models and parameter estimation methods for simulating rheological objects, especially focusing on the simultaneous reproductions of both rheological forces and deformation behaviors. In this chapter, we will demonstrate a series of experimental results and comparisons with simulation results for validating proposed FE models and parameter estimation methods.

6.1 Experimental Setup

As we mentioned before, a pushing-holding-releasing operation has been employed through out our discussions. Such kind of operation is frequently encountered in real applications and provides enough information to estimate the physical parameters included in the FE model. We have therefore performed a series of experiments on two different materials using this pushing-holding-releasing procedure. In order to perform such procedure, a testing device is necessary. At the same time, the force measurements should be recorded for the follow-up parameter estimation. Experimental setup used in our experiments is shown in Fig. 6.1. A motorized stage (KX1250C-L, SURUGA SEIKI Co.) was used to perform the pushing-holding-releasing operation. Force responses on the bottom surface of the object were measured by a tactile sensor (I-SCAN100L, NITTA Co.). In addition, several static images including the initial, deformed, and recovered shapes,

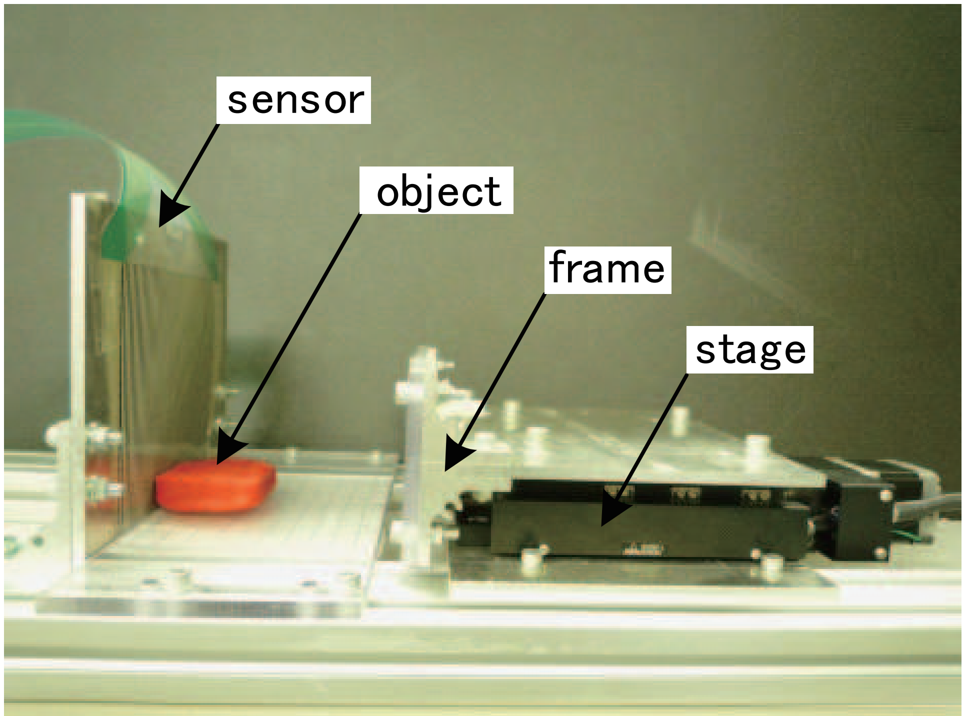

Figure 6.1: Experimental setup used for compressive tests.

were recorded by a camera (Canon Eos Kiss X2). These measurements were used to estimate the rheological properties of the object.

6.2 Compression Experiments

Two kinds of rheological materials were tested in our experiments, which are commercial available clay and Japanese sweets materials. These two materials show typical rheological behaviors under a loading-unloading operation.

6.2.1 Commercial Available Clay

The commercial clay is available in supermarket and is supposed to be played by kids (the one we used is supposed to be play by children over 3 years old, as shown in Fig. 6.2a). The clay is made of flour, salt, and water mixed with a special ratio. Several different colors are available and were used to distinguish

(a)

(b) (c) (d)

Figure 6.2: Commercial available clay product (a) and flat-squared objects used in experiments made of different colors: (b) red, (c) blue, and (d) yellow.

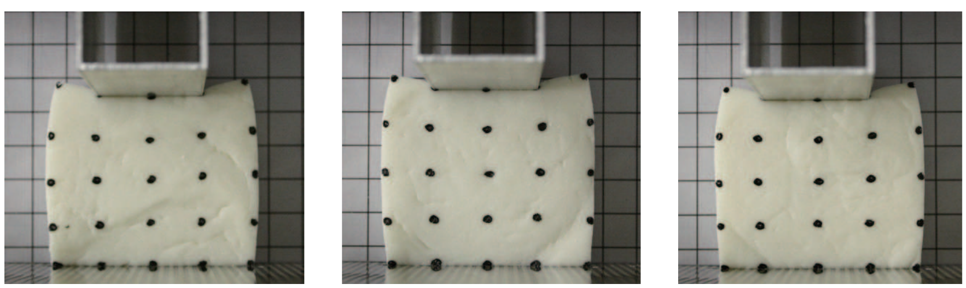

(a) v=0.1mm/s (b) v=0.2mm/s (c) v=0.5mm/s

Figure 6.3: Flat-squared objects made of white colored clay were compressed from the center part of top surfaces with different pushing velocities.

different pushing velocities in our experiments. Several flat-squared objects made by different colored clays were prepared for compressive testing, as shown in Fig. 6.2b, 6.2c, and 6.2d. Some markers were drawn on the object surfaces for conve-

Table 6.1: Detailed information of compression experiments with commercial clay

Object color	Object weight (g)	Object size W (mm)	H (mm)	T (mm)	Push velo. (mm/s)	Push disp. (mm)	Pushing time t_p (s)	t_h (s)
red-06	37.75	52.0	52.5	12.0		6	12.07	303.78
red-08	43.36	60.5	60.0	10.5	0.5	8	16.10	304.78
red-10	45.01	58.0	61.0	10.5		10	20.12	311.82
blue-06	43.98	60.5	59.0	10.0		6	30.17	311.83
blue-08	45.04	61.0	59.5	10.0	0.2	8	40.24	321.88
blue-10	43.80	60.5	59.5	10.0		10	49.29	342.00
yellow-06	46.19	59.0	59.0	11.0		6	58.34	502.94
yellow-08	44.72	59.5	59.0	10.0	0.1	8	79.46	500.94
yellow-10	45.14	57.5	56.5	11.5		10	98.58	609.57
white-05	46.43	58.0	57.0	12.0	0.5		16.09	369.16
white-02	46.23	60.0	60.5	10.5	0.2	8	40.24	400.34
white-01	44.08	59.5	58.0	10.0	0.1		79.46	601.52

nient capturing of internal deformation. During testing, the entire top surfaces of these objects were compressed downward with constant velocities. Different colors denote different velocities, *e.g.*, red color corresponding to the velocity of 0.5 mm/s, blue is 0.2 mm/s, and yellow is 0.1 mm/s. For each color, three objects were prepared and compressed with different displacements of 6 mm, 8 mm, and 10 mm, respectively. Measurements of these 9 objects were then used to estimate the physical parameters. In order to evaluate the estimated parameters, three white colored objects were prepared and compressed from the center part of top surfaces with different pushing velocities but same displacement, as shown in Fig. 6.3. Detailed information about these experiments with commercial clay was given in Table 6.1. Experimental trials with different pushing velocities (0.1, 0.2, and 0.5 mm/s) and different pushing displacements (6, 8, 10 mm) were performed to investigate how the pushing velocity and displacement affect the parameter estimation results.

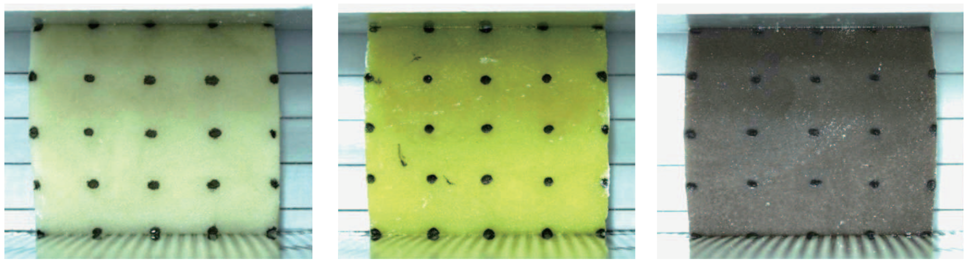

(a) material 1 (b) material 2 (c) material 3

Figure 6.4: Flat-squared objects made by different Japanese sweets materials.

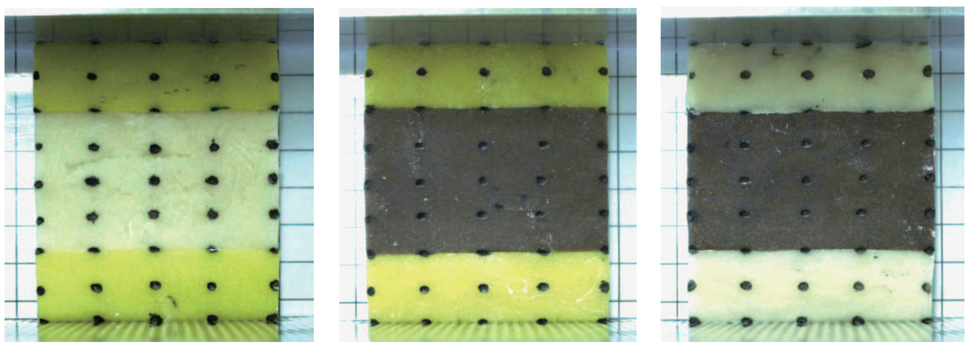

(a-1) material 1+2 (a-2) material 2+3 (a-3) material 1+3

(a) layered objects compressed from the top surface

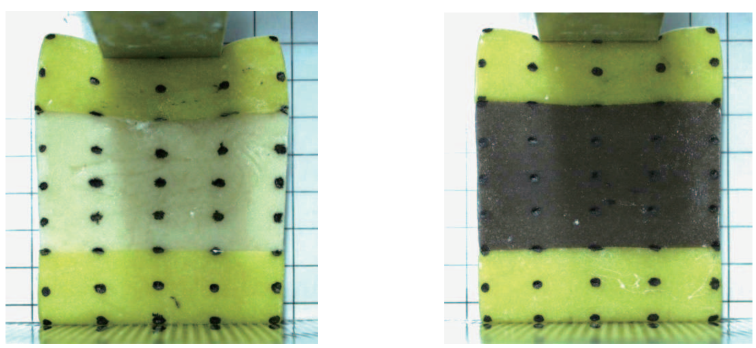

(b-1) material 1+2 (b-2) material 2+3

(b) layered objects compressed from the center of top surface

Figure 6.5: Non-uniform layered objects compressed over the entire or at the center of the top surfaces.

Table 6.2: Detailed information of compression experiments with Japanese sweets materials

Material	Object weight (g)	Object size W (mm)	H (mm)	T (mm)	Push type	Push velo. (mm/s)	Push disp. (mm)	Time t_p (s)	t_h (s)
Mat. 1	52.43	58.0	59.5	12.0				28.87	182.06
Mat. 2	32.97	50.0	50.0	11.0	top	0.2	6	29.68	181.26
Mat. 3	34.99	50.0	50.0	11.0				29.97	181.46
Mat. 1+2	66.99	60.0	80.0	11.0				49.29	181.76
Mat. 2+3	69.12	60.0	80.0	11.0	top	0.2	10	49.49	181.47
Mat. 1+3	68.52	60.0	80.0	11.0				49.49	181.97
Mat. 1+2	66.99	60.0	80.0	11.0	center	0.2	10	49.69	181.86
Mat. 2+3	69.12	60.0	80.0	11.0			8	39.13	182.07

6.2.2 Japanese Sweets Materials

Three kinds of Japanese sweets materials were provided by OIMATU, a sweets company in Kyoto. Each was made of flour, water, and bean powder mixed at specific ratios. Three flat-squared objects, each composed of one material, were prepared for the compression tests, as shown in Fig. 6.4. The entire top surfaces of these objects were compressed at a constant velocity of 0.2 mm/s and with a displacement of 6 mm. Several markers were drawn on the surfaces and force responses and deformed images were recorded. These measurements were used to estimate the rheological parameters of these sweets materials. In addition, to validate the FE model and the estimated parameters, several non-uniform layered objects(each made of three layers with two alternating materials) were compressed over their entire or at the center of their top surfaces, as shown in 6.5a and 6.5b, respectively. Detailed experimental information using Japanese sweets materials is given in Table 6.2. Note that the pushing time t_p was quite different between uniform object (about 30 s) and layered objects (about 40 or 50 s) because they were compressed with the same velocity (0.2 mm/s) but different displacements (6, 8, and 10 mm). The holding time t_h, however, was quite similar (around 3 minutes, as shown in the last column of Table 6.2) among these experimental trials. During the experiments, we manually controlled the time t_h and concluded that 3 minutes was sufficient to obtain adequate information on force relaxation behaviors. In addition, the compressing displacements were chosen to be 6, 8, and 10 mm (see the eighth column of Table 6.2) based on the small-deformation assumption of generalized Hooke's law. We used the same compressing displacement (10 mm) for the three trials (middle three rows of Table 6.2) with layered objects compressed over their entire top surfaces to investigate the performance of our model with different material combinations. Additionally, two further trials (the last two rows of Table 6.2) with layered objects compressed at the centers of their top surfaces were performed to validate our FE model and estimated parameters with different operations and different compressive displacements (8 and 10 mm).

6.3 Parameter Estimation Results

Generally, the material property of an object will not differ even though the object is subjected to different operations or it has different shape or size. This feature allows us to use regular shaped objects with simple pushing operations to estimate their physical parameters. Then, the estimated parameters should be able to simulate arbitrary shaped objects with any operations. In our experiments, we used flat-squared objects pushed on the entire top surfaces with constant velocities to estimate the parameters. As an example of our step-by-step estimation method, we show the case of the object made by red colored clay pushed with a displacement of 8 mm, denoted by red-08 in Table 6.1. A parallel five-element model was employed to model the rheological behaviors of this object. According to the discussions presented in section 5.1, parameter c_3 in the parallel five-element model was mainly responsible for eliminating the vibration from the simulation. Based on our experience, a small value of c_3 comparing with c_1 and c_2 is enough to remove the vibration and without significant effect on simulation results of force and deformation. Usually, parameter c_1 and c_2 of real materials have a magnitude about 10^5 or 10^6 Pa·s. We have therefore set a value of 100 Pa·s to parameter c_3 in advance. Now, we have 5 unknown parameters to

Table 6.3: Arbitrary values of E_1, E_2, c_1, c_2, and c_3 for estimating γ

Case no.	E_1 (Pa)	E_2 (Pa)	c_1 (Pa·s)	c_2 (Pa·s)	c_3 (Pa·s)
trial 1	5×10^2	1×10^3	2×10^3	3×10^3	1×10^2
trial 2	5×10^3	1×10^4	2×10^4	3×10^4	1×10^2
trial 3	5×10^4	1×10^5	2×10^5	3×10^5	1×10^2

Table 6.4: Estimation results for Poisson's ratio γ

Case number	Initial value x_0	Final value x^*	$E(\gamma)$ ($\times 10^{-6}$ m^2)	Iteration count	Cost (hr)
trial 1	0.15	0.29023634	3.7546	4	0.26
	0.25	0.29023308	3.7546	3	0.20
	0.35	0.29023665	3.7546	4	0.25
trial 2	0.15	0.29024458	3.7546	4	0.37
	0.25	0.29022518	3.7546	3	0.32
	0.35	0.29021075	3.7546	4	0.42
trial 3	0.15	0.29023707	3.7546	4	1.55
	0.25	0.29023282	3.7546	3	1.25
	0.35	0.29023569	3.7546	4	1.63

be estimated, *i.e.*, Poisson's ratio γ, Young's moduli E_1, E_2, and viscous moduli c_1, and c_2.

6.3.1 Estimation of Poisson's Ratio γ

In the first step, we estimated the Poisson's ratio γ by minimizing the differences of held-shapes. Since other parameters do not affect held-shape, we therefore assigned some arbitrary values to the other parameters. Three trials were performed and the arbitrary values for other parameters are listed Table 6.3. The optimization for minimizing the differences of held-shapes were then performed, as discussed in section 5.2.1. Table 6.4 shows the estimated Poisson's ratios γ at different cases and different initial values. We find that parameter γ quickly (only 3 or 4 iterations) converge to a global minimum of about $\gamma = 0.2902$. This value will be used in the following calculation of $\sum_{i=1}^{3} c_i$ and force optimization.

Table 6.5: Estimation results of E_1, E_2, and c_1 using simulation-based optimization

Trial number	Parameter	Initial value x_0	Final value x^*	$F(\mathbf{\Theta})$ (N^2)	Iteration count	Cost (hr.)
trial 1	E_1 (Pa)	4×10^4	2.4722×10^4	90.519	36	4.47
	E_2 (Pa)	6×10^4	5.0771×10^4			
	c_1 (Pa·s)	8×10^6	8.1142×10^6			
trial 2	E_1 (Pa)	8×10^4	5.5790×10^4	27.383	43	5.77
	E_2 (Pa)	6×10^4	3.8065×10^4			
	c_1 (Pa·s)	4×10^6	4.5349×10^5			
trial 3	E_1 (Pa)	3×10^4	3.7607×10^4	24.536	33	4.79
	E_2 (Pa)	8×10^4	7.6996×10^4			
	c_1 (Pa·s)	9×10^6	9.1985×10^6			

6.3.2 Calculation of Summation $\sum_{i=1}^{3} c_i$

Using Eq. 5.2, we can easily calculate the value of summation $\sum_{i=1}^{3} c_i$ based on experimental data on force and residual deformation. In this case, we found that $\sum_{i=1}^{3} c_i = 9.6961 \times 10^6$Pa·s. Note that the value of $\sum_{i=1}^{3} c_i$ can guarantee a good reproduction of final deformed shape since the residual deformation has been considered during the calculation.

6.3.3 Estimation of Other Parameters

After estimating Poisson's ratio γ and the value of $\sum_{i=1}^{3} c_i$, the other parameters can be then estimated by minimizing the difference of rheological forces with a constraint of summation $\sum_{i=1}^{3} c_i$. However, depending on the way obtaining virtual force data, the estimation of other parameters can be divided into two categories: simulation- and calculation-based methods, as discussed in Section 5.2.3 and 5.2.4 respectively.

6.3.3.1 Estimation Results of Simulation-Based Optimization

In simulation-based optimization, the FE simulations were iterated with updated parameters until the differences between simulation results and experiment mea-

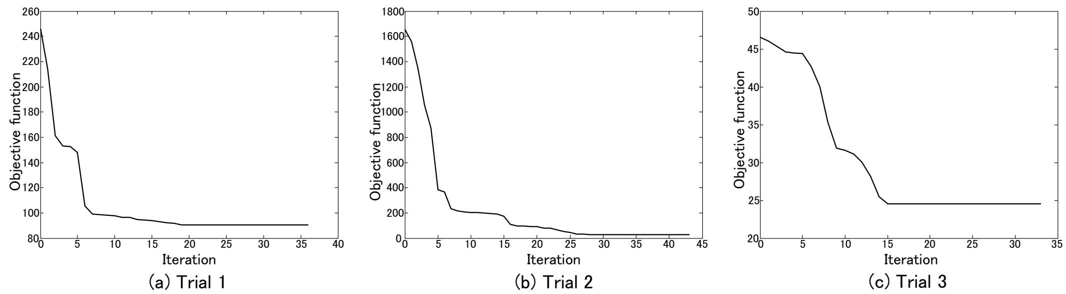

Figure 6.6: Optimization curves of three trials given in Table 6.5.

surements becomes minimal. Three optimization trials were performed with different initial conditions. The estimation results associated with computation costs were given in Table 6.5. We can see that the optimal solutions are quite sensitive with the initial setting of parameter values. The optimization curves (solution evolution) of these three trials were shown in Fig. 6.6. We are not able to obtain a global solutions in this optimization problem. We only can pick one local minimum by comparing the values of objective function $F(\boldsymbol{\Theta})$. In this case, we pick the third trial as a solution. We also can see that the simulation-based optimization took several hours to reach a local minimum even with a very close setting of initial values (the third trial). Usually, it is quite hard to find the close settings of initial values and we may have to perform a plenty of trials to finally reach an acceptable solution. This method is time-consuming but quite robust and widely applicable. It can be used in any model to estimate the parameters as long as the simulation can be done.

6.3.3.2 Estimation Results of Calculation-Based Optimization

In calculation-based optimization, the force results were calculated using Eqs. 5.4 and 5.5 instead of running FE simulations. The calculated force results were then used in optimization to minimize the force differences. Totally, five optimization trials were performed for this case. The fist three trials used the same initial conditions with simulation-based optimization (Table 6.5) for the convenience of comparison. The last two trials were with other arbitrary initial values. The estimation results associated with computation costs are given in Table 6.6. We can see that all trials converged to the same solution and it seems like we can

Table 6.6: Estimation results of E_1, E_2, and c_1 using calculation-based optimization

Trial number	Parameter	Initial value x_0	Final value x^*	$F(\mathbf{\Theta})$ (N^2)	Iteration count	Cost (s)
	E_1 (Pa)	4×10^4	3.7730×10^4			
trial 1	E_2 (Pa)	6×10^4	8.0916×10^4	24.514	15	0.17
	c_1 (Pa·s)	8×10^6	9.2022×10^6			
	E_1 (Pa)	8×10^4	8.0914×10^4			
trial 2	E_2 (Pa)	6×10^4	3.7730×10^4	24.514	20	0.20
	c_1 (Pa·s)	4×10^6	4.9375×10^5			
	E_1 (Pa)	3×10^4	3.7730×10^4			
trial 3	E_2 (Pa)	8×10^4	8.0917×10^4	24.514	14	0.19
	c_1 (Pa·s)	9×10^6	9.2023×10^6			
	E_1 (Pa)	2×10^3	8.0952×10^4			
trial 4	E_2 (Pa)	3×10^4	3.7731×10^4	24.514	23	0.23
	c_1 (Pa·s)	4×10^5	4.9381×10^5			
	E_1 (Pa)	6×10^5	8.0917×10^4			
trial 5	E_2 (Pa)	4×10^5	3.7730×10^4	24.514	16	0.18
	c_1 (Pa·s)	2×10^5	4.9375×10^5			

find the global minimum by using this method. The optimization curves of the first three trials were shown in Fig. 6.7. Comparing Figs. 6.6 and 6.7, we found that the values of objective function from both simulation- and calculation-based optimization were start from the same value (because the initial parameter setting are the same) but converged to the different minimal values in the end of optimization. Figure 6.6 shows that the curves in simulation-based optimization have more ladder-shaped regions which make the optimization easy to be trapped into a local minimum. On the other hand, the curves from calculation-based optimization are appears more smooth. Smaller tolerance used to terminate the optimization can yield better solutions, especially for simulation-based optimization method. However, it will take much more computation time. From the estimation results given in Tables 6.5 and 6.6, we can see that both optimization methods converge to the very similar solutions, as shown in trial 3 of Table 6.5

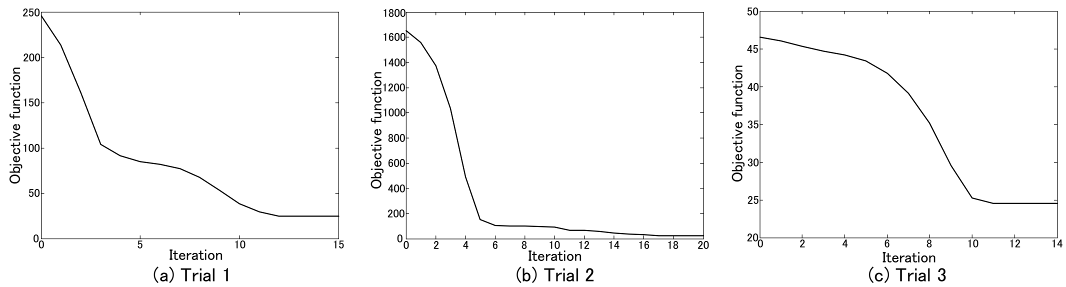

Figure 6.7: Optimization curves of three trials given in Table 6.6.

and all trials of Table 6.6. Note that the first and second layer Maxwell element are exchangeable in a parallel five-element model. Therefore, the values of E_1 and E_2, c_1 and c_2 are also exchangeable, which makes the solutions of trials 1, 3, and trials 2, 4, 5 of Table 6.6 actually very similar. In addition, the computation costs in the calculation-based optimization were extremely short (less than 1 second in all trials listed in Table 6.6) since there is no FE simulations involved during optimization. However, the disadvantage is that this method only can be used in parallel models which provide the analytical expressions of forces.

6.3.4 Estimation without the Constraint of $\sum_{i=1}^{3} c_i$

The value of $\sum_{i=1}^{3} c_i$ calculated separately before force optimization will guarantee a good reproduction of final deformed shape. In the last subsection, this value was used as a constraint during the force optimization. Since this constraint makes the optimization problem losing one independent variable, the result of force optimization will be suffered. We have to compromise the accuracy between the reproductions of final-shapes and force behaviors. Note that the held-shape is affected only by Poisson's ratio γ. Therefore, we do not have to do the same compromise for held-shapes. In some situations, such as deformable objects handled by robotic hand, we may care about the force response and the held-shape much more than the final-shape. In such situations, we can just ignore the calculation of $\sum_{i=1}^{3} c_i$ during the parameter estimation procedure. Instead, we use all four parameters: E_1, E_2, c_1, and c_2 as unknown variables to perform the force optimization. This should give us better results of force reproduction.

Table 6.7: Estimation results of E_1, E_2, c_1 and c_2 using simulation-based optimization

Trial number	Parameter	Initial value x_0	Final value x^*	$F(\boldsymbol{\Theta})$ (N^2)	Iteration count	Cost (hr.)
trial 1	E_1 (Pa)	4×10^4	3.1736×10^4	4.0351	24	24.9
	E_2 (Pa)	7×10^4	7.1867×10^4			
	c_1 (Pa·s)	9×10^6	1.3298×10^7			
	c_2 (Pa·s)	6×10^5	6.9787×10^5			
trial 2	E_1 (Pa)	3×10^4	3.1735×10^4	4.0351	39	39.8
	E_2 (Pa)	8×10^4	7.1884×10^4			
	c_1 (Pa·s)	9×10^6	1.3298×10^7			
	c_2 (Pa·s)	7×10^5	6.9787×10^5			
trial 3	E_1 (Pa)	2×10^3	7.1851×10^4	4.0351	26	26.7
	E_2 (Pa)	3×10^4	3.1732×10^4			
	c_1 (Pa·s)	4×10^5	6.9809×10^5			
	c_2 (Pa·s)	5×10^6	1.3300×10^7			

In the following subsections, the estimation results of these four parameters using both simulation- and calculation-based methods will be presented. Note that $\gamma = 0.2902$ and $c_3 = 100$Pa·s are still used in the following discussions.

6.3.4.1 Estimation Results with Simulation-Based Optimization

Three optimization trials with different initial conditions were performed and the estimation results were given in Table 6.7. The optimization curves are shown in

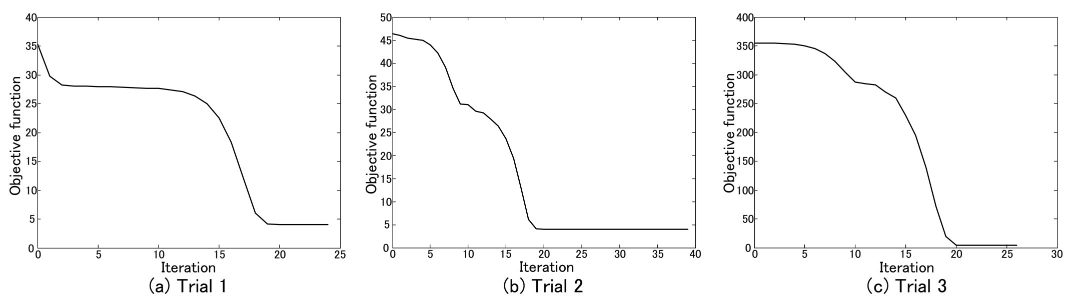

Figure 6.8: Optimization curves of three trials given in Table 6.7.

Table 6.8: Estimation results of E_1, E_2, c_1 and c_2 using calculation-based optimization

Trial number	Parameter	Initial value x_0	Final value x^*	$F(\mathbf{\Theta})$ (N^2)	Iteration count	Cost (s)
trial 1	E_1 (Pa)	4×10^4	3.1752×10^4	4.0766	25	0.3108
	E_2 (Pa)	7×10^4	7.2145×10^4			
	c_1 (Pa·s)	9×10^6	1.3291×10^7			
	c_2 (Pa·s)	6×10^5	6.9733×10^5			
trial 2	E_1 (Pa)	3×10^4	3.1753×10^4	4.0766	24	0.3205
	E_2 (Pa)	8×10^4	7.2147×10^4			
	c_1 (Pa·s)	9×10^6	1.3291×10^7			
	c_2 (Pa·s)	7×10^5	6.9731×10^5			
trial 3	E_1 (Pa)	2×10^3	7.2131×10^4	4.0766	26	0.3554
	E_2 (Pa)	3×10^4	3.1750×10^4			
	c_1 (Pa·s)	4×10^5	6.9745×10^5			
	c_2 (Pa·s)	5×10^6	1.3292×10^7			

Fig. 6.8. In this case, we are able to find a global minimum and the solution is much better than the ones shown in Tables 6.5 and 6.6 (by comparing the values of objective function $F(\mathbf{\Theta})$).

6.3.4.2 Estimation Results with Calculation-Based Optimization

Estimation results using calculation-based optimization method were given in Table 6.8 and optimization curves are shown in Fig. 6.9. Comparing with

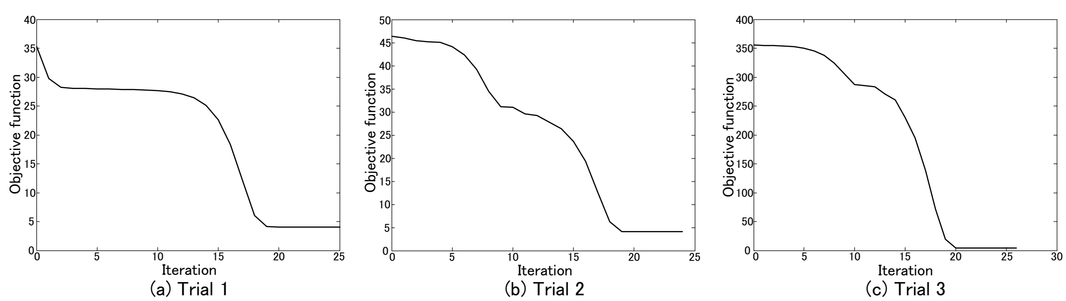

Figure 6.9: Optimization curves of three trials given in Table 6.8.

Table 6.9: Estimation results with the constraint of $\sum_{i=1}^{3} c_i$ for all objects made by clay materials

Trial name	γ	E_1 (Pa)	E_2 (Pa)	c_1 (Pa·s)	$\sum_{i=1}^{3} c_i$ (Pa·s)	$E(\mathbf{\Theta})$ (N^2)
red-06	0.2672	3.1706×10^4	6.4702×10^4	7.4606×10^6	7.9035×10^6	6.3658
red-08	0.2902	3.7730×10^4	8.0916×10^4	9.2022×10^6	9.6961×10^6	24.514
red-10	0.2367	2.7237×10^4	7.5406×10^4	5.4256×10^6	5.9092×10^6	31.5945
blue-06	0.2537	2.0182×10^4	4.4243×10^4	4.4555×10^6	4.9014×10^6	3.1863
blue-08	0.2292	2.6344×10^4	6.4348×10^4	6.9430×10^6	7.6884×10^6	5.5283
blue-10	0.2602	3.0593×10^4	7.5570×10^4	5.7866×10^6	6.5596×10^6	50.4884
yellow-06	0.2593	2.0820×10^4	3.9699×10^4	7.9776×10^6	8.5615×10^6	2.4562
yellow-08	0.2479	2.9216×10^4	4.6662×10^4	1.1663×10^7	1.2385×10^7	28.5041
yellow-10	0.2494	2.1480×10^4	4.1776×10^4	8.0970×10^6	8.9095×10^6	32.8334
average	0.2549	2.7256×10^4	5.9258×10^4	7.4457×10^6	8.0571×10^6	—

simulation-based method, very similar results were obtained using calculation-based optimization but the computation costs are significantly reduced. Figures 6.8 and 6.9 also show very similar curves of solution evolution.

6.3.5 Estimation Results for All Objects Made of Clay Materials

By following the same estimation procedures presented above, we can estimate the physical parameters for all experimental objects made of clay materials. Note that $c_3 = 100$Pa·s and the calculation-based optimization method were used in all trials. Estimation results for clay objects with and without the constraint of $\sum_{i=1}^{3} c_i$ are given in Tables 6.9 and 6.10, respectively. Note that the estimated parameters listed in Table 6.9 yield good reproductions of final-shapes while parameters in Table 6.10 result in good approximation of force responses. We can see that both sets of parameters of some clay objects are quite close and the optimal values of objective function (given in the last column of both tables) are also not very different. This means that it is possible for those objects (*e.g.*, red-06, blue-06) to use one set of parameters to accurately reproduce both deformation and force behaviors. However for most objects, the differences of parameters and

Table 6.10: Estimation results without the constraint of $\sum_{i=1}^{3} c_i$ for all objects made by clay materials

Trial name	γ	E_1 (Pa)	E_2 (Pa)	c_1 (Pa·s)	c_2 (Pa·s)	$E(\mathbf{\Theta})$ (N^2)
red-06	0.2672	2.8650×10^4	6.0364×10^4	8.8323×10^6	5.4820×10^5	3.1418
red-08	0.2902	3.1753×10^4	7.2147×10^4	1.3291×10^7	6.9731×10^5	4.0766
red-10	0.2367	2.1954×10^4	6.7528×10^4	8.4719×10^6	6.8294×10^5	4.2865
blue-06	0.2537	1.6582×10^4	4.2801×10^4	6.0304×10^6	6.1032×10^5	0.3573
blue-08	0.2292	2.2164×10^4	6.0319×10^4	8.7880×10^6	9.6051×10^5	1.2468
blue-10	0.2602	2.2424×10^4	7.1494×10^4	9.3098×10^6	1.2391×10^6	1.8716
yellow-06	0.2593	1.7273×10^4	3.6229×10^4	1.0636×10^7	8.4945×10^5	0.2495
yellow-08	0.2479	2.1804×10^4	4.2930×10^4	1.9429×10^7	1.3657×10^6	0.6176
yellow-10	0.2494	1.5206×10^4	4.1475×10^4	1.4602×10^7	1.4882×10^6	0.5583

objective function values are significant, especially the values of $\sum_{i=1}^{3} c_i$ which dominate both final-shape and force amplitude as discussed in Section 2.4. For these objects, one set of parameters is not enough to reproduce both rheological deformation and force simultaneously.

6.3.6 Estimation Results for Objects Made by Japanese Sweets Materials

The same parameter estimation procedures were also performed for objects made by three kinds of Japanese sweets materials. Experimental information was given in Table 6.2. Estimation results for these three objects with and without the constraint of $\sum_{i=1}^{3} c_i$ are given in Tables 6.11 and 6.12, respectively. Comparing with results of clay materials, two sets of parameters of sweets objects are very different with each other. The values of $\sum_{i=1}^{3} c_i$ from Table 6.12 (not given directly but can be easily calculated) are around 10 times larger than those given in Table 6.11. The optimal values of objective function are even hundreds times different. This means it is impossible for objects made by sweets materials to accurately reproduce both rheological deformation and forces simultaneously. This problem comes from the physical model (*e.g.*, parallel five-element model) itself and it cannot be resolved by adding more basic elements to the physical model or

Table 6.11: Estimation results with the constraint of $\sum_{i=1}^{3} c_i$ for three objects made by Japanese sweets materials

Trial name	γ	E_1 (Pa)	E_2 (Pa)	c_1 (Pa·s)	$\sum_{i=1}^{3} c_i$ (Pa·s)	$E(\mathbf{\Theta})$ (N^2)
material 1	0.3746	8.1002×10^3	9.7210×10^3	1.0804×10^6	2.3761×10^6	326.01
material 2	0.3353	1.0662×10^4	3.7979×10^3	1.2423×10^6	1.6849×10^6	186.48
material 3	0.3267	5.8791×10^3	7.3308×10^3	8.6015×10^5	1.9319×10^6	76.41

Table 6.12: Estimation results without the constraint of $\sum_{i=1}^{3} c_i$ for three objects made by Japanese sweets materials

Trial name	γ	E_1 (Pa)	E_2 (Pa)	c_1 (Pa·s)	c_2 (Pa·s)	$E(\mathbf{\Theta})$ (N^2)
material 1	0.3746	1.3468×10^4	2.4695×10^4	2.9631×10^7	7.2381×10^4	0.9152
material 2	0.3353	1.0553×10^4	3.7276×10^4	1.3213×10^7	1.1593×10^5	0.8385
material 3	0.3267	9.1565×10^3	5.0802×10^4	8.1809×10^6	1.3427×10^5	0.7208

changing the configuration of the model. Further validation of this phenomenon with simulation results comparing with experimental ones will be presented in the later of this chapter.

6.3.7 Estimation Results of FE Model with Dual-Moduli Viscous Elements

For some materials, such as clay materials discussed above, one set of parameters seems enough to capture both rheological forces and deformation behaviors. However for most rheological objects, such as Japanese sweets products, it is impossible to use only one set of parameters to cover both force and deformation simultaneously. We have therefore introduced FE model with dual-moduli viscous elements (section 3.3) to solve this problem. Here, we suppose that the FE model was formulated using parallel five-element model with two dual-moduli viscous elements (Fig. 2.9b) and we preassigned a value of 100 Pa·s to parameter c_3. By following the estimation procedure presented in section 5.2.5, we can determine those parameters for FE model with dual-moduli viscous elements and

Table 6.13: Estimation results of FE model with dual-moduli viscous elements for simulating the objects made of Japanese sweets materials

Trial name	E_1 (Pa)	E_2 (Pa)	c_1 (Pa·s)	c_2 (Pa·s)	α_1 (Pa·s)	α_2 (Pa·s)
mat.1	1.3468×10^4	2.4695×10^4	1.4820×10^7	5.3855×10^4	1.4811×10^7	1.8527×10^4
mat.2	1.0553×10^4	3.7276×10^4	6.6096×10^6	7.8271×10^4	6.6034×10^6	3.7659×10^4
mat.3	9.1565×10^3	5.0802×10^4	4.0958×10^6	8.2198×10^4	4.0851×10^6	5.2072×10^4

listed them in Table 6.13. Note that the Poisson's ratios are not listed in this table and they take the same values as given in Table 6.12.

6.4 Validation Results

In the above sections, the experimental information was introduced and the physical parameters for clay and Japanese sweets materials were estimated using different methods. In this section, the simulation results using the estimated parameters will be compared with experimental measurements to show the performance of our FE model and parameter estimation methods. Note that the physical parameters were estimated by using measured data of the uniform objects (for both clay and sweets materials) with compressing operations from the entire top surfaces. The measurements of uniform objects compressed from the center-top surfaces (white colored clay objects) and non-uniform sweets objects compressed from top and center-top surfaces were used to evaluate the estimated parameters.

6.4.1 Validation Results of Objects Made by Commercial Clay Materials

At first, the estimated parameters listed in Tables 6.9 and 6.10 were used to simulate the corresponding clay objects to show performance of our optimization-based estimation methods and also to demonstrate the difference between these two methods with or without the constraint of $\sum_{i=1}^{3} c_i$. Simulation results compared with experimental measurements for three trials (denote by red-08, blue-06, and yellow-08 in Tables 6.9 and 6.10) were shown in Figs. 6.10, 6.11, and 6.12,

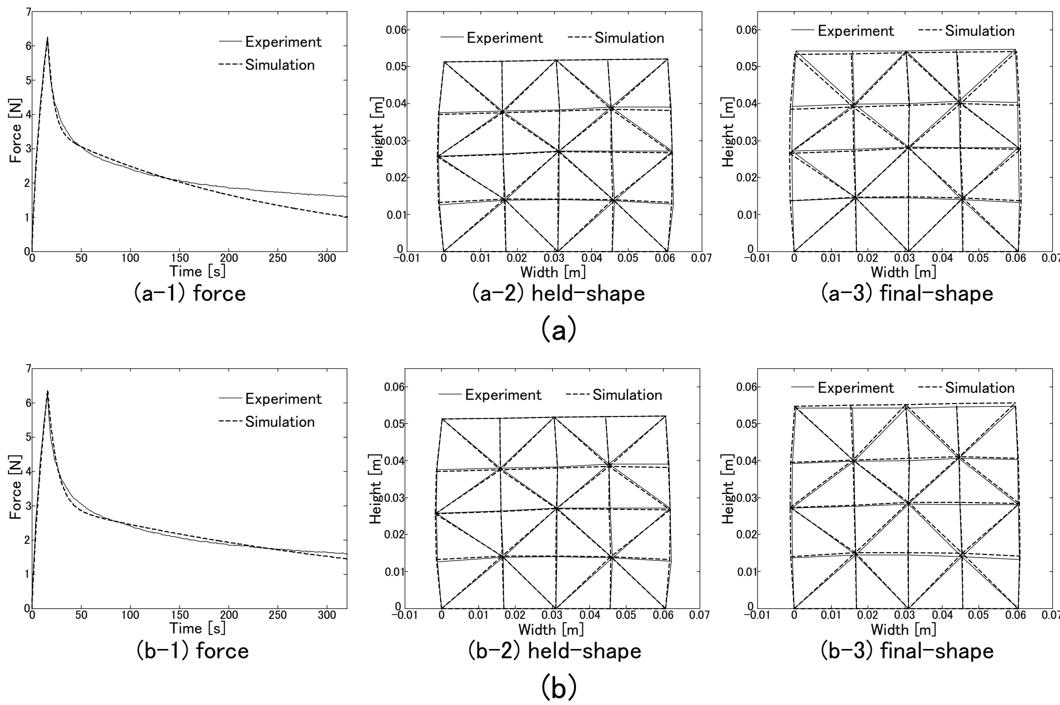

Figure 6.10: Validation results for object red-08 (a) with and (b) without the constraint of $\sum_{i=1}^{3} c_i$.

respectively. From these figures we can see that estimated parameters with the constraint of $\sum_{i=1}^{3} c_i$ yield better results of final-shapes. On the other hand, estimated parameters without this constraint result in better results in force approximation. This is coincide with our theoretical analysis, *i.e.*, the summation $\sum_{i=1}^{3} c_i$ dominates the residual deformation. We can also see that the estimated parameters with the constraint always under-approximated the force amplitudes, especially in the end of the holding phases. On the other hand, the estimated parameters without the constraint always over-approximated the final-shapes, especially for object yellow-08 shown in Fig. 6.12. It can be explained that accurate approximation of final-shape requires relative smaller values of $\sum_{i=1}^{3} c_i$ while accurate approximation of force behaviors requires relative larger values. If we look at Tables 6.9 and 6.10, we find that the values of $\sum_{i=1}^{3} c_i$ in Table 6.10 are always larger than those in Table 6.9. The object yellow-08 has the largest difference (about 1.8 times) between two sets of parameters among these three

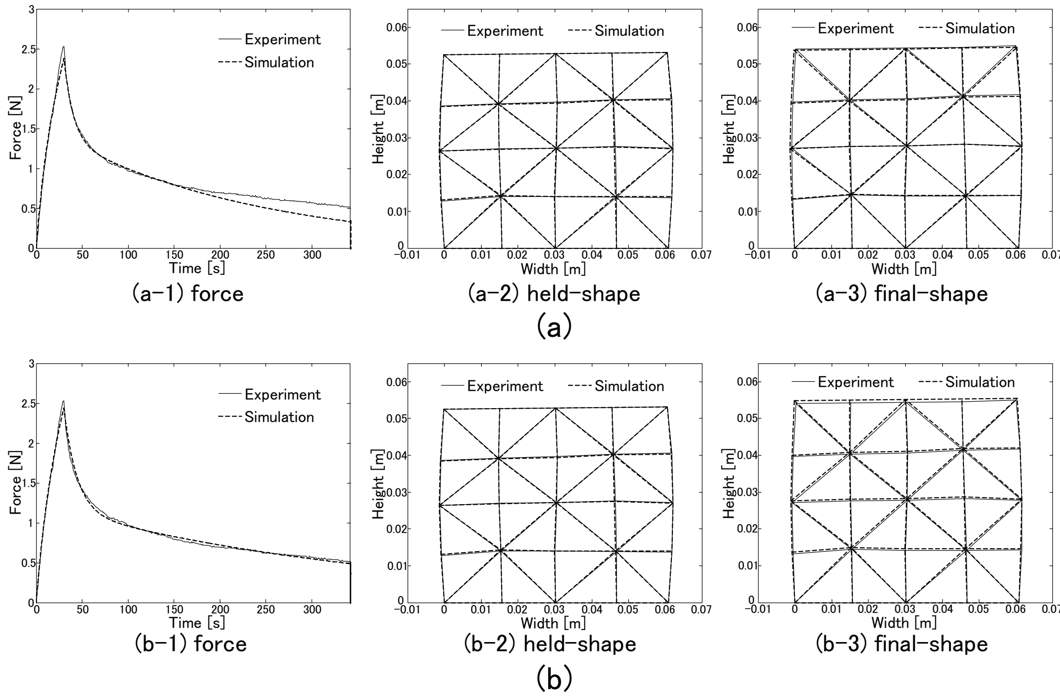

Figure 6.11: Validation results for object blue-06 (a) with and (b) without the constraint of $\sum_{i=1}^{3} c_i$.

objects. This is why the differences in both force and deformation behaviors shown in Fig. 6.12 are larger than those in Figs. 6.10 and 6.11. However, we can obtain good reproductions of both rheological forces and deformation behaviors for objects red-08 and blue-06 within a relative short time (within 200 seconds) using the estimated parameters with the constraint of $\sum_{i=1}^{3} c_i$. Actually in most applications, the holding time may not be very long. In such cases, the parameters listed in Table 6.9 are good enough to reproduce both rheological forces and deformation behaviors simultaneously.

The simulation results shown in Figs. 6.10, 6.11, and 6.12 were performed using their own estimated parameters. In other words, these validation results only showed how well the force and shape optimizations were performed. These validation results are thus quite insufficient. We therefore conducted three other experiments with objects made by white colored clay materials. In order to investigate how the estimated parameters can handle different operations, we compressed these three objects from the center area of the top surfaces instead of

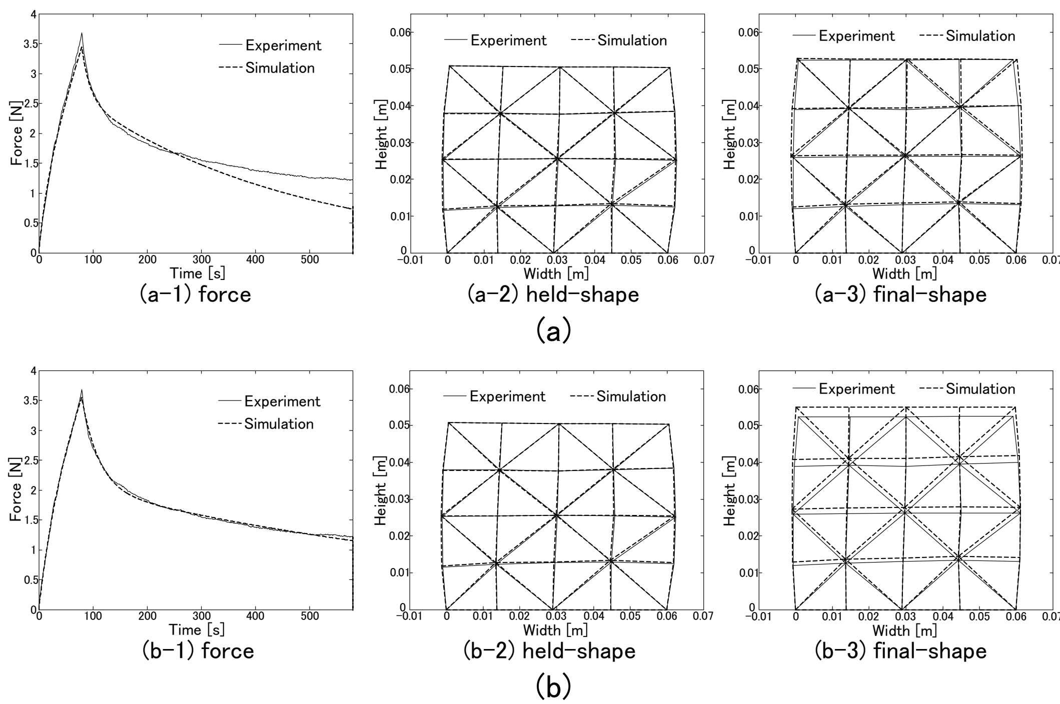

Figure 6.12: Validation results for object yellow-08 (a) with and (b) without the constraint of $\sum_{i=1}^{3} c_i$.

the entire top surfaces and also with different compressing velocities of 0.5 m/s, 0.2 m/s, and 0.1 m/s, respectively. Detailed experimental information of these three trials can be found in Table 6.1. Note that different colored clay materials actually denote different materials and they may have different properties. However, since they were sold in the same pack and manufactured at the same time, the difference in properties among them was supposed to be negligible. Therefore, the average values of estimated parameters listed in the last row of Table 6.9 were used to reproduce the rheological behaviors of these three objects. The simulation results compared with experimental measurements were shown in Fig. 6.13. Because the deformation behaviors are more complicated (especially in the contact corners) than compressing from the entire top surfaces, we have used a 16×16 triangular mesh instead of a 4×4 mesh to simulate the behaviors of these white colored objects. In order to clearly show the deformation comparisons between simulation and experiments, only 8×8 lattice mesh was shown in Fig.

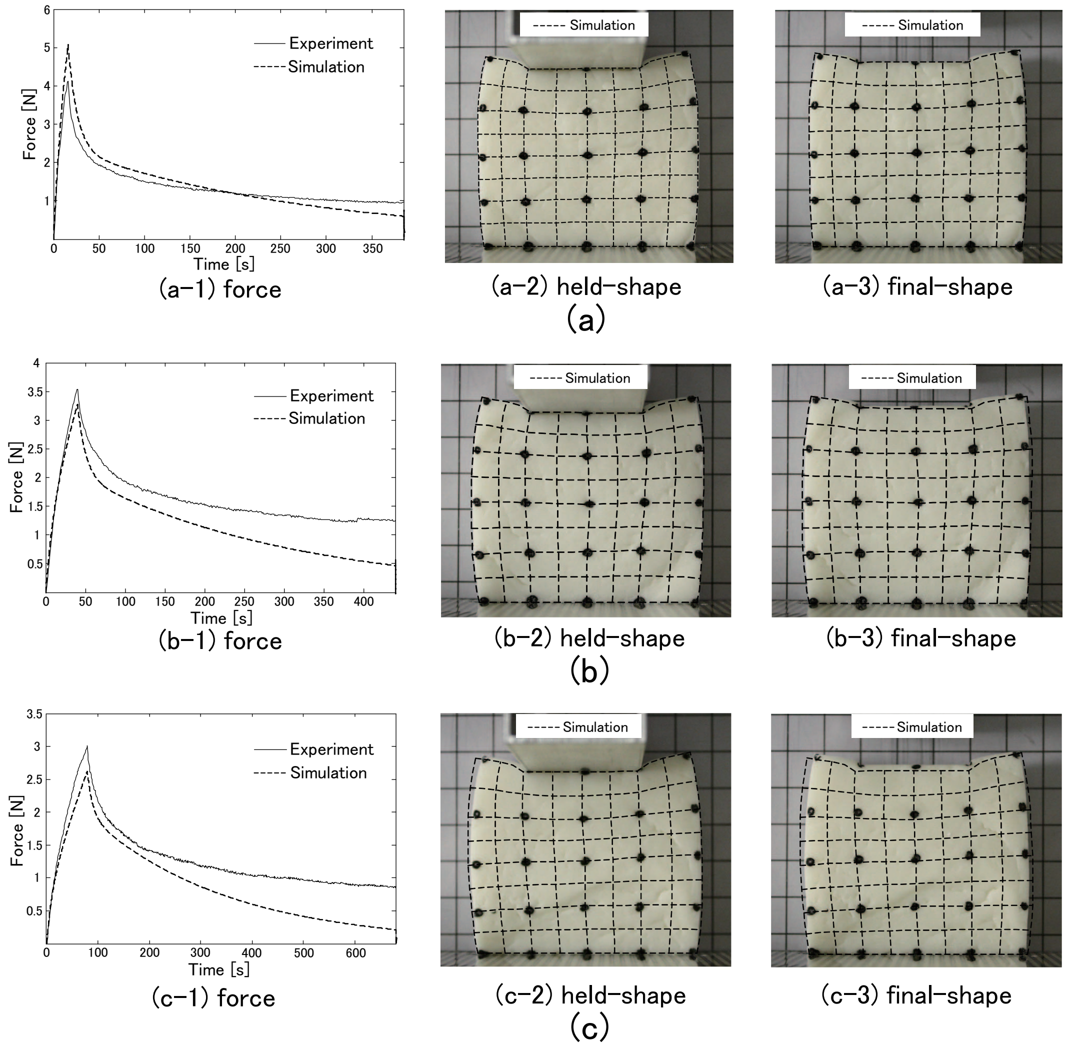

Figure 6.13: Validation results for white colored objects with a compressing velocity of (a) 0.5 m/s, (b) 0.2 m/s, and (c) 0.1 m/s.

6.13. We find that both held-shapes and final-shapes are pretty well matched between simulation results and experimental measurements and we can achieve good reproductions of force behaviors in a short term (within about 200 seconds). We can therefore say that we can obtain acceptable reproduction results of both rheological force and deformation for clay objects by using our FE model and the estimated parameters listed in Table 6.9.

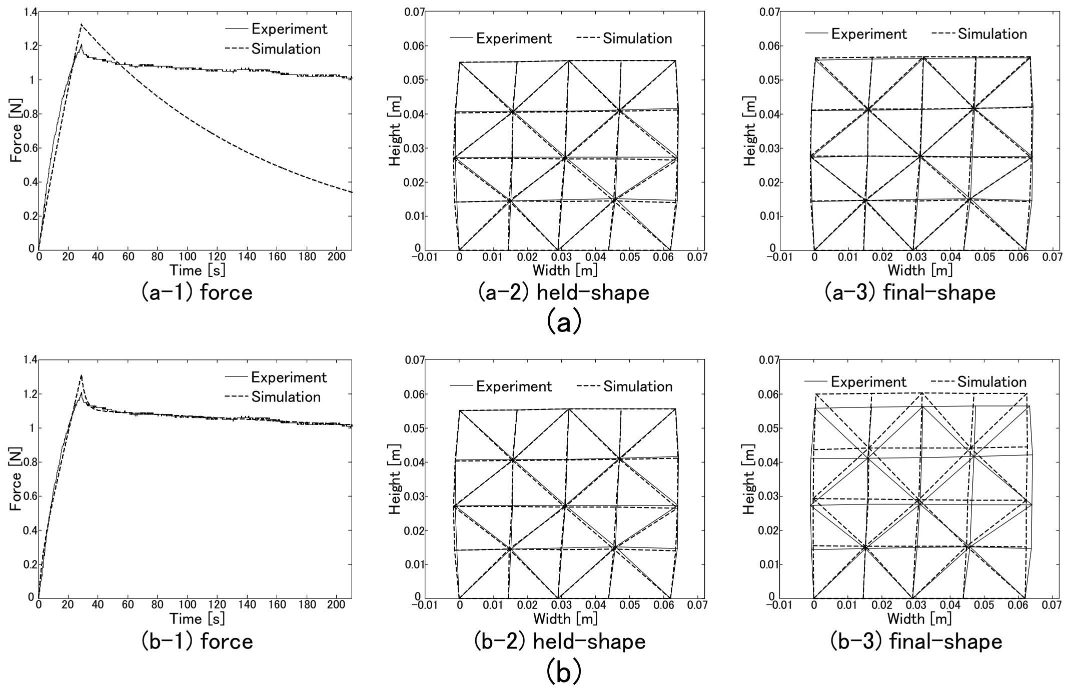

Figure 6.14: Validation results for sweets material 1 (a) with and (b) without the constraint of $\sum_{i=1}^{3} c_i$.

6.4.2 Validation Results of Objects Made by Japanese Sweets Materials

The estimated parameters listed in Tables 6.11 and 6.12 were used to simulate these three objects to see what happen for sweets materials with two estimation methods with or without the constraint of $\sum_{i=1}^{3} c_i$. Simulation results compared with experimental measurements for these three trials are shown in Figs. 6.14, 6.15, and 6.16, respectively. We can see that estimated parameters with the constraint of $\sum_{i=1}^{3} c_i$ yield good results of final-shapes but bad results of forces. On the contrary, estimated parameters without this constraint result in good results in force but bad in final-shapes. This again proved our theoretical discussions of $\sum_{i=1}^{3} c_i$ dominating both force amplitude and residual deformation. The values of $\sum_{i=1}^{3} c_i$ in Tables 6.11 and 6.12 are very different with each other. The ratios between these two set of values $\sum_{i=1}^{3} c_i$ are 12.5, 7.91, and 4.3 (values in Table 6.12 divided by values in Table 6.11) for sweets materials 1, 2, and 3, respectively. We

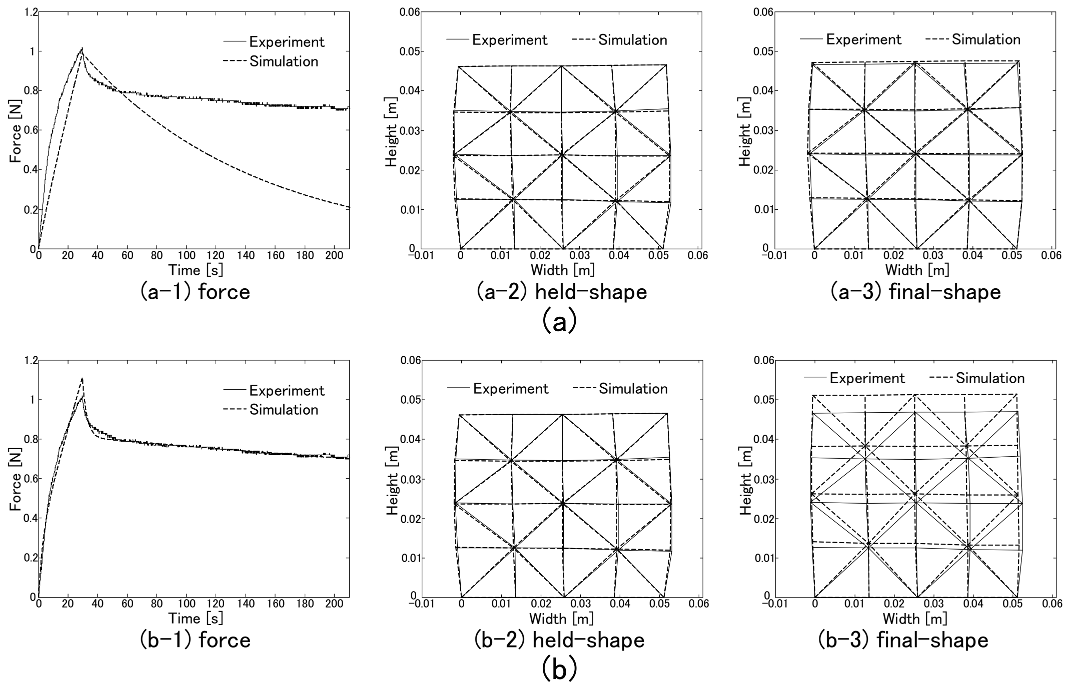

Figure 6.15: Validation results for sweets material 2 (a) with and (b) without the constraint of $\sum_{i=1}^{3} c_i$.

can see that material 1 has the largest ratio and also the largest difference of the objective function values (listed in the right most column in Tables 6.11 and 6.12). We are not able to accurately reproduce both forces and deformation behaviors simultaneously for sweets objects by using only one set of parameters. Using one set of parameters, we can reproduce either rheological forces or deformation behaviors alone. It is impossible to cover both in the same time. If we use only one set of parameters, we always have to compromise between the reproductions of force and deformation behaviors. We believe the reason of this phenomenon arises from the nonlinearity of material properties. Our FE model is based on linear Hooke's law, which provided a proportional relationship between stress and strain (force and displacement in 2D case). Most real materials include nonlinear, rate-, and time-dependent properties. Therefore, it is hard to use a linear model to approximate such nonlinear behaviors. We can introduce nonlinear modeling, such as the model with Green strain tensor as presented in Section 3.2, to cope with this problem. Such nonlinear models suffer from high computational cost

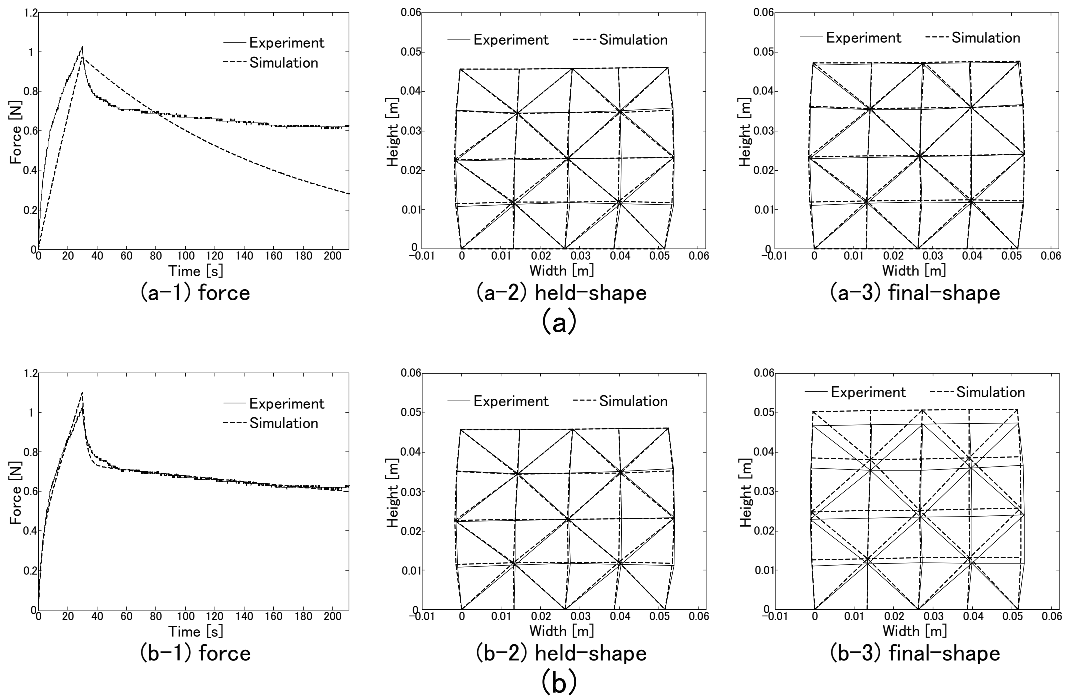

Figure 6.16: Validation results for sweets material 3 (a) with and (b) without the constraint of $\sum_{i=1}^{3} c_i$.

because of the complicated constitutive equations and the intensive calculation for updating the stiffness matrices. Analytical expressions of force are usually not available for such nonlinear models, which makes the parameter estimation more difficult and sometimes inapplicable. We have therefore introduced dual-moduli viscous elements into our FE model to deal with this problem and next section will demonstrate validation results of this model.

6.4.3 Validation Results of FE Model with Dual-Moduli Viscous Elements

The dual-moduli viscous element has an ability to switch two parameters from one to the other during simulation. The FE model is still linear model and only some parameters (c_1 and c_2 in the case of parallel 5-element model) change values before and after the switching moment. This model can yield accurate reproductions of both rheological forces and deformation behaviors simultaneously with the same computation cost as a linear model with one set of parameters.

6.4.3.1 Validation Results for Corresponding Uniform Objects

At first, we have used the estimated parameters listed in Table 6.13 to simulate the corresponding objects made by three sweets materials. The simulation results compared with experimental measurements are shown in Fig. 6.17, where the solid line denotes the results from experimental measurements and dashed line (may be hard to distinguish) denotes the results from simulation. We can see that this model successfully captured both rheological forces and deformation behaviors simultaneously.

6.4.3.2 Validation Results for Non-Uniform Layered Objects Made by Sweets Materials

Again, the simulation results shown in Fig. 6.17 were performed using their own estimated parameters. These validation results therefore only demonstrate how well the parameter estimation procedures were conducted. In order to further evaluate the estimated parameters, several other experimental trials with layered objects, as shown in Fig. 6.5, were performed. Each object consists of three layers and two different materials, with the materials of the top and bottom layers being identical. These types of layered structures are often encountered in food products, such as sandwich and sushi. Different combinations of two materials were tested, *e.g.*, in Fig. 6.5a-1, the object was made of Materials 1 and 2 with Material 1 in the middle. The objects were compressed over their entire top surfaces (Fig. 6.5a) or at the center (Fig. 6.5b) of the top surfaces with a constant velocity of 0.2 mm/s. Detailed experimental information can be found in Table 6.2. The estimated parameters listed in Table 6.13 were then used to simulate these layered objects. Comparisons of the simulation results and experimental measurements are shown in Figs. 6.18 and 6.19. In Fig. 6.19, the object images are from experiments and the blue and red lines are obtained from simulations. Because the objects compressed over their entire top surfaces showed simple deformation behaviors, 4×8 triangular meshes are sufficient for their simulations, as shown in Fig. 6.18. On the other hand, the objects compressed at

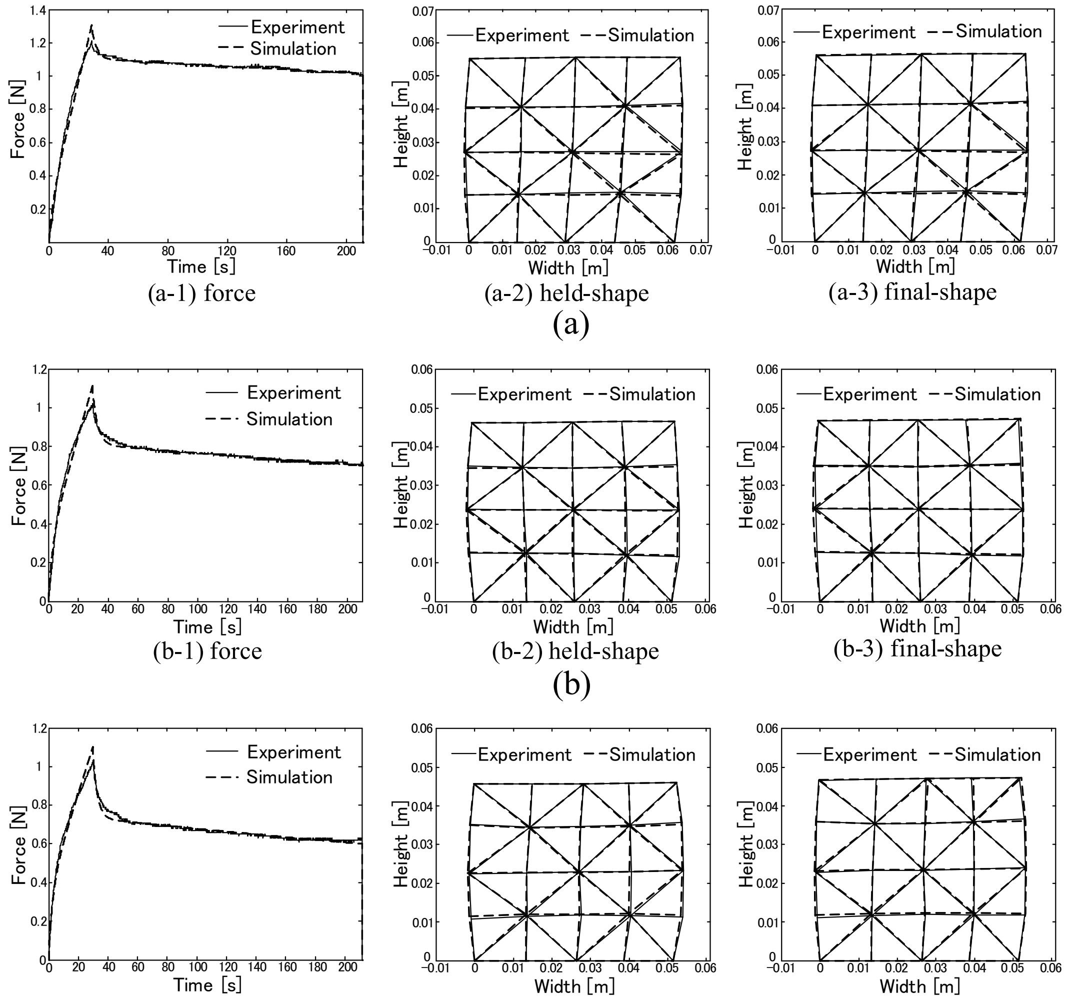

(a-1) force (a-2) held-shape (a-3) final-shape
(a)

(b-1) force (b-2) held-shape (b-3) final-shape
(b)

(c-1) force (c-2) held-shape (c-3) final-shape
(c)

Figure 6.17: Validation results of FE model with dual-moduli viscous elements for objects made by Japanese sweets material 1 (a), 2 (b), and 3 (c).

the center of top surfaces demonstrate more complicated deformations around the contact corners. We therefore use triangular meshes with finer resolution (16×32) to reproduce these deformation behaviors. In Fig. 6.19, only 8×16 lattice meshes are given for the convenience of comparisons with the experimental images. The validation results in Figs. 6.18 and 6.19 show the successful reproductions of both deformation behaviors and force responses for these layered objects. But the simulations results shown in Fig. 6.19 exhibited larger errors than those in Fig.

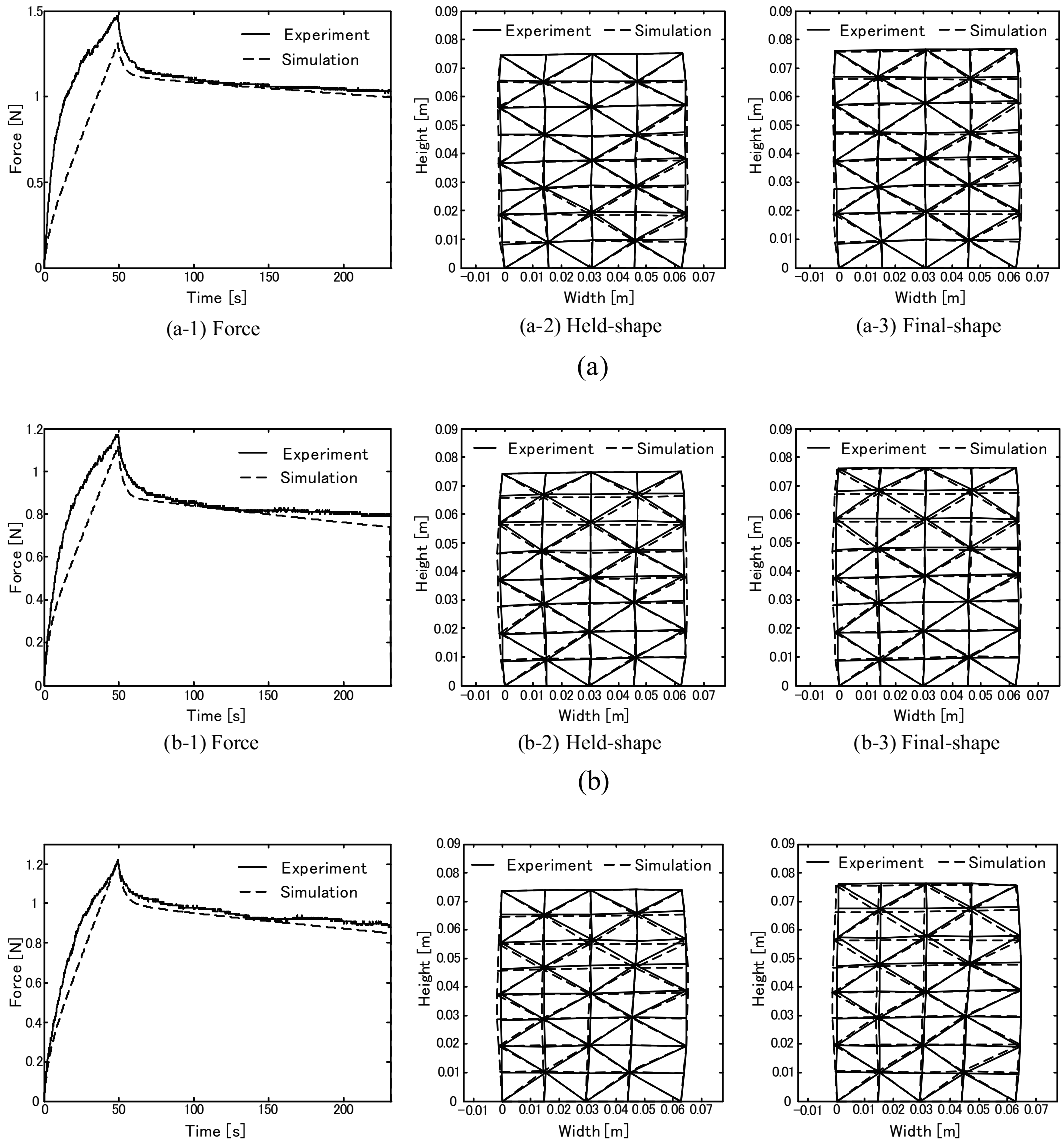

(a-1) Force (a-2) Held-shape (a-3) Final-shape

(a)

(b-1) Force (b-2) Held-shape (b-3) Final-shape

(b)

(c-1) Force (c-2) Held-shape (c-3) Final-shape

(c)

Figure 6.18: Validation results of layered objects compressed over the entire top surfaces. The layered objects made by materials 1+2 (a), 2+3 (b), and 1+3 (c), respectively.

6.18, especially the force behaviors. This suggests that better validation results might be obtained if the operation conditions used in parameter estimation and application are identical. Even though the force reproductions in Fig. 6.19 suffer

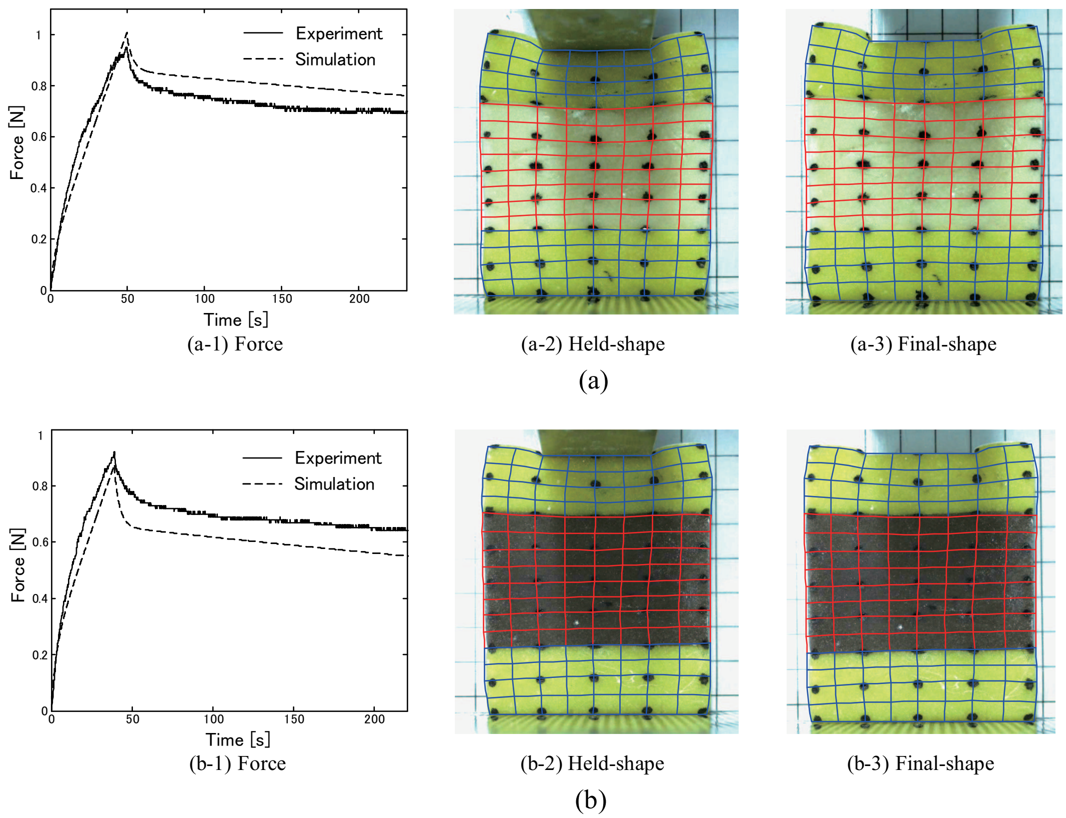

Figure 6.19: Validation results of layered objects compressed at the center of the entire top surfaces. The layered objects made by materials 1+2 (a) and 2+3 (b), respectively.

from some errors, the errors are still in acceptable range for most applications.

6.5 Concluding Remarks

In this chapter, experimental setup and compressing tests were demonstrated and simulation results were compared with experimental measurements to validate our FE models and parameter estimation methods. Two kinds of rheological materials, commercial available clay and Japanese sweets materials, were employed in our experiments. Flat-squared objects made by these two materials were compressed using a linear stage with a pushing-holding-releasing operations. The force data and static images were recorded for estimating the physical parameters. The estimation methods presented in Chapter 5 were used to estimate the physical parameters for these objects. Two sets of parameters with or without the constraint of $\sum_{i=1}^{3} c_i$ were given to compare the differences. The simulations were then performed using the estimated parameters and comparisons between simulation results and experimental measurements were done to validate the proposed FE models and parameter estimation methods. We found that the estimated parameters with the constraint of $\sum_{i=1}^{3} c_i$ yield better reproduction of final-shapes while parameters without $\sum_{i=1}^{3} c_i$ result in better force reproductions. For some objects made by clay materials, good reproductions of both rheological forces and deformation behaviors can be achieved simultaneously by using only one set of parameters. However for other objects, this is impossible and the reason caused the failure is the linearity of the physically-based models. Fortunately, after introducing the dual-moduli viscous elements into our FE models, we have finally solved this problem and successfully reproduced both rheological forces and deformation behaviors simultaneously. The estimated parameters from uniform objects can also be used in simulating non-uniform layered objects even with different compressing operations.

Note that the measurement requirements for our estimation methods included three static images of the object: the initial shape, the held-shape, and the final-shape, and the force responses during the experiments. In addition, we have used regular shaped objects with some markers drawn on the surfaces throughout our experiments. However, our estimation method is not limited by the shape of the object and can be applied to arbitrary object as long as the deformation field of some feature points is available. Besides, the loading position is also not limited to the top surface but may be anywhere, even at just one point convenient for force measurements.

Chapter 7

Conclusions and Future Works

7.1 Conclusions

Modeling and simulation of deformable objects has been playing an important role in many applications, such as surgical simulation, robotic manipulation, food engineering, and so on. Many modeling methods have been proposed, such as MSD, FEM, and particle-based methods, *etc.* They all have their own advantages and disadvantages. There are even many commercial softwares available for simulating deformable objects, such as ANSYS and ABAQUS. However, the modeling and simulation of deformable objects is still a unmature and hot research field. This is not only because the development of computation technology makes more methods applicable, but also because the diversity of deformation behaviors demonstrated in real world objects.

The work presented in this dissertation is focusing on modeling and reproducing the behaviors of rheological objects, which include both elastic and plastic properties and always yield residual deformation after loading-unloading operations. The difficult part of this subject is how to accurately reproduce both rheological forces and deformation, especially residual deformation behaviors simultaneously. The main contributions of our current work are as follows:

1. We have summarized the physically-based models which can be used to simulate rheological behaviors. We categorized such physical models into serial and parallel models and proposed a criterion to choose an appropriate

one for certain application. We have derived the generalized constitutive laws for both models and found a corresponding relation between the two models. We then derived the analytical expressions of rheological forces and residual deformation for generalized parallel models. Through a series of analysis, we found that there is contradiction between accurate reproductions of rheological forces and residual deformation. In order to cope with this contradiction, we have proposed a dual-moduli viscous element and integrated it with our physically-based models.

2. We have developed 2D and 3D FE dynamic models for simulating rheological behaviors based on the physically-based models and linear Cauchy strain tensor. In order to simulate large deformation and deformation with rotation motion, the nonlinear Green strain tensor has also been introduced into our FE formulations. The FE dynamic model with dual-moduli viscous elements was also derived. We have then extended our FE model to deal with non-uniform layered objects and contact interaction between rheological objects and external instruments. We found that the losing contact moment can serve as a perfect criterion for dual-moduli viscous element to switch the parameters.

3. We have proposed several methods for estimating the physical parameters of rheological objects. The basic idea is to minimize the difference between simulation results and experimental measurements with updated physical parameters. In order to capture both rheological forces and deformation behaviors, we proposed a three-step method with a separate estimation of Poisson's ratio γ and calculation of summation $\sum_{i=1}^{n} c_i$. Both simulation- and calculation-based optimization methods were investigated and compared. The simulation-based method is robust but time-consuming, while the calculation-based method is very efficient but limited to only parallel models. we found that the three-step method works well for some rheological objects but failed to others. We have therefore estimated the parameters of FE model with dual-moduli viscous elements. We employed the calculation-based optimization method to minimize the force difference and simulation-based method to optimize the difference of final-shapes.

4. A series of compressing tests were performed using objects made by commercial available clay and Japanese sweets materials. Experimental measurements of uniform objects with compressing from the top surfaces were used to estimate the physical parameters. The estimated parameters were then employed to simulate uniform objects with compressing operation from the top-center surfaces and even non-uniform layered objects. Through various validations, we proved the contradiction between the reproductions of rheological forces and residual deformation. For several clay objects, this contradiction phenomenon is not obvious and we could obtain acceptable results for both force and deformation using only one set of parameters. For other objects, however, this contradiction phenomenon is very strong and it is impossible to use one set of parameters to cover both rheological forces and deformation behaviors. This coincides with our theoretical discussions. The FE model with dual-moduli viscous elements and estimated parameters were then employed to solve this problem and finally we successfully reproduced both rheological forces and deformation behaviors simultaneously.

Even though our current work concentrated on reproductions of rheological behaviors, most of our discussions and methods can be easily applied to elastic, visco-elastic, and plastic models as long as the physically-based models were used. Since our attention is focusing on the reproduction accuracy of both forces and deformation, we have to sacrifice the computation costs and real-time performance is not of concern in the current situation.

7.2 Future Works

According to our current works, we have done a systematic analysis of modeling for simulating rheological behaviors and we have established efficient methods for estimating physical parameters of rheological objects. In the future, we plan to make our efforts on the following directions:

1. 3D validation of our FE model and estimated parameters. 3D FE formulation has been presented in this dissertation. But we did not perform any simulation validation for real objects with estimated parameters. The physical parameters were mainly estimated by using 2D FE model and they are supposed to be applicable in 3D simulation. Thus, we need experimental validations of this issue. If the proposed methods are not applicable, new parameter estimation methods with 3D model have to be investigated. This is theoretically feasible but practically difficult because the computation costs.

2. Therefore, the second future target is to speed up our FE simulation. We plan to use the new computing architecture called GPGPU (General Purpose Graphic Processing Unit) to achieve this target.

3. In the current experiments, only two kinds of materials were tested. This is quite limited. We will perform more experiments with other rheological objects, such as Japanese tofu and various kinds of sushi. There might be some interesting behaviors which have not been discovered.

4. We are now working on particle-based model, such as Smoothed Particle hydrodynamics (SPH). This could be another option for simulating rheological objects. Comparing with FE model, SPH model has advantages of low computation costs and convenient implement for complex operations, such as cutting and reforming. The SPH model also need parameter estimation when dealing with real materials. The parameter estimation ideas presented in this dissertation can serve as a good reference.

References

Ahn, B. & Kim, J. (2010). Measurement and characterization of soft tissue behavior with surface deformation and force response under large deformations. *Med. Image Anal.*, **14**, 138–148. 3, 5

Augenstein, K., Cowan, B., LeGrice, I., Nielsen, P. & Young, A. (2005). Method and apparatus for soft tissue material parameter estimation using tissue tagged magnetic resonance imaging. *J. Biomech. Eng.-Trans. ASME*, **127**, 148–157. 5

Balaniuk, R. & Salisbury, K. (2003). Soft-tissue simulation using the radial elements method. *Surgery simulation and soft tissue modeling*, 48–58. 3

Baraff, D. & Witkin, A. (1998). Large steps in cloth simulation. *Proc. 25th Annual Conference on Computer Graphics and Interactive Techniques (SIGGRAPH'98)*, 43–54. 2

Baumgarte, J. (1972). Stabilization of constraints and integrals of motion in dynamical systems. *Computer Methods in Applied Mechanics and Engineering*, 1–16. 35

Bianchi, G., Solenthaler, B., Székely, G. & Harders, M. (2004). Simultaneous topology and stiffness identification for mass-spring models based on fem reference deformations. *Proc. 7th International Conference on Medical Image Computing and Computer-Assisted Intervention (MICCAI'04)*, 293–301. 3

Bischoff, J., Arruda, E. & Grosh, K. (2000). Finite element modeling of human skin using an isotropic, nonlinear elastic constitutive model. *J. Biomech.*, **33**, 645–652. 3

Bro-Nielsen, M. (1998). Finite element modeling in surgery simulation. *Proc. IEEE*, **86**, 490–503. 3

Bro-Nielsen, M. & Cotin, S. (1996). Real-time volumetric deformable models for surgery simulation using finite element and condensation. *Computer Graphics Forum (EUROGRAPHICS'96)*, 57–66. 3

Chai, Y.H., Luecke, G. & Edwards, J. (1998). Virtual clay modeling using the ISU exoskeleton. *Proc. IEEE Virtual Reality Annual International Symposium (VRAIS '98)*, 76–80. 7

Chua, P., Ilschner, T. & Caldwell, D. (2003). Robotic manipulation of food products—a review. *Ind. Robot*, **30**, 345–354. 4

Cotin, S., Delingette, H., Bro-Nielsen, M., Ayache, N., Clément, J., Tassetti, V. & Marescaux, J. (1996). Geometric and physical representations for a simulator of hepatic surgery. *Proc. Medicine Meets Virtual Reality*, 139–151. 2

Farshad, M., Barbezat, M., Flüeler, P., Schmidlin, F., Graber, P. & Niederer, P. (1999). Material characterization of the pig kidney in relation with beh biomechanical analysis of renal trauma. *J. Biomech.*, **32**, 417–425. 6

Hing, J., Brooks, A. & Desai, J. (2007). A biplanar fluoroscopic approach for the measurement, modeling, and simulation of needle and soft-tissue interaction. *Med. Image Anal.*, **11**, 62–78. 3, 5

Hoshi, T., Kobayashi, Y., Kawamura, K. & Fujie, M. (2007). Developing an intraoperative methodology using the finite element method and the extended kalman filter to identify the material parameters of an organ model. *Proc. the 29th Annual International Conference of the IEEE EMBS*, 469–474. 5

Hrapko, M., van Dommelen, J., Peters, G. & Wismans, J. (2006). The mechanical behaviour of brain tissue: Large strain response and constitutive modelling. *Biorheology*, **43**, 623–636. 4

Ikawa, T. & Noborio, H. (2007). On the precision and efficiency of hierarchical rheology MSD model. *Proc. the 2007 IEEE/RSJ International Conference on Intelligent Robots and Systems (IROS'07)*, 376–383. 5, 7

Kähler, K., Haber, J. & Seidel, H.P. (2001). Geometry-based muscle modeling for facial animation. *Proc. of Graphics Interface*, 37–46. 2

Kauer, M., Vuskovic, V., Dual, J., Szekely, G. & Bajka, M. (2002). Inverse finite element characterization of soft tissues. *Med. Image Anal.*, **6**, 275–287. 3, 5

Lim, Y.J. & De, S. (2007). Real time simulation of nonlinear tissue response in virtual surgery using the point collocation-based method of finite spheres. *Comput. Methods Appl. Mech. Engrg.*, **196**, 3011–3024. 3

Lioyd, B., Székely, G. & Harders, M. (2007). Identification of spring parameters for deformable object simulation. *IEEE Trans. Vis. Comput. Graph.*, 1081–1094. 2, 3

Liu, Z. & Scanlon, M. (2003). Modelling indentation of bread crumb by finite element analysis. *Biosyst. Eng.*, **85**, 477–484. 3

Martins, R. (2006). Simple finite volumes and finite elements procedures for food quality and safety simulations. *J. Food Eng.*, **73**, 327–338. 3

Mendoza, C. & Laugier, C. (2003). Simulating soft tissue cutting using finite element models. *Proc. the 2003 IEEE International Conference on Robotics and Automation (ICRA'03)*, 1109–1114. 3

Mirsaeedghazi, H., Djomeh, Z. & Mousavi, S. (2008). Rheometric measurement of dough rheological characteristics and factors affecting it. *Int. J. Agri. Biol.*, **10**, 112–119. 7

Nava, A., Mazza, E., Furrer, M., Villiger, P. & Reinhart, W. (2008). In vivo mechanical characterization of human liver. *Med. Image Anal.*, **12**, 203–216. 3, 4

Noborio, H., Enoki, R., Nishimoto, S. & Tanemura, T. (2003). On the calibration of deformation model of rheology object by a modified randomized algorithm. *Proc. IEEE International Conference on Robotics and Automation (ICRA'03)*, 3729–3736. 6, 7

Nogami, R., Noborio, H., Tomokuni, S. & Hirai, S. (2004a). A comparative study of rheology MSD models whose structures are lattice and truss. *Proc. IEEE/RSJ International Conference on Intelligent Robots and Systems (IROS'04)*, 3809–3816. 7

Nogami, R., Noborio, H., Ujibe, F. & Fujii, H. (2004b). Precise deformation of rheologic object under MSD models with many voxels and calibrating parameters. *Proc. IEEE International Conference on Robotics and Automation (ICRA'04)*, 1919–1926. 7

Purlis, E. & Salvadori, V. (2005). Meat cooking simulation by finite elements. *2nd Mercosur Congress on Chemical Engineering and 4th Mercosur Congress on Process Systems Engineering*, 1–10. 3

Sakamoto, N., Higashimori, M., Tsuji, T. & Kaneko, M. (2007). An optimum disign of robotic hand for handling a visco-elastic object based on Maxwell model. *Proc. the 2007 IEEE International Conference on Robotics and Automation (ICRA'07)*, 1219–1225. 6, 7

Samur, E., Sedef, M., Basdogan, C., Avtan, L. & Duzgun, O. (2007). A robotic indenter for minimally invasive measurement and characterization of soft tissue response. *Med. Image Anal.*, **11**, 361–373. 5

Shames, I. & Cozzareli, F. (1992). *Elastic and Inelastic Stress Analysis*. Englewood, New Jersey. 4

Sivaramakrishnan, H., Senge, B. & Chattopadhyay, P. (2004). Rheological properties of rice dough for making rice bread. *J. Food Eng.*, **62**, 37–45. 7

Tada, M., Nagai, N. & Maeno, T. (2005). Material properties estimation of layered soft tissue based on MR observation and iterative FE simulation. *Medical Image Conputing and Computer-Assisted Intervention (MICCAI'05)*, **3750**, 633–640. 5

Taylor, Z., Comas, O., Cheng, M., Passenger, J., Hawkes, D., Atkinson, D. & Ourselin, S. (2009). On modelling of anisotropic viscoelasticity for soft tissue simulation: numerical solution and GPU execution. *Med. Image Anal.*, **13**, 234–244. 3

Terzopoulos, D. & Fleischer, K. (1988). Modeling inelatic deformation: viscoelasticity, plasticity, fracture. *Proc. 15th Annual Conference on Computer Graphics and Interactive Techniques (SIGGRAPH '88)*, 269–278. 2, 6

Terzopoulos, D., Platt, J., Barr, A. & Fleischer, K. (1987). Elastically deformable models. *Proc. 14th Annual Conference on Computer Graphics and Interactive Techniques (SIGGRAPH '87)*, 205–214. 2

Tsai, C.H., Kao, I., Sakamoto, N., Higashimori, M. & Kaneko, M. (2008). Applying viscoelastic contact modeling to grasping task: an experimental case study. *Proc. the 2008 IEEE/RSJ International Conference on Intelligent Robots and Systems (IROS'08)*, 1790–1795. 6, 7

Wang, Z. & Hirai, S. (2009). Modeling and parameter identification of rheological object based on fe method and nonlinear optimization. *Proc. IEEE/RSJ International Conference on Intelligent Robots and Systems (IROS '09)*, 1968–1973. 23, 24

Waters, K. (1987). A muscle model for animating three-dimensional facial expression. *Proc. 14th Annual Conference on Computer Graphics and Interactive Techniques (SIGGRAPH'87)*, **21**, 17–24. 2

Wu, M., Li, D., Wang, L., Özkan, N. & Mao, Z. (2010). Rheological properties of extruded dispersions of flaxseed-maize blend. *J. Food Eng.*, **98**, 480–491. 8

Yoshida, H., Murata, Y. & Noborio, H. (2005). A smart rheologic MSD model pushed/calibrated/evaluated by experimental impulses. *Proc. IEEE/RSJ International Conference on Intelligent Robots and Systems (IROS'05)*, 269–276. 7

Yoshida, H., Ujibe, F. & Noborio, H. (2007). Force/shape reappearance of MSD rheology model calibrated by force/shape sequence. *17th International Conference on Artificial Reality and Telexistence 2007*, 121–128. 7